Parameters affecting interferometric coherence and implications for long-term operational monitoring of mining-induced surface deformation

By

Jeanine Engelbrecht

Thesis Presented for the Degree of

Doctor of Philosophy

in the

Department of Electrical Engineering
Faculty of Engineering and the Built Environment
University of Cape Town

Supervisor: Prof. Michael R. Inggs

February 2013

ABSTRACT

Parameters affecting interferometric coherence and implications for long-term operational monitoring of mining-induced surface deformation
Jeanine Engelbrecht, February 2013

Surface deformation due to underground mining poses risks to health and safety as well as infrastructure and the environment. Consequently, the need for long-term operational monitoring systems exists. Traditional field-based measurements are point-based meaning that the full extent of deforming areas is poorly understood. Field-based techniques are also labour intensive if large areas are to be monitored on a regular basis. To overcome these limitations, this investigation considered traditional and advanced differential radar interferometry techniques for their ability to monitor large areas over time, remotely. An area known to be experiencing mining induced surface deformation was used as test case. The agricultural nature of the area implied that signal decorrelation effects were expected. Consequently, four sources of data, captured at three wavelengths by earth-orbiting satellites were obtained. This provided the opportunity to investigate different phase decorrelation effects on data from standard imaging platforms using real-world deformation phenomenon as test-case.

The data were processed using standard dInSAR and polInSAR techniques. The deformation measurement results together with an analysis of parameters most detrimental to long-term monitoring were presented. The results revealed that, contrary to the hypothesis, polInSAR techniques did not provide an enhanced ability to monitor surface deformation compared to dInSAR techniques. Although significant improvements in coherence values were obtained, the spatial heterogeneity of phase measurements could not be improved. Consequently, polInSAR could not overcome decorrelation associated with vegetation cover and evolving land surfaces. However, polarimetric information could be used to assess the scattering behaviour of the surface, thereby guiding the definition of optimal sensor configuration for long-term monitoring.

Despite temporal and geometric decorrelation, the results presented demonstrated that mining-induced deformation could be measured and monitored using dInSAR techniques. Large areas could be monitored remotely and the areal extent of deforming areas could be assessed, effectively overcoming the limitations of field-based techniques. Consequently, guidelines for the optimal sensor configuration and image acquisition strategy for long-term operational monitoring of mining-induced surface deformation were provided.

SUMMARY

Mining activities have the tendency to change the natural environment in several ways. Surface deformation due to underground mining is one area of concern, since it not only poses risks to health and safety, but also to infrastructure and the environment. Traditionally, the monitoring of surface deformation has been achieved by means of ground-based approaches. However, these techniques provide only point-based measurements meaning that the full extent of deforming areas is frequently poorly understood. Additionally, field-based measurements are usually made only on reasonable assumption of potential deformation, or once evidence of deformation has been detected by some other means, such as the observation of infrastructural damage or rainwater ponding on agricultural fields. The field-based approaches are also expensive in terms of man-power, especially if large areas need to be monitored on a regular basis.

To overcome the limitations associated with the field-based techniques, the use of differential radar interferometry techniques were considered in this investigation for their ability to reliably monitor large areas over time, remotely. Specifically, the investigation aimed to test the application of differential radar interferometry techniques for their ability to measure and monitor mining-induced surface deformation in the Witbank Coalfields of South Africa. The dynamic agricultural nature of the area implied that known limitations, due to phase decorrelation of SAR signals over time, could be expected. For this reason, four sources of SAR data were used, which provided information captured at three different wavelengths, namely X-Band (3.1 cm), C-band (5.6 cm), and L-band (23.6 cm). Different geometric and temporal properties at the time of image capture provided an opportunity to investigate the different signal decorrelation effects of data from standard SAR imaging platforms using a real-world deformation phenomenon as test-case.

The results of the monitoring of surface deformation using the various sources of SAR data were presented together with an analysis of the parameters most detrimental to the successful long-term monitoring of surface deformation using these techniques. The results revealed that dInSAR techniques can be employed to detect, measure and monitor surface subsidence associated with coal mining activities in the Witbank Coalfields. The results of the investigation further revealed that, contrary to the hypothesis, differential polarimetric interferometry did not provide an enhanced ability to measure mining-induced subsidence compared to traditional single polarisation interferometry approaches.

Despite significant improvements in the actual coherence values, the spatial heterogeneity of the phase contributions could not be improved. More specifically, polInSAR techniques were not able to overcome coherence limitations associated with vegetation cover and the evolution of the land surface over time. Although polarimetric data could not be used to enhance deformation measurements, the polarimetric analysis of quadrature polarisation data did provide an indication of the dominant scattering mechanisms over time and at different wavelengths. Together with the deformation measurements and analysis of the parameters associated with phase decorrelation, this information provided a significant amount of information that could be used to define the optimal sensor configuration and image acquisition strategy for the long-term monitoring of mining induced subsidence.

Despite limitations due to temporal and geometric decorrelation effects, the results presented here demonstrated that the traditional dInSAR approaches can overcome many of the limitations associated with field-based approaches. Specifically, large areas can be monitored remotely and the areal extent of deforming basins can be assessed. Additionally, the revisit time of the operational sensors means that routine measurements will be possible. Consequently, dInSAR measurements are highly complementary to traditional monitoring approaches. It is recommended that dInSAR techniques be included as a part of a long term strategy for the monitoring of deformation caused by mining.

LIST OF PUBLICATIONS

Engelbrecht, J., Inggs, M.R. and Makusha, G. 2011. Detection and monitoring of surface subsidence associated with mining activities in the Witbank Coalfields using differential radar interferometry. *South African Journal of Geology*, 114, pp 77 -94

Engelbrecht, J., Musekiwa, C., Kemp, J. and Inggs, M.R. 2013. Parameters affecting interferometric coherence- the case of a dynamic agricultural region. *IEEE Transactions on Geoscience and Remote Sensing*, 52 (1) doi 10.1109/TGRS.2013.2252620

Engelbrecht, J. and Inggs, M.R. 2013. Differential interferometry techniques on L-band data employed for the monitoring of surface subsidence due to mining. *South African Journal of Geomatics,*2 (2), pp 82 - 93

Engelbrecht, J. and Inggs, M.R. 2013. Recommendations for long-term operational dInSAR monitoring of mining-induced deformation in a dynamic agricultural region. *IEEE International Geoscience and Remote Sensing Symposium*, Melbourne, Australia

Engelbrecht, J., Inggs, M.R. and Kemp, J. 2013. The phenology of an agricultural region as expressed by polarimetric decomposition and vegetation indices. *IEEE International Geoscience and Remote Sensing Symposium*, Melbourne, Australia

Engelbrecht, J. 2010. Mapping and measuring surface deformation related to mining activities in the Witbank Coalfields using differential radar interferometry: Progress report September 2010. *Council for Geoscience Confidential file report number 2010-0200*. Council for Geoscience, Pretoria, South Africa.

Engelbrecht, J. 2011. Differential radar interferometry detects surface subsidence associated with mining activities in the Witbank Coalfields: A Progress report November 2011. *Council for Geoscience Confidential file report number 2011-0114*. Council for Geoscience, Pretoria, South Africa.

Engelbrecht, J. and Inngs, M.R. 2012. Surface deformation monitoring using synthetic aperture radar data. *Presented at the SA-GEO Conference 2012*, Cape Town, South Africa

Engelbrecht, J. 2012. Synthetic aperture radar data employed for the measurement of surface deformation due to mining. *Presented at the SASA Congress 2012*, Cape Town, South Africa

Engelbrecht, J. 2011. Differential Radar Interferometry detects surface subsidence associated with mining activities in the Witbank Coalfields. *Coaltech Research Association Annual Colloquium 2011*, Witbank, South Africa (invited paper)

Engelbrecht, J., Makusha, G., Bradford, A. and Inggs, M.R. 2011. Detection and Monitoring of Surface subsidence associated with mining activities in the Witbank Coalfields using differential radar interferometry. *30th International Conference on Ground Control in mining*, Morgantown, West Virginia

Engelbrecht, J. and Inggs, M.R. 2011. Differential Radar Interferometry detects surface subsidence due to mining activities in the Witbank Coalfields. *Geosynthesis 2011*, Cape Town, South Africa.

Engelbrecht, J., Inggs, M.R. and Makusha, G. 2011. Detection and monitoring of surface subsidence associated with mining activities in the Witbank Coalfields, South Africa, using differential radar Interferometry. *IEEE International Geoscience and Remote Sensing Symposium*, Vancouver, Canada

ACKNOWLEDGEMENTS

The thesis was made possible with the support and co-operation of many individuals and institutions. The author therefore wishes to express sincere appreciation to the following:

- Prof. Michael Inggs for his skilful supervision, assistance and advice;
- The Council for Geoscience and for partial funding of the research;
- The Department of Science and Technology for partial funding of the research through the South African Geological Hazards Observation System (SAGHOS) project;
- The European Space Agency for providing the ERS-2 and ALOS PALSAR data used in the research through their CAT-1 support initiative;
- The Deutsches Zentrum für Luft- und Raumfahrt (DLR) for providing the TerraSAR-X data used in this investigations through the TerraSAR-X science Service System;
- Gift Makusha, Angus Bradford, Pieter Jonker, Wikus Mahne, Calvin Govendor, Ria Olivier and Cecilia Pretorius form Anglo American and Anglo Coal for their assistance during field investigations and advice on the problem, its effects and implications;
- Dr. Luc Chevallier, Kate Robey, Dr. Jaco Kemp and other friends, family and colleagues for their unwavering support and advice;
- The external examiners for their constructive remarks and meaningful suggestions.

CONTENTS

FIGURES

TABLES

1 BACKGROUND TO THE STUDY

1.1 INTRODUCTION TO GEOHAZARDS AND INTERFEROMETRY

Geological hazards (also called geohazards) are naturally occurring or man-made conditions or phenomena that present a risk or are a potential danger to life and property (e.g. landslides, floods, earthquakes, ground subsidence, coastal and beach erosion, faulting, dam and leakage failure, mining disasters, pollution and waste disposal, sinkholes, volcanic eruptions and many more). The opportunities in studying the field of geohazards revolve around the notion of developing decision-support or risk-management systems aimed at reducing the impact of geohazards. Where risk is appropriately expressed in terms of expected impacts, scientists should move towards addressing the mitigation of such risks, thereby providing answers, solutions and recommendations.

Radar remote sensing techniques can contribute to programmes dedicated to the assessment of natural risks and hazards, and can be regarded as a unique tool to obtain deformation measurements over large areas (Carnec & Delacourt 2000; Carnec & Raucoules 2000; Guéguen et al. 2009; Le Mouélic et al. 2005; Simonetto et al. 2005). The synoptic view provided by SAR data will provide an overview of potential hazards and is expected to be a powerful tool for initial assessment of potentially hazardous areas, on the basis of which further ground-based measurement can be commissioned. The latest development in the field of radar remote sensing is in the use of a technique called radar interferometry which has been employed to monitor the stability of large engineering works and for detecting and measuring ground deformations on the earth's surface (ESA (European Space Agency) 2005). Astonishing accuracies have been achieved in several areas of research including: 1) measuring of surface subsidence; 2) assessment of deformation following earthquake activity; 3) monitoring of landslides and deformation linked to volcanic activity, and many more (ESA (European Space Agency) 2005). The interferometry techniques open up many new potential application areas for space-borne synthetic aperture radar (SAR) data in disciplines such as volcanology, structural geology, glaciology and geotechnics, and for work relevant to a variety of geohazards, including surface subsidence and landslide monitoring (ESA (European Space Agency) 2005).

Research in applications of radar interferometry to measure changes in the earth's surface has increased since the early 1990s (Akoglu et al. 2006; Massonnet & Feigl 1998). Synthetic Aperture Radar (SAR)

technology is an important tool for monitoring deformation resulting from seismic or anthropogenic causes (Yen et al. 2007). This is because synthetic aperture radar interferometry (InSAR) provides the ability to map surface deformations of small spatial extent and to monitor their spatial evolution over time (Carnec & Delacourt 2000; Herrera et al. 2007; Le Mouélic et al. 2005; Reigber et al. 2007). Various authors also describe the ability to map large-scale surface deformations using InSAR techniques (Akoglu et al. 2006; Carnec & Delacourt 2000; Massonnet & Feigl 1998). The advantage of InSAR is that it provides a comprehensive overview of the motion detected for an entire affected area (Guéguen et al. 2009; Rosen et al. 2000). It is expected that this type of result will complement ground-based measurements, which are generally only made at a limited number of locations.

Traditional ground-based measurements (such as spirit-levelling and GPS networks) of deformation of the earth surface are well established and frequently employed. However, the advantages of differential radar interferometry (dInSAR) are numerous. Several advantages of dInSAR techniques compared to traditional techniques have been summarised (Herrera et al. 2007; Tomás et al. 2005). These include the high spatial coverage of SAR data (especially over urban areas), whilst ground-based techniques are able to measure only at discrete points (Herrera et al. 2007; Yen et al. 2007). Furthermore, dInSAR is more favourable for visual interpretation of deformation compared to point-based measurements (Yen et al. 2007). Additionally, while levelling techniques can be employed to cover large areas, the measurements cannot be made at such frequent time intervals since the associated costs are too high. Consequently, dInSAR complements field-based techniques by providing a synoptic view and overcoming limitations due to inaccessibility of field areas (Carnec & Raucoules 2000).

DInSAR can be incorporated into a monthly or annual monitoring service at lower cost than could be provided using traditional techniques (Herrera et al. 2007). Several studies have compared dInSAR results with traditional geodetic techniques (Carnec & Delacourt 2000; Herrera et al. 2007; Liu et al. 2004; Massonnet & Feigl 1998; Raucoules et al. 2003b; Tomás et al. 2005). They found that dInSAR measurements frequently compare well with these ground-based methods (Guéguen et al. 2009; Raucoules et al. 2003b; Simonetto et al. 2005) and that the associated cost compared to ground-based approaches is significantly lower (Herrera et al. 2007). However, GPS-based measurements frequently provide a more accurate measure of deformation than interferometry-based measurements, with the detection of very slow movements being a possibility (Smith 2002). Despite these aspects, the primary

advantage of dInSAR measurements over GPS is that measurements can be made in the absence of fieldwork, while providing a synoptic view as opposed to point-based measurements (Smith 2002).

Radar remote sensing technologies can be used as a predictive tool in the field of risk management in terms of assessing the potential of a particular area to be affected by a specific geohazard. Radar interferometry can also play a role in determining the extent of the area influenced by a geohazard after the event, which will be a powerful tool for disaster management and formulation of compensation or relief strategies. This research assesses the potential of radar interferometry for geohazards assessment with particular focus on deformation due to mining activities in South Africa, including possible applications as a predictive tool and for post-event assessments.

1.2 PROJECT AIMS AND GOALS

This study aims to test the application of radar interferometry techniques for geohazard assessment in South Africa. Conventional differential interferometry (dInSAR) techniques will be applied to study surface deformation associated with coal mining activities in the Mpumalanga Province of South Africa. To curb the problems associated with traditional interferometry techniques, a relatively new technique, known as polarimetric interferometry (polInSAR) will also be tested to determine its ability to detect surface deformation. The availability of ground-truth data in the study area implies that the area is suitable for methodology development of advanced dInSAR techniques. Successful methodology development will imply that the methodology can be applied to determine surface deformation where such deformation is expected, but not yet proven. In this regard, recommendations for an operational monitoring system using interferometric techniques that can be employed for long-term monitoring of abandoned and active underground mining activities will be made. The detection of surface deformation or lack thereof in these areas will be important for future development planning and subsidence risk assessment.

1.3 GEOHAZARDS IN SOUTH AFRICA AND STATEMENT OF THE PROBLEM

The geohazards influencing South Africa are numerous and include the occurrence of landslides, earthquakes, movement along faults, sinkholes and other surface deformations associated with mining activities. Most of these hazards can produce disaster events with no prior warning. This is particularly

true in the case of landslides, earthquakes and sinkholes. Although systems to predict accurately the occurrence, magnitude and location of such hazards have not been designed, the susceptibility of an area to geological hazards can be determined. In this regard, the ability to detect, measure and monitor small scale surface movements will be critical in determining the hazard of an area to be influenced by geological hazards. In the case of surface subsidence and deformations associated with mining activities, mining companies are aware of the problem. In these cases, traditional surveying methods (such as spirit levelling and GPS surveying) are employed at a number of locations. However, these methods are expensive in terms of cost and manpower, meaning that measurements are only made at a limited number of point locations. This means that the full extent of subsidence basins, their evolution over time and the associated impact on the environment is poorly understood.

The limitations associated with ground-based surveying techniques imply that a means of remote monitoring of the particular geohazard in question would be ideal to gain understanding of that hazard. Here, radar remote sensing techniques can contribute to the monitoring of the particular hazard since they provide the ability to obtain deformation measurements over large areas. Furthermore, the availability of interferometric synthetic aperture radar (InSAR) data since 1991 also implies that historical datasets are available for studying the evolution of a variety of geohazards over time (Raucoules et al. 2007).

The application of interferometry techniques to study surface deformations associated with geohazards is well established with numerous researchers achieving accurate results (Anderson 2007; Cakir et al. 2005; Carnec & Delacourt 2000; Chang et al. 2004; Herrera et al. 2007; Liu et al. 2004; Massonnet et al. 1993; Massonnet et al. 1995; Massonnet & Feigl 1998; Perski & Jura 2003; Raucoules et al. 2003b; Smith 2002; Tomás et al. 2005; Yen et al. 2007). However, many studies also describe a number of limitations to the use of dInSAR for investigating surface deformations (Carnec & Delacourt 2000; Massonnet & Feigl 1998; Perski & Jura 2003; Raucoules et al. 2007). The most limiting factor is the loss of interferometric coherence as a result of vegetation and land cover changes over time. Several advanced dInSAR approaches have been developed to overcome this limitation. Two such approaches, known as permanent scatterer interferometry (PSI) and small baseline subset (SBAS) techniques, consider only those pixels that remain coherent in the interferometric datasets (Berardino et al. 2002; Euillades et al. 2011; Ferretti et al. 2001; Galloway & Hoffman 2007; Mora et al. 2003; Raucoules et

al. 2007; Tomás et al. 2005). These techniques enable a reduction in errors associated with temporal and geometric decorrelation, and reduces atmospheric artefacts. However, researchers found that this technique could not be employed over rural areas (Perski & Jura 2003). This is a result of insufficient stable pixels in rural areas over time. Consequently, the main problems associated with temporal and geometric decorrelation still remain a drawback in these areas.

It is therefore proposed to employ the polarimetric interferometry (polInSAR) technique for geohazard assessment in rural areas. This technique combines information obtained from fully polarimetric radar data and traditional dInSAR approaches to maximise interferometric coherence (Boerner & Verdi 1998; Cloude & Papathanassiou 1997; Navarro-Sanchez et al. 2010; Papathanassiou & Cloude 2001; Pipia et al. 2009; Sagués et al. 2001). PolInSAR approaches have traditionally been applied to determine tree height in forested regions, as well as for the study of glacier properties and their movement (Öttl et al. 2000; Stebler et al. 2005) but have also been adopted for differential applications (Navarro-Sanchez et al. 2010; Pipia et al. 2009).

1.4 HYPOTHESIS STATEMENT AND RESEARCH QUESTIONS

Hypothesis statement: Differential polarimetric interferometry provides an enhanced ability to measure mining-induced subsidence compared to traditional single polarisation interferometry approaches

Following the broad hypothesis we aim to answer the following specific research questions:

- Can dInSAR techniques be employed to study surface subsidence associated with mining activities in South Africa?
- What advances can be achieved by using polInSAR techniques that could not be achieved by using traditional interferometry approaches?
- Can polInSAR techniques overcome coherence limitations associated with vegetation and land cover changes over time?
- What are the operational limitations of dInSAR for long-term monitoring of mining-induced surface deformation

The ultimate objective of this research is to examine the operational limitations of dInSAR technology for the long-term monitoring of mining-induced deformation in a highly dynamic agricultural region. The known limitations of traditional dInSAR approaches in the presence of disturbances to reflected signals due to agricultural activities will be addressed by testing polInSAR techniques for their ability to enhance interferometric coherence and to detect surface movement in the areas of interest. The availability of ground-truth data in the study area provides an ideal resource for the purpose of methodology development and determination of the accuracy to which polInSAR techniques can be used to measure surface deformations in areas where vegetation and land cover changes will negatively influence the ability to perform deformation measurements using traditional dInSAR techniques.

A number of questions were raised during the 3rd International workshop on the Science and Applications of SAR Polarimetry and Polarimetric Interferometry held in Frascati, Italy (January 2007). Specifically, the following seed questions[1] were aired:

1) Is there any demonstrated benefit of multi-baseline polInSAR?

2) What are the potential polInSAR applications that can be demonstrated?

The current research will aim to address these questions by investigating the ability of polInSAR techniques to monitor surface deformations in a selected study area in South Africa. The research will make a novel contribution to polInSAR for deformation measurements by investigating the ability of the polInSAR techniques to assess mining-induced deformation in a highly dynamic agricultural environment in South Africa. This will provide the opportunity to determine which improvements polInSAR can offer over traditional interferometric techniques for deformation monitoring. Additionally, operational requirements and recommendations for the long-term monitoring of deformation using dInSAR techniques will be made.

1.5 DESCRIPTION OF THE STUDY AREA – SUBSIDENCE IN THE WITBANK COALFIELDS

The area focussed on in this investigation, is situated in a coal mining region in the Mpumalanga Province of South Africa which is also subject to commercial agricultural activities. The main crop types include maize, sunflowers and soya in addition to pasture (Figure 1). Planting of crops usually

[1] http://earth.esa.int/workshops/polinsar2007/POLinSAR_2007_Seed_Questions.htm

takes place between October and the end of November. Both soya and sunflowers ripen by the end of March, at which time the leaves of the plants disintegrate, significantly lowering the leaf area index and the vegetation biomass. Maize is usually harvested in June except in cases where the maize is used as fodder, when harvesting can take place earlier. When maize ripens, plant leaves do not disintegrate as is the case with sunflower or soya which means that the plant retains its biomass until harvesting. After harvesting, leaves, stalks and other debris will be left over and scattered throughout the fields.

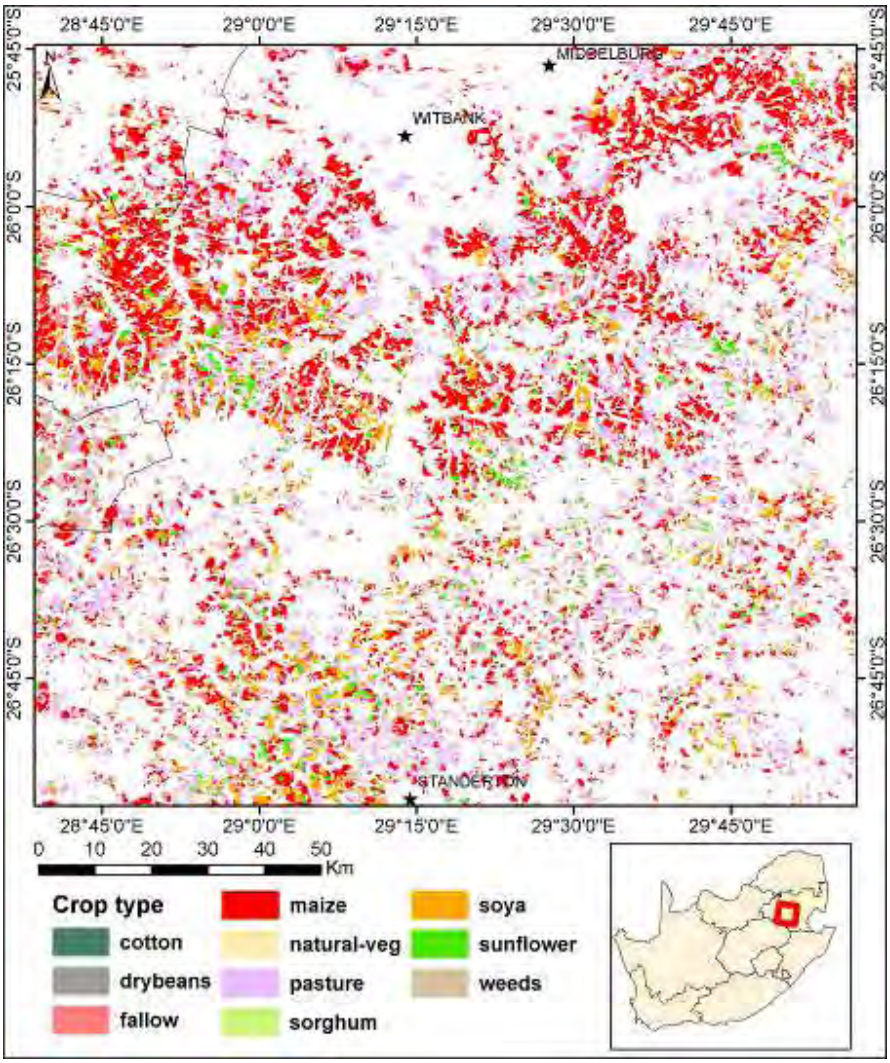

Figure 1: Agricultural activities in the region of interest.

Coal mining activities in the region since the turn of the 20th century have changed the natural environment in several ways. Current challenges for mining companies lie in rehabilitating the natural

environment and preventing further environmental degradation. One particular area of concern is surface deformation associated with mining activities. Mining subsidence associated with underground coal mining is, in theory, a gentle, gradual settling of the earth's surface (Perski & Jura 2003). Underground mining cavities can result in a lowering of the earth's surface (hereafter referred to as surface subsidence) as a result of the collapse of bedrock and the subsequent sinking of unconsolidated surface sediments (Perski & Jura 2003). Some of the primary effects of the collapse of underground cavities include the appearance of tension cracks and crownhole development. The effects of surface subsidence on the built environment are severe and include damage to infrastructure (roads, dams, pipelines and buildings) (Raucoules et al. 2007). Such damage can amount to millions of Rands and can have severe legal consequences for the mining companies involved. The effects of surface subsidence on the natural environment include the alteration of hydrological pathways. The ponding of water in subsidence basins results in an increase in groundwater recharge. The groundwater circulating through mining cavities becomes polluted and discharges into the natural environment contaminating wetlands, streams and dams. For the mining companies involved, it is necessary to know where subsidence is occurring, how the ground is moving and how fast subsidence is progressing. With this knowledge, informed decisions on current and future infrastructure development can be made and remedial actions and prevention strategies can be formulated for the problems associated with environmental degradation (Engelbrecht et al. 2011).

In the Witbank Coalfields, the room and pillar technique (also called bord and pillar) was the extraction technique of choice in the early days. The room and pillar technique is a system in which mined material is extracted across a horizontal plane while leaving pillars of untouched material to support the overburden (Bell et al. 2001; McCarthy & Pretorius 2009). The key to successful room and pillar mining is selecting the optimum pillar size. If the pillars are too small the mine will collapse. If the pillars are too large then significant quantities of valuable materials will be left behind reducing the profitability of the mine. Initially, little or no environmental degradation was associated with the mining activities in the coalfields in the Witbank area. However, a pillar-robbing program in the late 1930's had a marked effect on the environment. In the pillar robbing stages of mining, the pillars were quartered, leaving four smaller pillars at the corners, meaning that approximately 25% of the original pillar was left intact (Bell et al. 2001). This increased the stress on the remainder of the pillars, eventually leading to pillar collapse.

The primary effects of the pillar robbing programme included surface subsidence (several hundreds of square kilometres in extent), the appearance of tension cracks and crownhole development. Secondary effects included the spontaneous combustion of the remaining coal as well as a negative impact on groundwater resources in the area (Bell et al. 2001). The burning of coal accelerated the weakening of the pillars and the collapse of inter-pillar tensional areas resulted in upward void migration through the overlying strata until the weathered zone was reached. In general, the weathered material has subsided by 2 to 3 metres, but in some cases the material collapsed totally into the old workings, leaving voids 15 to 20 m deep. The resultant crownholes at the surface have diameters between 5 and 10 m (Bell et al. 2001). Both gradual subsidence and sudden collapse are accompanied by surface deformation including fractures, crevices, faults, step folds and slides (Perski & Jura 2003). Both primary and secondary effects of the pillar-robbing programmes are visible today. The photographs below (captured on 9 and 10 September 2008) each portray the effects of the pillar robbing program including surface subsidence (Figure 2), tension cracks (Figure 3) and sinkhole development (Figure 4). The burning of the remaining coal is represented in Figure 5 where smoke is rising from a tension crack on the surface.

Figure 2: Pylon affected by subsidence basin formation in the Middelburg area.

Figure 3: Tension cracks representing secondary features of surface subsidence.

Figure 4: Sinkhole developed in areas associated with pillar robbing programmes also showing openings into underground workings.

Figure 5: Smoke and steam produced by burning coal below the surface rising from a surface opening.

Present day mining activities (open-cast and underground activities presented in Figure 6) are also associated with surface subsidence features although these features are less pronounced than those associated with the abandoned mines. Currently primarily two mining techniques are employed including the room and pillar technique, as well as a technique known as longwalling. The longwall mining technique is a form of underground mining where a longwall of coal is mined in a single slice and the roof is allowed to collapse into the void (McCarthy & Pretorius 2009). The longwall panel (the block of coal being removed) is typically 3 to 4 km long and 250 to 400 m wide. The roof strata between the remaining roof support structures are subject to sagging leading to surface subsidence at the surface. This may cause a characteristic wave-like propagation of subsidence features on the surface. The advantages of longwall mining compared to the room and pillar method include the fact that there is a greater resource recovery and less roof support consumables are needed and surface subsidence is largely immediate. The surface subsidence associated with longwall mining is referred to as controlled subsidence with mining companies anticipating the deformation which allows for better planning.

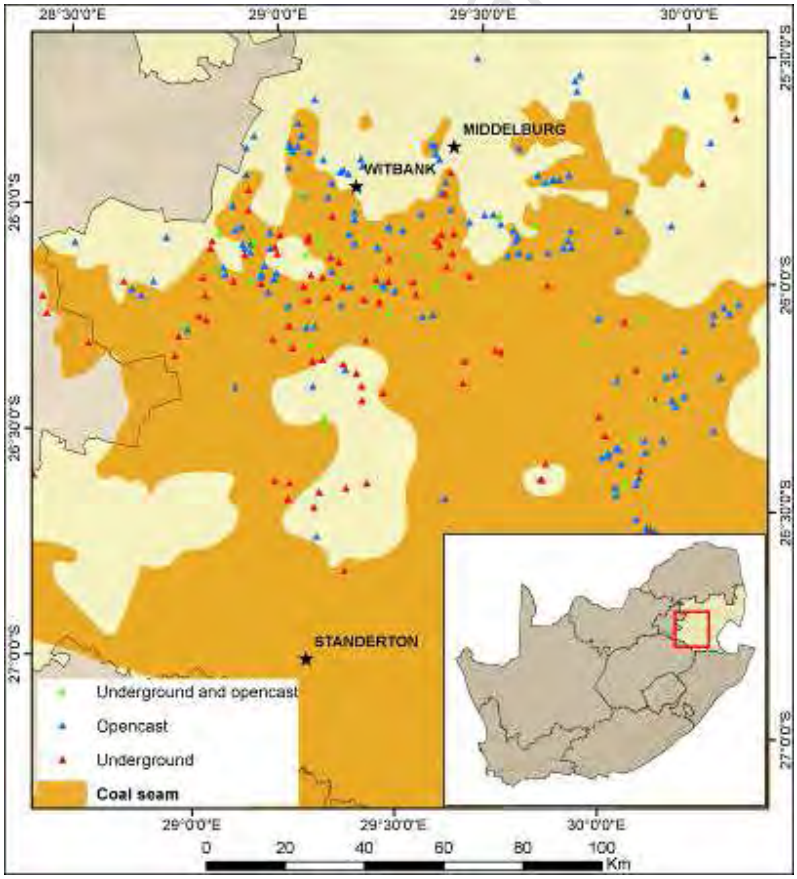

Figure 6: Coal mining activities in the area of interest in the Mpumalanga province of South Africa.

The severity of the impact of coal mining depends on various parameters including the mining methods used the local geological conditions and whether the mine is working or abandoned (Bell et al. 2001). In particular, the composition of the roof strata will influence the expression of surface subsidence on the surface. These statements are supported by the fact that varying conditions between the Witbank/Middleburg area and the Standerton area lead to different expression of surface subsidence being observed. The Witbank/Middelburg areas of the coalfields are coincident with roof strata composed of shales while in the Standerton area, roof strata are composed of sandstones. The sandstones, being more competent will be less susceptible to deformation while the less competent shales will be more susceptible to gradual movements. Additionally, the coal seam in the Witbank area is between 0 and 80 m below the surface with the thickness of the coal seam ranging between 4 and 4.5 m. On the other hand, mining at the Standerton area takes place approximately 200 m below the surface while the thickness of the coal seam is between 2 and 2.5 m.

In addition to the geological conditions, the mining method also influences the expression of surface subsidence with the room and pillar method being employed in the Witbank/Middelburg area whilst the longwall method is used in the Standerton area. These factors combine to produce different patterns of surface subsidence. The Witbank/Middelburg area is prone to subsidence basins that subside by between 2 to 3 metres (Figure 7) while deformation in the Standerton area is less pronounced with subsidence reaching a maximum vertical deformation of between 0.4 and 0.8 m (Figure 8). The secondary effects of surface subsidence such as the appearance of tension cracks are also more pronounced in the Witbank/Middleburg area (Figure 9) while they remain virtually underdeveloped in the Standerton area.

Figure 7: Subsidence basin observed in an agricultural field in the Witbank area.

Figure 8: Subsidence basin observed in an agricultural field in the Standerton area.

Figure 9: Tension cracks associated with subsidence basin formation developed in an agricultural field in the Witbank area.

Ground-based programmes for the monitoring of the surface subsidence in the coalfields have been established in certain locations. The traditional way of monitoring surface subsidence is by using geodetic techniques such as spirit levelling and GPS surveys. The problems associated with ground-based techniques for measuring surface subsidence have been described (Raucoules et al. 2007). These include the difficulties associated with frequent field visitations, variations in the precision of measurements and difficulties in accessing monitoring sites in isolated areas. Furthermore, these techniques are expensive in terms of man-power and cost and consequently the strategy of most mining companies is to measure as little as possible (Perski & Jura 2003). The techniques also rely on point-based measurements implying that the full extent of the subsiding area is not well recognised and is poorly understood. Furthermore, the need to monitor subsidence associated with abandoned mines has been recognised by the mining companies involved.

To overcome the limitations associated with traditional techniques for monitoring surface subsidence, differential radar interferometry (dInSAR) techniques are proposed for the study of mining subsidence in the Mpumalanga Province. DInSAR measurements will provide a synoptic view of the study area (Guéguen et al. 2009) whilst historical data availability will imply that the extraction of information on the spatial and temporal evolution of subsiding areas will be a distinct possibility (Anderson 2007;

Guéguen et al. 2009; Herrera et al. 2007; Massonnet & Feigl 1998; Tomás et al. 2005). Furthermore, the dInSAR technique can be employed to monitor extensive areas at a fraction of the cost of traditional ground-based techniques (Anderson 2007; Herrera et al. 2007).

To test the dInSAR technique for its ability to monitor surface deformation due to underground mining activities, an area undergoing longwall mining was selected to be the focus of this investigation. This area was selected since, at the time of investigation, it was undergoing active mining. Additionally, subsidence was known to be associated with the underground mining and was planned for. This implied that new acquisitions of SAR scenes could be commissioned with the desired attributes (temporal frequency of acquisitions and polarisation) to test the hypothesis and research questions posed in Section 1.4. The background to SAR, dInSAR and its limitations as well as advanced interferometry techniques are provided in Section 2. Examples of the use of dInSAR techniques for deformation measurement are also provided. The SAR scenes and ancillary data acquired for this investigation are introduced in Section 3 and the data processing sequence is presented. The parameters affecting successful deformation measurements are investigated in Section 4 together with the results of polInSAR processing. The results of the deformation monitoring are presented in Section 5. The discussion on the results and their implications for long-term monitoring is presented in Section 6 and 7.

The monitoring of mining-induced subsidence will enable the understanding of the evolution of subsidence basins and the consequent long-term impacts on the environment. With this knowledge, informed decisions on current and future infrastructure can be made. Radar interferometry is believed to provide a means to monitor subsidence in mining areas at a fraction of the cost of traditional ground-based techniques. Furthermore, the coalfields in the Mpumalanga Province are believed to be an ideal study area for developing and testing advanced DInSAR approaches for measuring and monitoring surface deformations in South Africa. Not only is the area known to be subsiding, but the availability of ground-truth data in certain locations will provide the means for testing the accuracy of the methodology and its results.

2 LITERATURE REVIEW AND METHODOLOGY

Synthetic aperture radar (SAR) images are formed by recording the phase (time delay) and amplitude (energy intensity) of microwave echoes returned from the earth's surface (Massonnet 1995; Smith 2002). The phase measured by the SAR antenna is related to the round-trip distance between the antenna and the earth's surface (Blaes & Defourny 2003). Any ground motions that transpire in the radar line-of-sight direction would result in a slight increase or decrease in round-trip distance, causing an offset in phase (Smith 2002). The interference pattern caused by the phase differences between two images captured at different times or different locations can be calculated, resulting in an interferogram (Chang et al. 2004; ESA (European Space Agency) 2005; Liu et al. 2004; Massonnet & Feigl 1998; Smith 2002). This process is called radar interferometry.

An interferogram provides information about height variations present on the imaged surface. Therefore, using radar interferometry, detailed three-dimensional relief maps (or digital elevation models) of the earth's surface can be produced from multiple-pass synthetic aperture radar (SAR) data sets (Ferretti et al. 2001). Furthermore, the phase difference information in an interferogram can be adjusted to compensate for topography, resulting in information that can be related to very small relative movements of the ground surface (centimetre or millimetre scale) (ESA (European Space Agency) 2005; Euillades et al. 2011; Ferretti et al. 2001; Prati et al. 2010). This is called differential synthetic aperture radar interferometry (DInSAR).

Although the interferometric phase is sensitive to the topographic relief and surface motions that occur between two image acquisitions, this phase is really the addition of different contributing parameters including: 1) a flat earth and topographic component; 2) an atmospheric component; 3) an orbital component; 4) phase noise; and 5) the deformation component (Chang et al. 2004; Liu et al. 2004; Massonnet & Feigl 1998; Mora et al. 2003; Raucoules et al. 2003b; Raucoules et al. 2007). Additionally, a sixth component due to data processing errors can also add to interferometric phase (Liu et al. 2004). To exploit the interferometric phase to derive a measure of surface deformation or motion, the components listed in 1 to 4 and 6 above need to be removed from the interferogram. The following sections (Section 2.1) describe the removal of these components from the interferograms, providing the potential to remain with only the deformation component.

2.1 INTERFEROMETRIC PHASE CONTRIBUTIONS AND THEIR REMOVAL

2.1.1 Removal of the flat earth (orbital) and topographic components

The generation of SAR interferograms relies on the acquisition of two SAR scenes captured at different times or antenna positions. The positions of the antennas at the respective times of image capture can be described by a parameter known as the interferometric baseline. The interferometric baseline is defined as the cross-track orbital separation (or distance) between two satellite positions. For interferometric analysis, the component of importance is the component perpendicular to the SAR slant-range vector (known as the perpendicular baseline) (Figure 10).

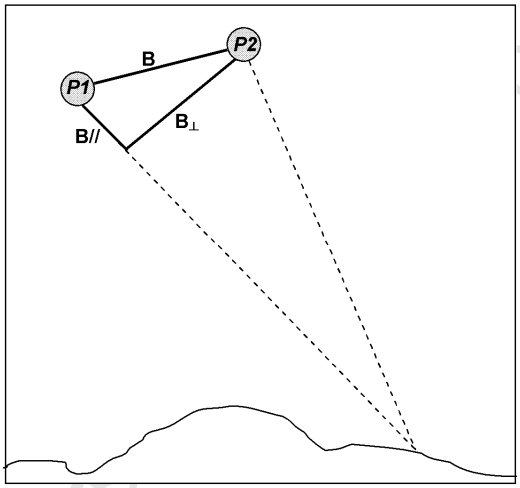

Figure 10: The baseline (B) associated with two antenna positions (P1 and P2) and associated parallel (B//) and perpendicular ($B^{\perp}$) components.

The separation of the antenna at the times of image capture results in two distinct phase contributions affecting the interferogram namely the flat-earth and topographic components. The flat-earth or orbital phase contribution is imposed by the variations in the positions of the antenna at the time of image capture which results in a phase difference between scattering elements at the same height. This low frequency phase contribution can be removed through orbital modelling from precise orbital data (Liu et al. 2004). In addition to the flat earth phase contributions, topographic variations on the earth surface will also contribute to the interferometric phase and is affected by the perpendicular baseline. If the antenna positions are exactly the same, the resulting interferometric phase can be attributed purely to ground displacements. On the other hand, as the perpendicular baseline increases, additional cycles of

interferometric phase are introduced due to topographic variations (Smith 2002). This implies that larger perpendicular baselines are more sensitive to topographic relief. The sensitivity to topography can be expressed by a parameter known as the ambiguity height. The ambiguity height (H_a) is calculated as $H_a = \frac{\lambda R \sin(\theta)}{4\pi B_\perp}$ where λ is the wavelength, R is the range distance, θ is the incidence angle and $B_\perp$ is the perpendicular baseline. The sensitivity to height variations in an interferogram is inversely proportional to the ambiguity height with large H_a values associated with a decreased sensitivity to height variations.

Two techniques can be used to remove the topographic phase contributions from the interferogram. The first technique relies on the availability of an external source of elevation data (Chang et al. 2004; Massonnet & Feigl 1998; Raucoules et al. 2003b; Raucoules et al. 2007; Smith 2002). When using an external digital elevation model (DEM) for the removal of the topographic phase, successful removal of topographic phase will depend on successful co-registration of the DEM, the quality of the DEM and the perpendicular baseline between the interferometric image pairs (Raucoules et al. 2007). If the DEM used to eliminate the topographic contribution is in error and if the error is significant with respect to the ambiguity height, the interferogram will contain residual topographic phase contributions. These artefacts will appear in the same location in every interferogram produced using that DEM, making them easily recognisable (Massonnet & Feigl 1998; Mora et al. 2003). However, it is possible to misinterpret such phase residues as deformation if the deformation field resembles the topographic surface. Therefore, the selection of interferometric pairs of images with a short as possible perpendicular baseline will increase the sensitivity to mapping surface deformations whilst lowering the requirement on the accuracy of the external DEM (Liu et al. 2004). It should be noted that freely available DEM data provided through the SRTM mission is generally regarded as sufficient for conventional dInSAR approaches even with moderate perpendicular baselines, assuming moderate relief.

A second technique for the removal of topographic phase is by subtracting previously generated topography-only interferograms. Topography-only interferograms are interferograms generated during a time-frame when it is known that no deformation has taken place. Since larger perpendicular baselines are more sensitive to elevation changes, large baselines are preferred for the creation of these

topography-only interferograms resulting in the detection of smaller elevation variations. However, larger perpendicular baselines lead to an increase in phase noise. Consequently, the creation of topography only interferograms requires a moderate baseline to find a balance between the phase sensitivity to elevation changes and phase noise (Liu et al. 2004). To ensure the use of interferometric pairs with a low probability of containing a deformation component, tandem pairs of images, captured at 1-day intervals, have been considered (Liu et al. 2004). The 1-day difference between image acquisitions ensures that the phase contribution resulting from surface deformation can be considered as negligible since significant surface deformation is generally unlikely over such a short time period.

2.1.2 Recognising the atmospheric component

After removal of the flat earth and topographic component, the differential interferogram is composed of residual topographic phase due to DEM errors (which is proportional to perpendicular baseline and easily identifiable if a time series is used) as well as an atmospheric phase contribution. Unlike residual topographic phase, the atmospheric component is generally highly variable over time (Mora et al. 2003). However, in areas with high relief, atmospheric effects could also be correlated with altitude and, consequently, may also be temporally correlated. An atmospheric phase contribution can be present in interferograms due to spatial and temporal fluctuations of the atmosphere (variations in water vapour and ionospheric disturbances) between the satellite and target (Chang et al. 2004; Massonnet & Feigl 1998; Raucoules et al. 2003b; Raucoules et al. 2007; Smith 2002). Any difference in the troposphere or the ionosphere between two dates of image acquisition can change the apparent length of the path between the radar and the ground, causing an apparent phase change in the interferogram (Ferretti et al. 2001; Mora et al. 2003). Effects will also be present in turbulence caused by forming storm clouds or by interaction of high winds and relief. Such effects can look similar to deformation signatures and may therefore corrupt interferogram interpretation (Prati et al. 2010; Raucoules et al. 2003b). Slight radar signal delays due to atmospheric variations can result in significant height errors in InSAR DEMs and centimetre-scale errors in displacement measurements (Smith 2002).

The atmospheric error in dInSAR application can be significant, especially when millimetre-scale surface displacements are investigated (Le Mouélic et al. 2005). To minimise potential atmospheric phase contributions, interferograms derived from night-time scenes can be used since they show fewer

and smaller atmospheric artefacts than do daytime scenes (Massonnet & Feigl 1998). This may be a result of the more quiescent state of the vegetation and the statistically more stable atmosphere at night. Atmospheric artefacts can be identified and partially distinguished from deformation signals by comparing several interferograms generated from SAR images from different dates (Massonnet & Feigl 1998; Raucoules et al. 2003b; Raucoules et al. 2007) . Using this technique, atmospheric effects can be identified since their fringe structure is independent over several interferograms. Additionally, interferograms from both ascending and descending orbits have been used compare their fringe patterns. If the overall fringe pattern is the same for the different orbits, no significant atmospheric signature is present on the scenes (Akoglu et al. 2006).

A technique for mitigating atmospheric effects by averaging multiple interferograms has been described (Chang et al. 2004; Raucoules et al. 2003b; Yen et al. 2007). By combining the sets of interferograms, the artefacts related to atmospheric effects can be reduced since the atmospheric artefacts superimposed on the interferograms are uncorrelated (Chang et al. 2004; Raucoules et al. 2007). Since atmospheric conditions are different every day, the atmospheric phase screen does not correlate over time and by averaging the interferograms over time the resulting deformation map should exhibit fewer atmospheric-phase contributions than any individual interferogram (Yen et al. 2007). Such advanced dInSAR techniques (described in Section 2.3.1) can be used to eliminate the atmospheric ambiguities from interferometric measurements (Ferretti et al. 2001).

2.1.3 Phase noise

Scene coherence can be considered as the cross-correlation between the phases of two signals and can be calculated to estimate the phase noise component of interferograms. Formally, interferometric coherence (γ) is defined as:

$$\gamma = \frac{\left|\sum s_1(x) \cdot s_2(x)^*\right|}{\sqrt{\sum |s_1(x)|^2 \cdot \sum |s_2(x)|^2}}$$

where $s_1(x)$ is the complex signal of scene 1 at pixel x and $s_2(x)$ is the complex signal of scene 2 at pixel x. Interferometric coherence presents a measure of the correlation between two points on the input scenes and ranges between 0 and 1 with 0 indicating total decorrelation and 1 indicating complete correlation. The calculation of coherence in this manner means that the different sources of noise

cannot be discriminated through the above formulation. However, the phase noise is related to systemic spatial decorrelation resulting from baseline effects (additive noise), and to temporal decorrelation between master and slave acquisitions (SARscape 2009).

Phase noise can be introduced into interferograms as a result of various factors which include spatial baseline decorrelation, decorrelation due to the rotation of the target and incoherent changes in the physical characteristics of the target between observations and decorrelation from surface motion of individual scattering centres (Raucoules et al. 2007; Zebker & Villasenor 1992). These sources of decorrelation are usually referred to as geometric and temporal decorrelation effects. Additionally, thermal noise and processing errors can contribute to the noise component in interferograms (Chang et al. 2004; Grey & Luckman 2001; Liu et al. 2004; Stebler et al. 2002). Of these components, the thermal noise component is usually considered to be negligible (Liu et al. 2004). The individual contributions of temporal decorrelation, baseline decorrelation and volume decorrelation have been defined and can be summarised as:

$$\gamma = e^{i\phi_s}\gamma_{SNR}\gamma_t\gamma_{proc}\gamma_s\gamma_v$$

where γ_{SNR} is decorrelation due to additive noise in the signals, γ_t is temporal decorrelation due to motion of scatterers between image acquisitions, γ_{proc} is the loss of coherence due to processing errors, γ_s is baseline decorrelation and γ_v is volume decorrelation (Cloude 2010).

Phase noise is considered to be one of the most limiting factors influencing successful dInSAR measurements since it hampers the identification of the phase contribution due to topography and displacement (Raucoules et al. 2007). Sources of temporal and geometric decorrelation of the interferometric signal have been described in detail (Raucoules et al. 2007; Zebker & Villasenor 1992) and will be further explored in Section 2.2.

2.1.4 Extracting the deformation component

The extraction of the deformation component in an interferogram will depend on the successful removal of the contributions discussed in Sections 2.1.1 to 2.1.3 above. Once all the other components have been accounted for, the deformation component can be interpreted to assess surface movement.

Interferograms containing only the deformation component result in a dataset in which one interferometric fringe corresponds to displacement equalling half a wavelength of the radiation transmitted by the sensor (Raucoules et al. 2003b). Consequently, the sensitivity of the dInSAR to deformation is dependent on the wavelength of the sensor since a relative displacement (*d*) of $d = \frac{\lambda}{2}$ (where λ is the wavelength) generates a differential phase variation ($\Delta\phi_d$) of $\Delta\phi_d = 2\pi$ radians. This means that shorter wavelength data is more sensitive to small scale deformation compared to longer wavelength data (Prati et al. 2010) assuming no external sources of inaccuracy. Irrespective of the wavelength of the data, the ability to successfully and accurately extract surface deformation measurements is limited by the phase noise term. Section 2.2 explores the phase noise and other limitations associated with dInSAR measurement in more detail.

2.2 LIMITATIONS ASSOCIATED WITH DINSAR FOR GEOHAZARDS ASSESSMENT

Although numerous advantages are associated with the use of dInSAR techniques for surface deformation measurement, various limitations are also described. The problems relate mostly to phase noise that are introduced into interferograms due to various parameters including temporal and geometric attributes (Kervyn et al. 2006; Tanase et al. 2010). Additional limitations involve the deformation gradient limit of the sensor and other sensor and image limitations (Massonnet & Feigl 1998).

A fundamental condition for interferometry is that the maximum detectable deformation gradient is one fringe per pixel (also the dimensionless ratio of pixel size to wavelength) (Jiang et al. 2009; Massonnet & Feigl 1998; Zhou et al. 2009). However, this is only true on the assumption that no additional sources of phase decorrelation are present. If the relative displacement between two neighbouring pixels exceeds one fringe, the displacement cannot be detected (Zhou et al. 2009). For C-band data (~5.6 cm wavelength) with a pixel size of 10 m, the gradient limit implies that, for successful deformation measurement, the surface deformation cannot exceed 2.8 cm per 10 m. For longer wavelength L-band data with a wavelength of ~23 cm, the gradient limit would be ~11.5 cm per pixel. Strains that produce deformations larger than the gradient limit in a period of time shorter than the

satellite's orbital cycle will be inaccessible using radar interferometry techniques (Raucoules et al. 2007).

A deformation gradient exceeding this gradient limit would result in decorrelation of the interferometric signal, producing phase noise. The gradient limit therefore also imposes a limitation on the day difference between master/slave image acquisitions with gradual deformation over extended areas allowing for the use of longer temporal baseline data and rapid deformation over smaller areas requiring shorter temporal baselines (Massonnet & Feigl 1998; Perski & Jura 2003; Zhou et al. 2009). A possible solution in areas where the deformation gradient locally exceeds the gradient limit is to subtract digital elevation models created both before and after a deformation event (Smith 2002). This will provide the ability to measure surface deformations larger than the gradient limit.

A further restriction, concerns the pixel size of the SAR images, which imposes its own limitation (Massonnet & Feigl 1998). Interferometric measurements are meaningless on a single pixel, since the pixel can include noise in an unpredictable way. Successful interpretation of deformation depends on the agreement of several neighbouring pixels. Consequently, using traditional dInSAR techniques, geophysical phenomenon will be difficult or impossible to recognise unless it is at least 10 pixels wide (Massonnet & Feigl 1998). However, to overcome this problem, advanced dInSAR techniques have been developed which enables the extraction of deformation measurements on point targets. These advanced approaches are introduced in Section 2.3.1.

An additional limitation for detecting surface deformations using dInSAR techniques lies in the fact that only line-of-sight (LOS) deformations are recorded using a single interferometric pair (Akoglu et al. 2006; Manzo et al. 2006; Massonnet 1995; Yen et al. 2007). Therefore, a change in phase could either imply a vertical motion or horizontal motion to the east or west (for descending or ascending orbits respectively) (Yen et al. 2007). Therefore, there is an ambiguity when an interferogram indicates an increase or decrease in slant range. The ambiguity between vertical and horizontal movements can be partially compensated for by the use of both ascending and descending passes, which provide additional information at the cost of higher processing complexity (Akoglu et al. 2006; Manzo et al. 2006; Massonnet 1995; Smith 2002). If only a single interferometric pair is available, the knowledge of the local geological structure may eliminate most ambiguities. However, without a priori knowledge, a

solution is provided by the fusion of dInSAR and GPS data (Akoglu et al. 2006). A GPS can record three components of displacement, while providing greater precision in horizontal motions (Akoglu et al. 2006; Yen et al. 2007). Additionally, a smaller radar incidence angle will provide a greater sensitivity to vertical motion and diminished sensitivity to horizontal movement (Yen et al. 2007).

Although dInSAR techniques are successful in monitoring surface deformation, the phase decorrelation effects due to temporal and geometric sources are described as the most limiting factors (Prati et al. 2010; Reigber et al. 2007). Geometric decorrelation effects are introduced due to the variation in the target reflectivity as a function of the incidence angle of the signal (Prati et al. 2010). This results from the relative position of the sensor at the time of master/slave image capture as assessed by the perpendicular baseline (Section 2.1.1) and the Doppler centroid difference. The perpendicular baseline affects the phase noise with larger perpendicular baselines resulting in lower interferometric coherence when compared to shorter perpendicular baselines (Canaslan & Ustun 2012). The perpendicular baseline has to be below the theoretical maximum value (the critical baseline) since, for baselines higher than the critical baseline, targets would no longer be correlated. It should be noted that the land surface characteristics will affect the sensitivity to baseline decorrelation effects. Specifically, an increased sensitivity to baseline decorrelation effects (induced by the change in incidence angle) is observed for increasing radar backscatter from vegetation canopies (Papathanassiou & Cloude 2005). If the backscatter contribution is from the surface, the geometric decorrelation effects are minimised. The interferometric coherence as a function of surface and volume scattering has been mathematically defined (Papathanassiou & Cloude 2005). However, surface roughness effects will also affect the sensitivity to baseline decorrelation. The backscatter contributions from smooth surfaces have been found to be more sensitive to changes in the local incidence angle compared to rough surfaces (Farr 1993). Consequently, large changes in the local incidence angle imposed by large perpendicular baselines will affect the coherence of smooth surfaces more than rough surfaces.

Another source of geometric decorrelation is known as the Doppler centroid difference between master-slave image pairs. Since the satellite transmitting the microwave radiation is moving relative to the Earth's surface, the returned signal will reflect a change in frequency relative to the transmitted frequency. This is known as the Doppler Effect. Slight changes in the attitude and velocity of the satellite implies that this frequency shift will vary along the line of flight of the satellite. The Doppler

centroid is an estimate of the centre frequency of the Doppler spectrum of the data (Rosich et al. 2000). The Doppler centroid difference of two image pairs is the difference in hertz (Hz) between Master image and Slave image Doppler centroids. As the Doppler centroid difference between two scenes of an InSAR becomes larger, the common bandwidth decreases and InSAR performance decreases leading to low coherence (Rosich et al. 2000). Where the Doppler centroid difference is higher than the azimuth bandwidth (or Critical Doppler), there is no common frequency between two InSAR pairs and total decorrelation occurs (Rosich et al. 2000) implying that the pairs are not suitable for interferometric processing.

Temporal decorrelation effects appear where the signature of the target changes over time (Prati et al. 2010; Raucoules et al. 2007; Reigber et al. 2007) and are introduced due to the day difference between the capturing of the two scenes of an interferometric pair (known as master-slave pairs). The day difference between master-slave pairs is known as the temporal baseline. Although, in theory, there is no limit to the length of the temporal baseline, in practice it is restricted to a few weeks or months (although a few years is possible in ideal conditions) depending on the wavelength of the sensor and the characteristics of the land surface (Massonnet & Feigl 1998). This is because changes in surface conditions can cause incoherent phase changes in the returned signal. Two radar images will be coherent with respect to each other if each signal experiences the same interaction with scattering elements on the ground. Incoherence occurs when scatterers within a pixel rearrange randomly leading to different backscatter returns (Massonnet & Feigl 1998). Temporal decorrelation effects include decorrelation due to the position of the scatterer as well as change in scattering characteristics of the target (including a change in the shape, orientation and dielectric constant of the scatterer) (Reigber et al. 2007). Examples of the change in surface properties that cause incoherence include vegetation growth, a change in soil moisture conditions, and erosion from water or wind (Cakir et al. 2005; Massonnet & Feigl 1998).

The evolution of the earth's surface, which tends to increase with increasing temporal baseline, can also lead to interferometric incoherence (Carnec & Delacourt 2000; Perski & Jura 2003) and consequently, temporal decorrelation effects makes dInSAR measurements unfeasible over vegetated areas (Ferretti et al. 2001). In a dynamic commercial agricultural region for instance, the evolution of the land surface is quite pronounced with activities such as tilling, crop growth and harvesting

significantly altering the observed surface. These changes also affect the radar backscatter return which induce an incoherent change in the signal (Blaes & Defourny 2003; Massonnet & Feigl 1998). In these areas, coherence will decrease with increasing temporal baseline. Temporal decorrelation effects can also occur due to changes over short time periods. For instance, the random movement of leaves and twigs of vegetation implies that scattering elements are continuously re-arranged inducing an incoherent phase change. Therefore, higher vegetation densities will be prone to decorrelation effects and interferometric coherence will decrease rapidly with time (Grey & Luckman 2001). The sensitivity of interferometric coherence to variations in the height and density of vegetation have been described in several investigations (Cloude & Papathanassiou 1997; Papathanassiou & Cloude 2001).

Although temporal decorrelation effects are particularly limiting depending on the characteristics of the earth surface, these effects can be partially minimised by careful selection of the wavelength of the sensor and the polarisation of the signal. The interaction of the radar signal with vegetation is dependent on the wavelength of the sensor in relation to the mean size of different plant components (leaves, stems, stalks, trunks etc.) (ESA (European Space Agency) 2005). If the radar wavelength is much greater than the plant components, the signal will penetrate through vegetation, thereby increasing the probability of ground surface interaction (ESA (European Space Agency) 2005). Typically, short wavelength (X-band) signals will interact with the top of the canopy and C-band will partially penetrate resulting in multi-scattering from plant components. L-band signals will penetrate the furthest with a larger probability of interaction with the surface (Raucoules et al. 2003a). Consequently, the influence of vegetation and the associated interferometric decorrelation can be overcome by using longer wavelength L-band data (Massonnet & Feigl 1998; Raucoules et al. 2007). In addition to the wavelength of the sensor, polarisation effects have been shown to play an important role in the extraction of data from interferograms and the strong dependence of interferometric coherence on the polarisation used to form the interferogram have been described (Cloude & Papathanassiou 1998; Cloude & Papathanassiou 1997; Papathanassiou & Cloude 2001). The polarisation of the SAR signal and how it can be exploited for interferometric applications is explored in Section 2.3.2.

2.3 ADVANCED DINSAR APPROACHES

The limitations introduced by phase decorrelation and its impact on dInSAR measurement have been exhaustively researched (Section 2.2). For the purpose of minimising the phase noise component and its impacts, several advanced processing techniques have been developed. These techniques rely either on the selection of pixels demonstrating ideal behaviour to focus on for further processing (Berardino et al. 2002; Euillades et al. 2011; Ferretti et al. 2001; Galloway & Hoffman 2007; Mora et al. 2003; Prati et al. 2010), or the techniques are designed to directly enhance interferometric coherence (Cloude & Papathanassiou 1998; Colin et al. 2006; Navarro-Sanchez et al. 2010; Neumann et al. 2007; Papathanassiou & Cloude 2001; Pipia et al. 2009; Reigber et al. 2007; Sagués et al. 2001). The following sections introduce the theory of advanced dInSAR techniques namely the persistent scatterer and Small-baseline interferometry approach (Section 2.3.1), as well as coherence optimisation approaches (Section 2.3.2).

2.3.1 The persistent scatterers and Small-baseline interferometry techniques

Limitations associated with dInSAR measurements are related to temporal and geometric decorrelations and atmospheric heterogeneities (Ferretti et al. 2001; Prati et al. 2010) as described in Section 2.2. Since they require only a short temporal baseline, traditional dInSAR techniques are well established and are known to be successful in measuring single deformation events (like earthquakes and volcanoes) (Berardino et al. 2002; Mora et al. 2003). However, the measurement of slow gradual deformation over time using traditional dInSAR techniques requires long temporal baselines which can become problematic due to temporal decorrelation effects (Section 2.2). In areas where vegetation cover is sparse and bare soil or rock outcrops dominate, interferometric coherence will be preserved for longer periods allowing for the monitoring of slower movements although, in general, temporal decorrelation effects, in addition to geometric decorrelation effects, will limit the ability to extract useful interferometric measurements (Mora et al. 2003). In addition to temporal and geometric decorrelation, different atmospheric and tropospheric conditions between image acquisitions will result in time delays and will produce phase patterns similar to deformation patterns in interferograms, limiting the accuracy of deformation measurements (Mora et al. 2003).

To overcome the problems associated with temporal and geometric decorrelation and atmospheric artefacts, several advanced interferometric processes have been developed (Berardino et al. 2002; Euillades et al. 2011; Ferretti et al. 2001; Mora et al. 2003; Prati et al. 2010). One such technique, known as persistent scatterer interferometry (PSI) has been described as a powerful tool to overcome these effects (Galloway & Hoffman 2007; Prati et al. 2010; Raucoules et al. 2007). In PSI, a large stack of images (10 to 15 (Raucoules et al. 2007) but ideally more than 30 (Mora et al. 2003)) is used to generate differential interferograms with respect to a common master scene (Berardino et al. 2002; Ferretti et al. 2007; Prati et al. 2010). The algorithm searches for pixels that remains coherent over the entire stack of interferograms, even in the presence of large perpendicular baselines (Ferretti et al. 2001; Prati et al. 2010). These coherent pixels, (known as persistent scatterers (PS)) are usually identified by a statistical analysis of their amplitudes over an entire stack of SAR scenes (also known as the amplitude dispersion index), or by selection of pixels that exhibit coherence values above a certain threshold value for the entire interferogram stack (Ferretti et al. 2001; Mora et al. 2003; Prati et al. 2010). A pixel-by-pixel analysis is carried out to isolate the individual phase contributions due to topography, atmosphere, noise, displacement and orbital contributions from the PS (Raucoules et al. 2007).

The phase terms due to temporal, geometrical and atmospheric effects can be isolated due to the different behaviour of these effects over time and space (Prati et al. 2010). For instance, the phase contributions due to a linear component of deformation over time as well as topographic phase contributions due to DEM errors can be estimated by applying a linear model (Mora et al. 2003). Additionally, atmospheric phase contributions exhibit a strong spatial correlation within every interferogram but will be uncorrelated over time (Berardino et al. 2002; Prati et al. 2010). Therefore the atmospheric phase contributions can be estimated and eliminated by spatio-temporal filtering techniques (Mora et al. 2003).

The PSI technique allows for the measurement of very slow deformation (in the order of millimetres per annum) and, by exploiting very high resolution data, can resolve very small scale features such as the motions of individual buildings (Ferretti et al. 2001; Prati et al. 2010; Raucoules et al. 2007). Additionally, the PS technique allows for the extraction on sub-meter DEM accuracy and millimetric terrain motion detection since the atmospheric effects are removed (Ferretti et al. 2001). The advantage

of the PSI technique over traditional dInSAR techniques is that reliable deformation and terrain measurements can be obtained for a selection of coherent targets even in areas where no interferometric fringes are visible on individual interferograms (Ferretti et al. 2001). However, this is achieved at the expense of the pixel density since only those targets that exhibit sufficiently high coherence values are used in the analysis (Berardino et al. 2002). The PSs are stable natural reflectors usually corresponding to man-made structures of rock-outcrops (Ferretti et al. 2001; Raucoules et al. 2007) meaning that in vegetated, non-urban areas the density of PSs may be very low which will limit the ability to extract long term deformation measurements. Additionally, the large number of scenes needed for PS analysis can be limiting in areas where long time-series of SAR scenes are unavailable.

In an effort to increase the number of coherent targets and decrease the number of scenes required for analysis, an alternative technique based on the selection of a multiple small baseline interferograms were developed (Berardino et al. 2002; Euillades et al. 2011). The technique, known as the Small BAseline Subset (SBAS) technique, minimises the geometric decorrelation effects by focussing only on small baseline (SB) interferometric pairs which result in a higher density of coherent pixels when compared to PSI targets (Euillades et al. 2011). The temporal lag between interferograms using the SBAS technique is reduced by allowing multiple master scenes for the generation of interferograms in contrast to the PSI technique which used a common master scene for interferogram generation.

The use of small baseline interferograms ensures that spatially dense deformation maps can be created since spatial decorrelation effects are minimised (Berardino et al. 2002). Additionally, the small baseline datasets ensure that the topographic contribution due to DEM errors are minimised (Berardino et al. 2002; Mora et al. 2003). The technique has also been extended to subsets of small Doppler centroid difference interferometric pairs which ensured a high density of coherent targets even in the presence of high Doppler centroid difference datasets (Euillades et al. 2011). The SBAS technique has also been extended to involve multi-dimensional datasets, implying the inclusion of datasets from all possible platforms (airborne and space-borne) collected with different acquisition parameters (Samsonov & d'Oreye 2012). This leads to an enhanced temporal resolution of InSAR observations (Samsonov & d'Oreye 2012).

The identification of the atmospheric phase contributions for the SBAS technique are achieved in the same way as in the PSI technique (Berardino et al. 2002; Mora et al. 2003). Additionally, the effects of temporal and geometric decorrelation are also minimised in a similar way to PSI by exploiting the different temporal and spatial behaviour of these phase contributions (Mora et al. 2003). However, the advantage of the SBAS techniques over the PSI technique is that higher densities of coherent targets are identified leading to higher density deformation maps (Prati et al. 2010). Additionally, since more than 1 master scene can be used for interferogram generation, fewer scenes are needed with as few as 7 scenes having been found to be sufficient although as with PSI, more scenes would increase the measurement accuracy (Mora et al. 2003; Tomás et al. 2005).

Both the permanent scatterer (PS) technique and the SBAS technique is based on the analysis of scatterers associated with coherent behaviour over a temporal series. Using these techniques it is possible to partially eliminate the influence of atmospheric and DEM errors and to overcome temporal decorrelation effects. However, various limitations associated with these techniques have been described (Simonetto et al. 2005). Specifically, the prerequisite for PS interferometry is a very high density of permanent scatterers (Navarro-Sanchez et al. 2010; Reigber et al. 2007) with at least 3 to 4 PSs per square kilometre needed to guarantee a sufficient spatial sampling to exploit the spatial correlation whilst isolating the atmospheric phase contributions (Raucoules et al. 2007). Unfortunately, a sufficient density of permanent scatterers is frequently not reached over natural areas limiting the viability of the SBAS and PSI techniques in these areas (Galloway & Hoffman 2007; Reigber et al. 2007). Therefore, in rural and agricultural regions, an alternative approach to overcome temporal and geometrical decorrelation effects is needed.

To overcome temporal and geometric decorrelation effects in agricultural regions, advanced dInSAR techniques have focussed on exploiting the polarimetric properties of SAR signals to maximise interferometric coherence as opposed to merely selecting the high coherence targets for further processing (Navarro-Sanchez et al. 2010; Pipia et al. 2009). Polarimetric data has been used in an attempt to increase the number of stable pixels for further advanced interferometric processing (Navarro-Sanchez et al. 2010). These coherence optimisation techniques have been found to be successful in improving the number of pixel candidates over single polarisation data (Navarro-Sanchez

et al. 2010). Section 2.3.2 will investigate the polarimetric techniques and how they can be exploited for the optimisation of interferometric coherence.

2.3.2 Radar polarimetry, polarimetric interferometry and coherence optimisation

Interferometric coherence remains the most limiting factor for successful interferometric measurement since it reduces the accuracy of interpretations (Binghuang & Bing 2007) (Section 2.2). An important source of decorrelation in interferometric signals is the random rearranging of scattering elements as well as changes in surface and volume scattering mechanisms due to variations in the height and density of the vegetation (Cloude & Papathanassiou 1997; Papathanassiou & Cloude 2001). Although persistent scatterers and SBAS techniques try to overcome some of the limitations of low coherence by focussing only on those pixels above a certain coherence threshold (Berardino et al. 2002; Euillades et al. 2011; Ferretti et al. 2001; Galloway & Hoffman 2007; Prati et al. 2010; Raucoules et al. 2007), the main problems associated with temporal and geometric decorrelation still remain an issue in rural areas (Section 2.3.1). Since temporal decorrelation not only has an effect on the interferometric coherence, but also leads to a different polarimetric responses in two SAR images (Cloude & Papathanassiou 1998; Perski & Jura 2003) the introduction of polarimetry into conventional interferometry has been proposed for sophisticated interpretation of interferometric signals (Stebler et al. 2002).

SAR systems are designed to transmit either vertically polarized or horizontally polarized radiation (or sometimes both). Likewise, the antenna can receive either vertical or horizontal polarized waves (or both). The planes of transmitted and received polarisation are designated by the letters H and V for the horizontal and vertical cases respectively. Thus the polarisation of a radar image can be HH, for horizontal transmit, horizontal receive, VV for vertical transmit, vertical receive, HV for horizontal transmit vertical receive, and vice versa (Natural Resources Canada 2012). A sensor with the ability to capture data in fully polarimetric mode captures information in 4 channels corresponding to different polarisation states. These include HH, HV, VH and VV polarisations. The HH and VV polarised channels are also referred to as like-polarized or co-polarized images whilst HV and VH images are also referred to as cross-polarized images (Natural Resources Canada 2012).

The field of SAR polarimetry investigates the radar back scattering behaviour of surfaces using information obtained from the polarimetric channels (Cloude 2010). The radar backscatter in different polarisations is sensitive to the shape, orientation and dielectric properties of the scattering elements (Papathanassiou & Cloude 2001). When a polarized radar pulse is scattered by rough surfaces such as soil or rock (surface scattering), most of the scattered energy that returns to the antenna has the same polarisation as the transmitted pulse (ie. HH or VV). However, when a polarized pulse interacts with vegetation, it will penetrate the vegetation to a certain degree and will have multiple interactions with leaves, twigs, branches, etc, which cause many scattering events. Such volume scattering will cause partial depolarisation of the radar signal and the returned pulse will have a different polarisation than the transmitted signal (NSIDC 2009). Surface scattering mechanisms do not cause significant depolarisation, resulting in a low backscatter response in cross-polarized (HV or VH) channels. Volume scattering on the other hand, as is the case for vegetated areas, causes significant depolarisation of radar signals resulting in a very strong backscatter in cross-polarized channels (HV and VH) and weak returns in like-polarised channels (HH and VV) (NSIDC 2009).

In vegetated areas, the backscatter return in HH or VV polarisations will depend on the nature of the vegetation in the area. Where vertically orientated vegetation types dominate, a vertically polarised signal will interact with the vegetation thereby increasing the backscatter return from vegetation as opposed to the surface (Silva et al. 2012). On the other hand, where vertical crops dominate, horizontally polarised signals will provide an increased ability to interact with the surface (Silva et al. 2012). In bare soil conditions, the backscatter contribution will be similar for both HH and VV polarisations. However, VV polarisation is more suited for surfaces with small scale roughness (in the order of magnitude of the wavelength of the signal) since the Bragg scattering effect provides a higher signal to noise ratio in the VV channel (Natural Resources Canada 2012). On the other hand, HH polarisation is less sensitive to surface roughness effects than VV polarisation (Natural Resources Canada 2012).

The sensitivity of backscatter in different polarisations to the shape, orientation and dielectric properties of the scattering elements allows for the identification and separation of scattering mechanisms by investigating the differences in polarimetric signatures (Papathanassiou et al. 2000b; Papathanassiou & Cloude 2001). Several coherent and incoherent scattering target decomposition

theorems have been developed with the objective to extract information about scattering behaviour from volumes and surfaces (Cloude & Pottier 1996) allowing the description of ground/volume scattering scenarios (Sagués et al. 2001). These target decomposition theorems have also been introduced in interferometry to advance the interpretation of interferometric phase in an effort to minimise temporal decorrelation effects (Cloude & Papathanassiou 1998; Cloude & Papathanassiou 1997; Colin et al. 2006; Navarro-Sanchez et al. 2010; Neumann et al. 2007; Neumann et al. 2008; Papathanassiou & Cloude 1997; Papathanassiou & Cloude 2001; Reigber et al. 2007).

A strong dependency of interferometric coherence to the polarisation of the signal have been described (Papathanassiou & Cloude 2001) depending on the characteristics of the surface observed. Specifically, in the case of pure volume scattering contributions, polarisation has no influence on interferometric coherence (Papathanassiou & Cloude 2001). In contrast, the ground scattering effects are strongly polarisation dependent and even small ground scattering contributions affect interferometric coherence (Papathanassiou & Cloude 2001). Furthermore, the ability to identify and separate scattering mechanisms from polarimetric signatures implies that the combination of interferometric and polarimetric information can be used to infer the interferometric phase of any scattering mechanism and, consequently, the vertical distribution of different scattering mechanisms (Colin et al. 2006; Papathanassiou & Cloude 1997; Papathanassiou & Cloude 2001). The combination of radar polarimetry and radar interferometry is known as polarimetric interferometry (polInSAR) and the mathematical formulation can be obtained in various published works (Boerner & Verdi 1998; Cloude & Pottier 1997; Papathanassiou & Cloude 1997; Papathanassiou & Cloude 2001).

PolInSAR allows for the retrieval of the height of different scattering mechanisms present in a resolution cell, even if one scattering mechanisms dominates over another (Sagués et al. 2001). Consequently, polInSAR also enables the development of coherence optimisation algorithms to improve the quality of interferometric measurements (Cloude & Papathanassiou 1998; Cloude & Papathanassiou 1997; Colin et al. 2006; López-Martinez et al. 2009; Navarro-Sanchez et al. 2010; Neumann et al. 2007; Neumann et al. 2008; Papathanassiou & Cloude 2005; Pipia et al. 2009). This is achieved by identifying the scattering mechanism which leads to the highest possible coherence and, consequently, the scattering mechanism providing best phase estimates (Colin et al. 2006).

The selection of the optimal scattering mechanism is generally achieved using two techniques. The first approach, also referred to as the Multiple Scattering Mechanism (MSM) technique, relies on the identification of the scattering mechanisms that provide the highest possible coherence, as well as those that provide intermediate and low coherence values and their associated phase information (Cloude & Papathanassiou 1998). Since the phase contribution from different scattering mechanism can be obtained using this technique, the information can then be used to determine the height of the various scattering mechanisms and is therefore useful for the extraction of vegetation parameters such as vegetation height (Neumann et al. 2008; Papathanassiou et al. 2000a). Additionally, vegetation extinction coefficients (related to vegetation density) and underlying topography can be determined (Papathanassiou et al. 2000a).

The drawback of the MSM technique for differential applications is that the scattering mechanism that provides the highest possible interferometric coherence can vary between neighbouring pixels and different scattering mechanisms can contribute to the optimal phase (Neumann et al. 2007; Neumann et al. 2008; Pipia et al. 2009; Reigber et al. 2007). In a multi-baseline approach to the MSM optimisation, varying polarisations in different datasets will have to be taken into account (Neumann et al. 2007; Neumann et al. 2008). Since different scattering mechanisms will provide phase measurements at different phase centres, topographic phase will be incorporated depending on the scattering mechanism that provides the best coherence (Navarro-Sanchez et al. 2010). This can introduce phase discontinuities and introduce an element of heterogeneity into interferograms (Binghuang & Bing 2007). Therefore, for differential applications, it is advisable to select the same polarisation state across all scenes since otherwise interferometric and polarimetric information is mixed and reliable interferometric measurements cannot be made (Reigber et al. 2007).

Although coherence optimisation by the MSM method have been successful in optimising interferometric phase (Colin et al. 2006), the effects of phase contributions from different scattering mechanisms has to be overcome. To overcome these effects, an alternative approach to coherence optimisation using an Equal Scattering Mechanisms (ESM) technique has been developed (Colin et al. 2006). The ESM optimisation process involves the simultaneous search for the optimised coherence and the corresponding scattering mechanism (Neumann et al. 2007) with the constraint that equal scattering mechanisms are selected (Neumann et al. 2007; Neumann et al. 2008; Reigber et al. 2007).

The ESM approach ensures the selection of equal polarimetric signatures representing the dominant scattering mechanism (Neumann et al. 2007; Neumann et al. 2008; Reigber et al. 2007). By identifying the most correlated scattering mechanism, the phase error for this scattering mechanism will be minimal although lower coherence magnitudes will be obtained when compared to the MSM technique. However, the corresponding phase measurements are regarded as more accurate (Neumann et al. 2008).

The drawback of the ESM approach is that it assumes that the polarimetric behaviour across datasets do not change (Neumann et al. 2007) which implies that small temporal and perpendicular baseline datasets are needed (Neumann et al. 2008). This is considered to be the drawback of the ESM approach since, in cases where a large amount of temporal decorrelation exists or where large changes between viewing angles between interferometric pairs exist, the scattering behaviour of surfaces can change significantly. This implies that different scattering mechanisms will provide the optimal coherence and the ESM approach is therefore considered to be ineffective for long temporal and perpendicular baselines (Binghuang & Bing 2007; Neumann et al. 2008). In these cases, the MSM technique is preferred.

Ultimately, the selection of the optimal coherence optimisation technique depends on the similarity of the polarimetric behaviour over time. For the MSM method, the heterogeneity introduced by selecting different optimal scattering mechanisms means that phase noise cannot be entirely eliminated. On the other hand, the ESM method is constrained to areas that do not undergo significant changes in the polarimetric behaviour over time and, additionally, constrained to datasets with small perpendicular baselines. In the case of strong temporal characteristics and perpendicular baselines, the MSM technique should be used (Neumann et al. 2007).

2.4 SOME SPECIFIC EXAMPLES OF RADAR INTERFEROMETRY FOR THE STUDY OF SURFACE DEFORMATIONS

2.4.1 Radar interferometry applied to the monitoring of surface subsidence

The measuring of surface deformations associated with mining using traditional ground-based techniques is expensive and consequently the common strategy of the coal mining industry is to measure as little as possible (Perski & Jura 2003). As a result measurements are done only at limited

locations with a low frequency. In most cases this means that many of the deformation phenomena are not well recognised and poorly understood. The problems associated with ground-based techniques for measuring surface subsidence have also been recognised (Raucoules et al. 2007). These include the difficulties and high cost associated with frequent re-visitations, variations in the precision of measurements and difficulties in accessing monitoring sites in isolated areas. To overcome these limitations, differential radar interferometry has been proposed for measuring surface subsidence.

Various authors have studied surface subsidence using radar interferometry techniques (Anderson 2007; Carnec & Delacourt 2000; Chang et al. 2004; Herrera et al. 2007; Massonnet & Feigl 1998; Perski & Jura 2003; Raucoules et al. 2003b; Smith 2002; Tomás et al. 2005). These studies found that the causes of subsidence vary and include: 1) subsidence as a result of mining (Carnec & Delacourt 2000; Perski & Jura 2003; Raucoules et al. 2003b); 2) subsidence as a result of over-exploitation of groundwater reserves (Herrera et al. 2007; Massonnet & Feigl 1998; Tomás et al. 2005) ; 3) subsidence caused by the collapse of underground cavities (Herrera et al. 2007); and 4) subsidence as a consequence of natural geological processes (Anderson 2007). The advantages of using radar interferometry for measuring and monitoring surface subsidence include the fact that it is more cost effective than monitoring extensive areas by traditional ground-based approaches (Anderson 2007; Herrera et al. 2007). It also allows for the extraction of information on the spatial and temporal evolution of subsiding areas at more frequent intervals than traditional techniques (Anderson 2007; Herrera et al. 2007; Massonnet & Feigl 1998; Tomás et al. 2005). Various authors also remark that radar interferometry will provide a synoptic view of the deformation pattern as opposed to the discrete point locations monitored by traditional techniques (Carnec & Delacourt 2000; Raucoules et al. 2003b). Most of the authors describe the ability to measure subsidence at millimetre- to centimetre-scale accuracy in good agreement with ground-based measurements.

Successful studies on the use of dInSAR in surface subsidence measurements include:

- The monitoring and measuring of subsidence as a result of ground water extraction in California. Subsidence of up to 90 mm during a two-year period was reported. Based on the interferometric measurements, ground water loss was estimated and found to be in good agreement with the water loss based on their pump-log data (Massonnet & Feigl 1998);

- The interferometric measurement of subsidence of up to 42 mm over a 35-day period in a coal mining area in France has been reported (Massonnet & Feigl 1998). This subsidence was recorded despite efforts to prevent subsidence by using waste rock to compensate for the loss of volume behind the extraction front. The ability to measure such deformations opens the prospect for industrial and environmental applications with both economic and legal consequences (Massonnet & Feigl 1998);
- Local subsidence associated with the coal mining activities in France has been investigated which revealed a migration of the subsidence halo associated with the working face of the mine. Deformation was also observed in the presence of abandoned underground cavities. Comparison of the results with data obtained by field levelling revealed that the amount of subsidence measured by both techniques was similar (Carnec & Delacourt 2000);
- Deformation associated with a coal-mining area in Poland using 50 ERS SAR scenes in 2-pass, 3-pass and 4-pass approaches was investigated. Detailed analysis of the data demonstrated that both qualitative (shape and extent of subsided area) and quantitative (rate of subsidence) information could be retrieved. The total deformation was measured for both urbanised and rural areas where damage to buildings, infrastructure and hydrological systems was reported (Perski & Jura 2003);
- Advanced dInSAR techniques (PSI techniques) were applied to measure subsidence in a metal mining area in south-eastern Spain. Here the collapse of abandoned underground galleries caused subsidence of an industrial area. The derived deformation maps enabled the detection of several deformation processes over different locations. Comparing the results with a map of underground mining galleries revealed a relationship between the presence of galleries and surface subsidence (Herrera et al. 2007);
- The PS technique was also applied to study subsidence related to aquifer over-exploitation in Spain. A total of 25 ERS-1 and -2 scenes were used to derive a subsidence map indicating settlement of up to 8 cm. Comparison of dInSAR results with groundtruth data indicated a relationship between deformation and ground water fluctuations and borehole extensiometric settlement (Tomás et al. 2005);
- DInSAR was used to detect and monitor ground deformation at a salt mine in France using a 2-pass interferometry technique. An adaptive filtering technique was applied to improve the level

of coherence. dInSAR measurements showed a good comparison with available levelling lines providing ground-truth data for accuracy assessment purposes (Raucoules et al. 2003b).

- Both dInSAR and PS interferometry techniques were employed for the monitoring of mining-induced subsidence in the Nord/Pas-de-Calais Coal basin in Northern France. The results were compared with field-based levelling results and the results indicated that the observed subsidence using the different techniques was equal. Additionally, it was possible to measure small displacements of the same magnitude than those measured by levelling techniques although larger areas could be monitored on a regular basis (Guéguen et al. 2009).
- The results of dInSAR experiments in 6 mining areas in France have been reported (Simonetto et al. 2005). This includes subsidence associated with coal mining, salt mining and iron mining regions. Their results revealed that surface subsidence could be detected in good agreement with levelling results. Additionally, uplift associated with was also reported. PS interferometry results over an iron mining region further revealed that precursory surface deformation prior to sudden collapse of underground cavities could be detected, confirming that dInSAR techniques can be used for long term monitoring of areas susceptible to deformation risk (Simonetto et al. 2005).

Although polInSAR techniques are traditionally applied for the inversion of vegetation parameters (Cloude 2010; Cloude & Papathanassiou 1998; Cloude & Papathanassiou 1997; Öttl et al. 2000; Papathanassiou et al. 2000a; Papathanassiou et al. 2000b; Stebler et al. 2002) the ability to extract phase information for different scattering mechanisms prompted the consideration of the technique differential interferometric applications (Navarro-Sanchez et al. 2010; Pipia et al. 2009). The potential of polarimetric coherence optimisation for dInSAR measurements have been tested on simulated and real zero-baseline X-band polarimetric acquisitions (Pipia et al. 2009). The results suggest that, for simulated data, the MSM and ESM techniques converge to the same optimal coherence although the highest coherence values were obtained with the MSM algorithm using real data. This was due to the fact that a change in scattering behaviour over time resulted in the failure of the condition for application of the ESM technique. In terms of the differential movement, the results revealed that no enhancement in differential phase information was obtained using either ESM or MSM results. However, it was demonstrated that the phase standard deviation was higher after MSM optimisation compared to EMS optimisation highlighting the selection of diverse phase centres for different

scattering mechanisms. This corroborated the notion that same scattering mechanism is needed for differential applications (Pipia et al. 2009).

As mentioned in Section 2.3.1, the PS and SBAS techniques need a large number of high coherence, stable pixels to be successful. Therefore, the use of polInSAR coherence optimisation techniques was considered for its ability to increase the number of suitable pixel candidates (Navarro-Sanchez et al. 2010). The technique was tested on dual-polarisation TerraSAR-X data. The coherence optimisation approach focussed on the provision of a single polarimetric channel providing optimal coherence for a stack of interferograms, thereby eliminating the effect of diverse phase centres. The results demonstrated that a significant increase in the number of pixel candidates for PS and SBAS processing could be achieved by exploiting polarimetric data (Navarro-Sanchez et al. 2010).

These studies and numerous others highlight the ability of radar interferometry techniques to measure and monitor subsidence over large areas. DInSAR techniques are regarded by most as being complementary to traditional measurement techniques. However, there are various limitations of dInSAR approaches to monitor subsidence. The major limitations described in the literature include:

- Short temporal baselines: Since subsidence is generally a slow process, very short temporal baselines may prohibit the detection of subsidence using traditional differential interferometry approaches with long temporal baseline interferograms being needed to detect slow movements of say 10 to 20 cm per annum (Perski & Jura 2003). However, advanced dInSAR techniques can be used to overcome these limitations (Section 2.3.1);
- Coherence limitations: Successful interferogram generation is dependent on seasonal and weather conditions before and during image acquisition (Carnec & Delacourt 2000; Perski & Jura 2003). Low coherence can be avoided by selecting data with a short temporal baseline (Carnec & Delacourt 2000; Perski & Jura 2003). However, the longer temporal baseline acquisitions to measure slow movements associated with subsidence will increase coherence losses as a result of surface cover changes (Carnec & Delacourt 2000; Perski & Jura 2003). Consequently careful SAR data selection considering detailed meteorological information will enable the maximisation of interferometric coherence (Perski & Jura 2003). Furthermore, advanced dInSAR approaches (described in Section 2.3) can be employed to overcome coherence limitations;

- Ionospheric and troposperic fluctuations: These effects can result in interferometric artefacts that may be misinterpreted as deformations. These atmospheric artefacts have a spatial correlation that is very similar to that of subsidence basins and care should be taken with interferogram interpretation (Raucoules et al. 2007). Although comparison between several independent interferograms will usually be sufficient for separating atmospheric artefacts from deformation information (Raucoules et al. 2007), advanced dInSAR approaches including the SBAS and PS techniques (Section 2.3.1) should be considered to eliminate atmospheric phase from interferograms.
- Land surface conditions: The use of dInSAR for the measurement of mining-induced subsidence (using C-band data) was found to be unsuccessful in non-urban areas due to vegetation growth and humidity variations (Simonetto et al. 2005). However, the application of longer wavelength L-band data revealed that the longer wavelength data was less sensitive to temporal variation due to surface changes (Simonetto et al. 2005).

Some factors not directly associated with the dInSAR technique will also have to be taken into account. For instance, the geology of the study area will influence the expression of surface subsidence (Carnec & Delacourt 2000). More competent lithologies will be less susceptible to deformation and more prone to collapse than gradual subsidence, while less competent lithologies will be more susceptible to gradual movements. In the case of collapsing structures there is a chance that the event could occur outside the dates of interferometric pair acquisition making measurement by dInSAR approaches impossible (Carnec & Delacourt 2000). However, the roof strata in the mines of the Witbank coal fields are generally weak and more prone to gradual movements (Bell et al. 2001), which would imply that the area will provide an ideal test case for interferometric subsidence measurements.

2.4.2 Radar Interferometry in South Africa

The use of radar interferometry to measure surface deformation in South Africa has been investigated by various authors (Doyle et al. 1997; Doyle et al. 1999; Doyle et al. 2001b; Doyle et al. 2001a). Mining-induced seismic deformation in Welkom after an M 4.5 earthquake took place in April 1999. A combination of ERS SAR images captured both before and after the event was used to quantify the deformation resulting from the earthquake. Despite expected coherence limitations associated with

active agricultural lands, patterns associated with crustal deformation were observed coinciding with surface displacement of ~9.5cm at the centre of the deformation feature. The time-span between the capturing of the images (11 months) and the fact that the area coincides with areas of general surface subsidence due to mining meant that surface subsidence could not be ruled out as a contributing factor in the deformation process. However, the results indicated that the orientation of the elliptical fringe patterns coincided with the major geological structures in the study area. Significantly, the deformation patterns associated with the seismic events of M 4.5 could be mapped, while the research output could be used as input into rockburst characterization models (Doyle et al. 2001a).

The detection and measurement of crustal deformation associated with the filling of the Katse Reservoir in Lesotho using dInSAR techniques were also investigated (Doyle et al. 1997; Doyle et al. 1999; Doyle et al. 2001b). The loading effects of large reservoirs may be sufficient to cause vertical buckling of the surface as well as induce brittle failure and remobilization of existing fracture zones, sometimes triggering earthquakes (Doyle et al. 1997). SAR data before and after the filling of the reservoir were obtained for the purpose of mapping the deformation caused by a known volume of water. The results could be used to draw conclusions relating to geophysical factors, including flexural thickness (Doyle et al. 1997).

Despite decorrelation effects associated with seasonal variation of vegetation cover and terrain attributes, good coherence and fringe patterns could be produced using imagery with short temporal baselines. However, the high topographic relief meant that unwrapping of the interferograms, and consequently DEM generation, were impossible and that direct subtraction of the topographic phase for the purpose of differential interferometry was not possible (Doyle et al. 1999). To overcome these limitations, a small baseline (21 m) interferometric pair was obtained to produce a topographic fringe rate that was sufficiently low for differential fringes to be visible without the need for topographic phase removal (Doyle et al. 2001b). The resulting interferogram indicated no evidence of deformation fringes. It was concluded that the actual deformation associated with the Katse Reservoir impoundment was not sufficiently large to be detected using dInSAR techniques. Additionally, the rigidity of the crust were believed to cause deformation effects from crustal loading to be distributed over an area exceeding the extent of ERS image boundaries (Doyle et al. 2001b).

2.5 FINAL REMARKS

The ability of differential interferometry techniques to detect and measure surface deformations is well established, with a large number of researchers describing successful applications. Advanced dInSAR approaches provide a means of extracting millimetre-scale changes on the earth surface, making it a powerful tool for detecting and monitoring potential deformation hazards. Even though traditional ground-based techniques for measuring deformation are well established, dInSAR approaches have numerous advantages over traditional geodetic techniques. This includes acquiring a synoptic view of deformation signatures over large and/or remote areas faster and more economically than would be possible using traditional techniques. DInSAR monitoring of deformations will also relieve the need to send personnel into areas considered too remote or unsafe to enter.

The historical availability of SAR images (since 1992 in the case of ERS) means that these images are useful for measuring historical deformations events. This makes dInSAR applications critical, since traditional ground-based monitoring programmes are frequently implemented only after a deformation event. Using these archives and advanced approaches such as PSI and SBAS techniques can be applied. This also implies not only that past deformation phenomena can be studied, but precursors to critical events can be identified.

The most limiting factor of the use of dInSAR is linked to the loss of coherence over time, the influence of atmospheric artefacts, the presence of uncompensated topography and to sensor limitations (such as orbital cycle and pixel size) (Raucoules et al. 2007). However, advanced dInSAR approaches including PSI, SBAS and polInSAR have potential to alleviate many of the problems.

The results obtained by various authors demonstrate the need to include dInSAR techniques systematically as an operational component in monitoring surface deformation irrespective of the cause of the deformation. Since dInSAR is a powerful and cost-effective tool for monitoring potentially deforming surfaces, dInSAR is expected to be highly complementary to traditional techniques. The monitoring of subsidence as a result of mining using dInSAR techniques will enable the understanding of the evolution of subsidence basins and the consequent long-term impacts on the environment. Understanding the geological processes is the key to managing subsidence (Anderson 2007). Importantly, it is necessary to know where subsidence is occurring, how the ground is moving and how

fast subsidence is progressing. With this knowledge, informed decisions on current and future infrastructure can be made. Radar interferometry is believed to provide a means to monitor subsidence in mining areas at a fraction of the cost of traditional ground-based techniques. Additionally, the synoptic view provided by SAR data will enable the selection of sites for ground-based monitoring networks.

3 SAR AND ANCILLARY DATA AND IMAGE PROCESSING

To explore the operational limitations to the long-term monitoring of mining-induced surface deformation and the advantages provided by advanced interferometry techniques, several sources of SAR data were exploited. These include C-band (ERS-2 and RADARSAT-2), L-band (ALOS PALSAR) and X-band (TerraSAR-X) data. The data was acquired with different temporal and geometric conditions implying that the effects of different sources of decorrelation could be investigated. Additionally, the acquisition of the data at different polarisation states implied that polarimetric parameters could also be considered.

The agricultural nature of the area of interest implied that the existence of a high density of coherent targets over time was unlikely. Consequently, PS and SBAS techniques were not tested in this investigation. However, the availability of fully polarimetric data implied that polInSAR techniques to overcome limitations associated with dInSAR techniques could be investigated. A description of the image and ancillary data used in this investigation is provided in Section 3.1. The dInSAR and polInSAR processing chain is provided in Section 3.2.

3.1 IMAGERY AND ANCILLARY DATA REQUIRED

To test dInSAR and polInSAR techniques for their ability to monitor surface deformation in the area of interest, several sources of SAR scenes were obtained. The scenes were captured at a variety of wavelengths (X-band, C-band and L-band) as well as polarisation states (single polarisation, dual polarisation and fully polarimetric). Sections 3.1.1 to 3.1.4 introduce the SAR scenes acquired and a description of ancillary sources of information used in this investigation is provided in Section 3.1.5.

3.1.1 ERS-1 and ERS-2 data available for traditional dInSAR analysis

The ERS-2 satellites were launched on 21 April 1995. ERS-2 is in a sun-synchronous orbit at an altitude of 800 km. The Synthetic Aperture Radar (SAR) instrument operates at C-band with VV polarisation. A typical image covers an area of 100 x 100 km. A search for historical ERS-1 and ERS-2 data was performed by using Eoli-sa V 6.0.1 software available from the European Space Agency. The search for images covering the Witbank Coalfields revealed that a large number of historical ERS-2 images were available for interferometric processing. The footprint of available ERS-2 scenes is presented in Figure 11. The dates of image acquisition are presented in Table 1. The scenes were obtained from the European Space Agency through their Cat-1 support initiative. The backscatter intensity of the ERS-2 scene captured on 1995/12/02 is presented in Figure 12.

Table 1: Dates of ERS-2 image capture.

Date of image capture
1995/12/02
1996/03/15
1996/12/21
1997/01/25
2000/02/19
2002/09/21
2002/10/26
2003/04/19
2003/05/24
2008/04/12
2008/05/17
2008/06/21
2008/07/26
2008/08/30

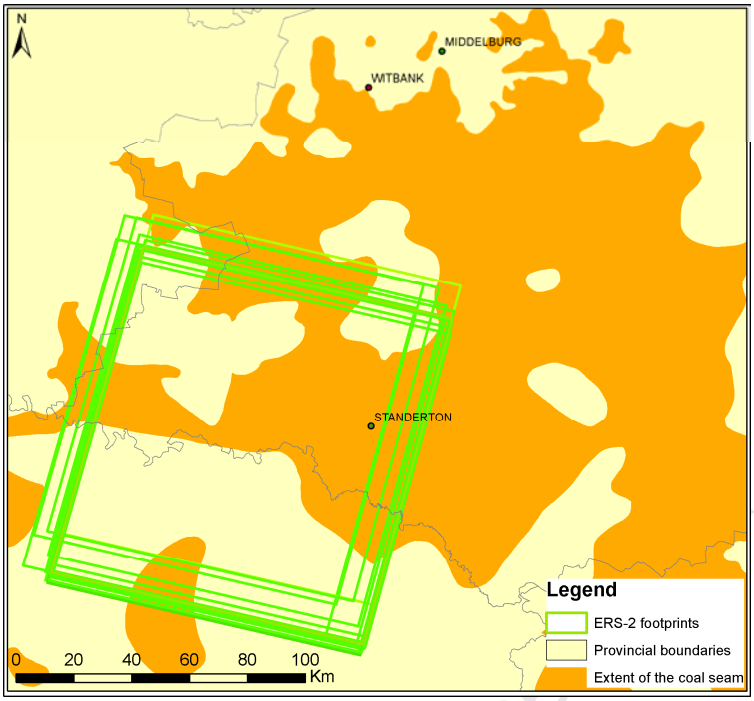

Figure 11: Footprints of available ERS-2 data.

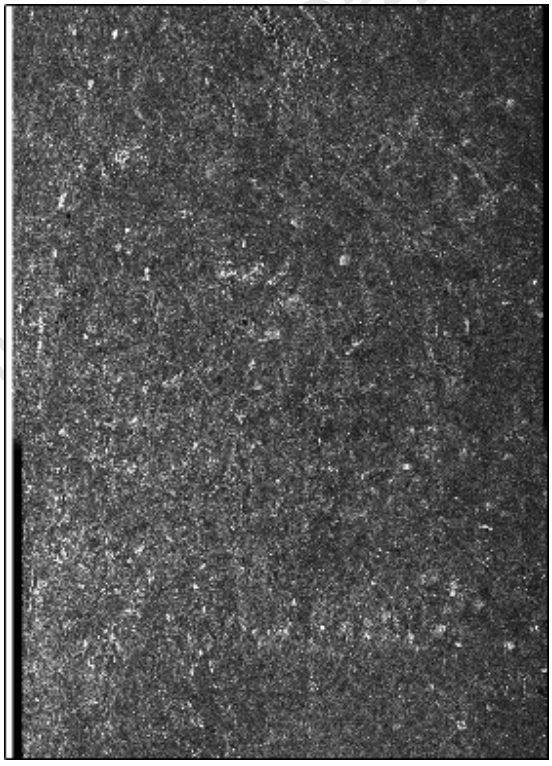

Figure 12: The backscatter amplitude of the ERS scene captured on 1995/12/02.

3.1.2 ALOS PALSAR data available for traditional dInSAR and polInSAR analysis

The ALOS satellite was launched on 24 January 2006 in sun-synchronous orbit at an altitude of 691.65 km. The phased array type L-band synthetic aperture radar (PALSAR) sensor, operating in polarimetric mode offers a 30 m resolution on a 30 km swath and can offer a full polarisation scheme. When operating in fine resolution mode, it offers 10 m spatial resolution with a swath width of 70 km whilst operating in single (HH or VV) or dual polarisation (HH/HV or VV/VH).

To test the ability of traditional dInSAR and polInSAR approaches to measure surface deformation in the area, several scenes captured in different polarisation modes were obtained from the European Space Agency through their Cat-1 support initiative. The footprints of available scenes are displayed in and the polarisation states and dates of image capture are summarised in Table 2. The backscatter intensity of the ALPOS PALSAR scene captured on 2007/08/16 is presented in Figure 14.

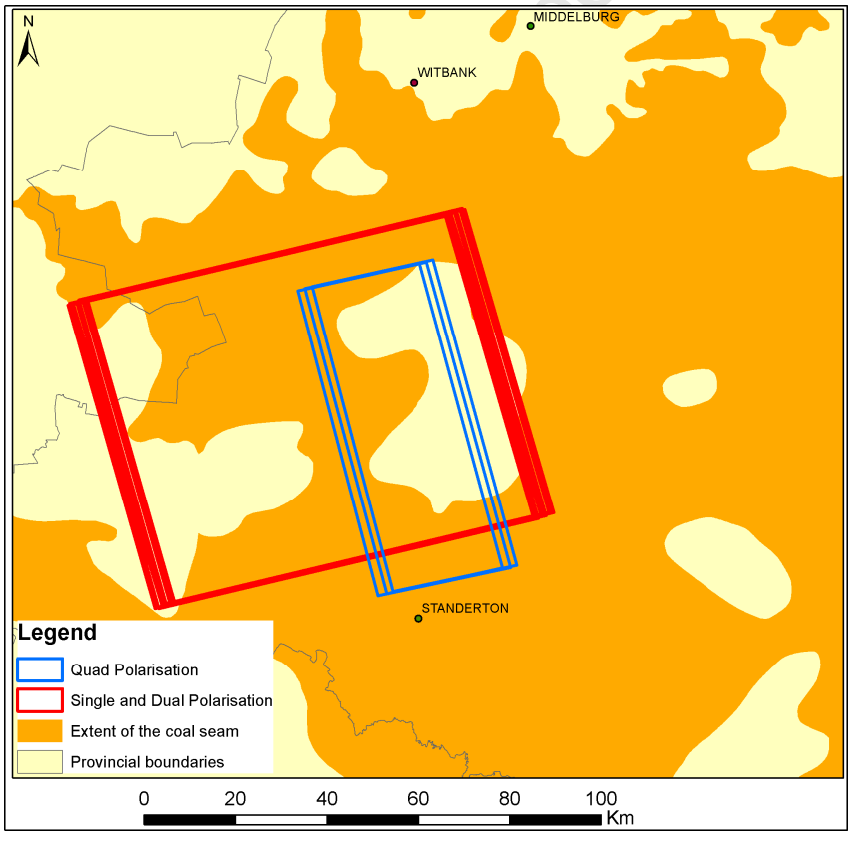

Figure 13: Footprints of available PALSAR datasets captured in single, dual and full polarisation modes.

Table 2: PALSAR scene availability.

Date of image capture	Polarisation
2007/08/16	HH/HV
2008/02/16	HH
2008/05/18	HH/HV
2008/07/03	HH/HV
2008/08/18	HH/HV
2008/10/03	HH/HV
2008/10/27	HH/HV/VH/VV
2009/01/03	HH
2009/02/18	HH
2009/04/29	HH/HV/VH/VV
2009/10/30	HH/HV/VH/VV
2010/01/06	HH
2010/02/21	HH
2010/04/08	HH
2010/08/24	HH/HV
2010/10/09	HH/HV

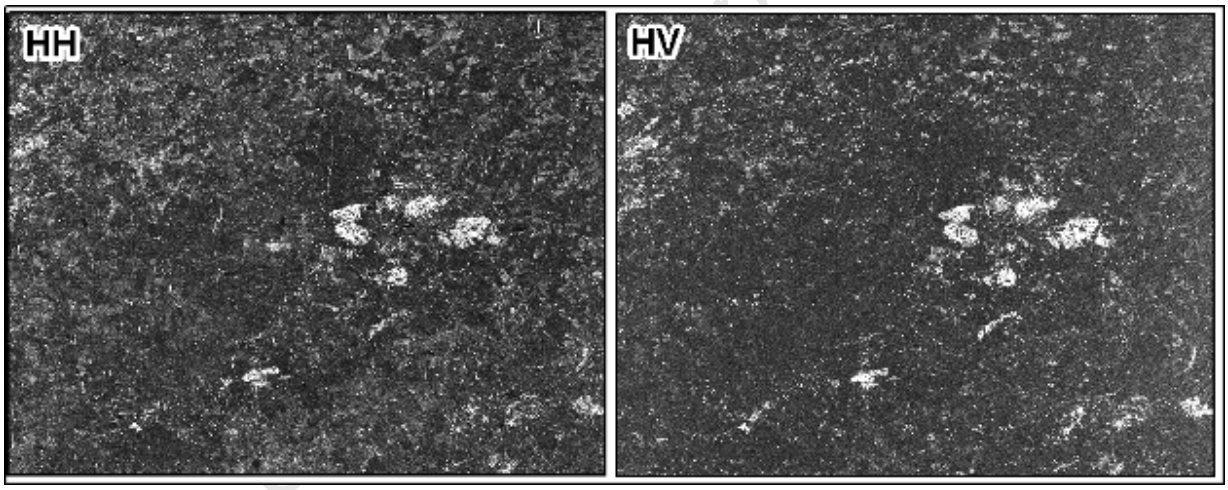

Figure 14: The backscatter amplitude for ALOS PALSAR scene captured on 2007/08/16 in HH and HV polarisation respectively.

3.1.3 RADARSAT-2 data available for dInSAR and polInSAR analysis

The RADARSAT-2 satellite, hosted by the Canadian Space Agency was launched on 14 December 2007. The satellite hosts a synthetic aperture radar sensor with the ability to capture data in various polarisation modes. Specifically, fully polarimetric data can be acquired. To test polInSAR for its ability to increase polarimetric coherence for optimised interferogram generation, 12 RADARSAT-2 images were commissioned to be captured in the Witbank Coalfields. The data, captured in fine beam

quadrature polarisation, covers an area of 25 X 25 Km at a resolution of 5.2 m in range direction and 7.6 m in azimuth direction. Images were captured at 24-day intervals with exception of a period between 2011/05/02 and 2011/08/06 during which no scenes were captured due to conflicting data orders. The availability of data captured at regular intervals throughout 2011 will enable the monitoring of the evolution of subsiding features over time.

Due to the high cost and small footprint of fully polarimetric RADARSAT-2 data, the scenes were limited to cover only an area of active longwall mining where subsidence was known to take place. The footprint of the scenes in relation to the area of interest is displayed in Figure 15 and the dates of image capture are summarised in Table 3. The backscatter amplitude images for HH, HV, VH and VV polarisation channels for the scene captured on 2011/01/26 are presented in Figure 16.

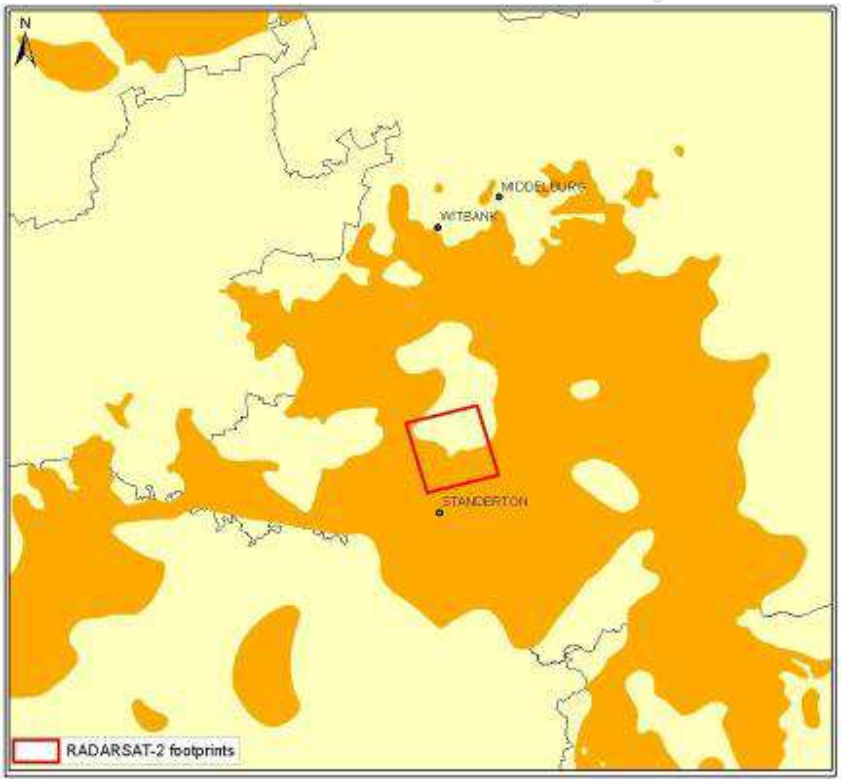

Figure 15: Footprint of the RADRSASAT-2 scenes in relation to the area of interest.

Table 3: RADARSAT-2 image availability.

Date of image capture
2011/01/26
2011/02/19
2011/03/15
2011/04/08
2011/05/02
2011/08/06
2011/08/30
2011/09/23
2011/10/17
2011/11/10
2011/12/04
2011/12/28

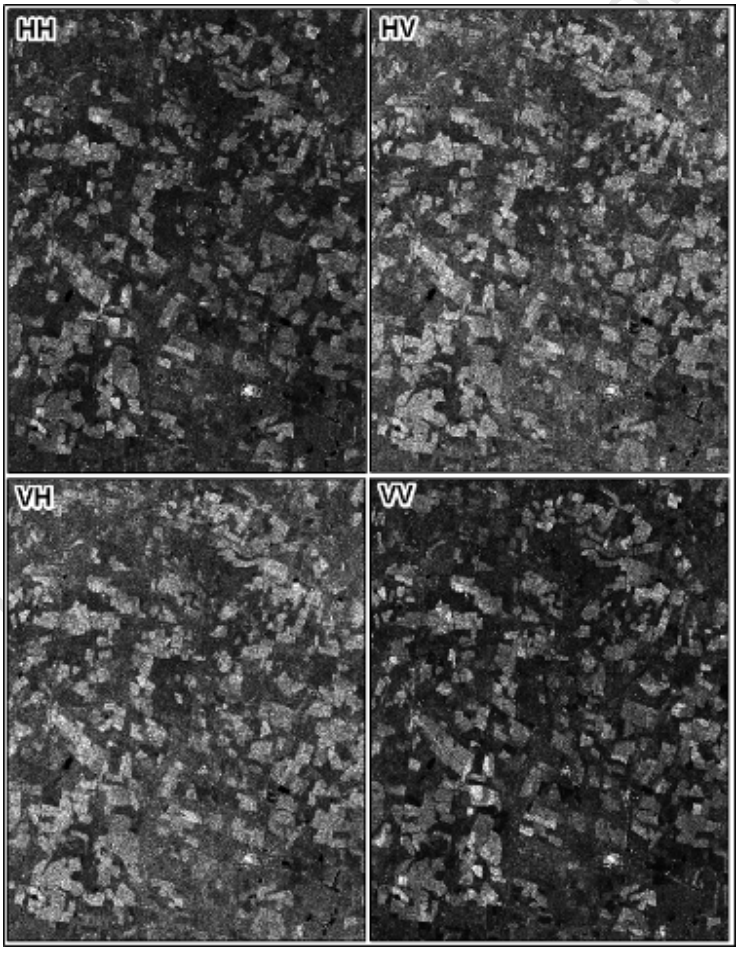

Figure 16: The backscatter amplitude for RADARSAT-2 scene captured on 2012/01/26 in HH, HV, VH and VV polarisations respectively.

3.1.4 TerraSAR-X data available for dInSAR analysis

The German TerraSAR-X satellite was launched on 15 June 2007. The phased array X-band SAR antenna acquires high resolution imagery and operates at an altitude of 514 km. Although the TerraSAR-X sensor was designed to capture data at various polarisation modes including single polarisation, dual polarisation and fully polarimetric modes, at the time of data acquisition, the fully polarimetric mode was operated on an experimental basis and only dual- or single polarisation data could be acquired for the Witbank Coalfields. 21 TerraSAR-X scenes were made available through the German Aerospace Centre (DLR) Science Service System.

The data was provided in StripMap mode which provides data at ~ 3 m resolution. To determine the optimal sensor configuration for interferometric analysis, scenes in various polarisation states were acquired. These include 4 scenes captured at VV polarisation, 10 scenes in HH polarisation and 7 scenes in dual polarisation (HH/HV). The scene parameter including date of image acquisition and polarisation mode is summarised in Table 4. The backscatter amplitude images for HH and VV polarisation channels for the scene captured on 2009/07/16 is presented in Figure 18.

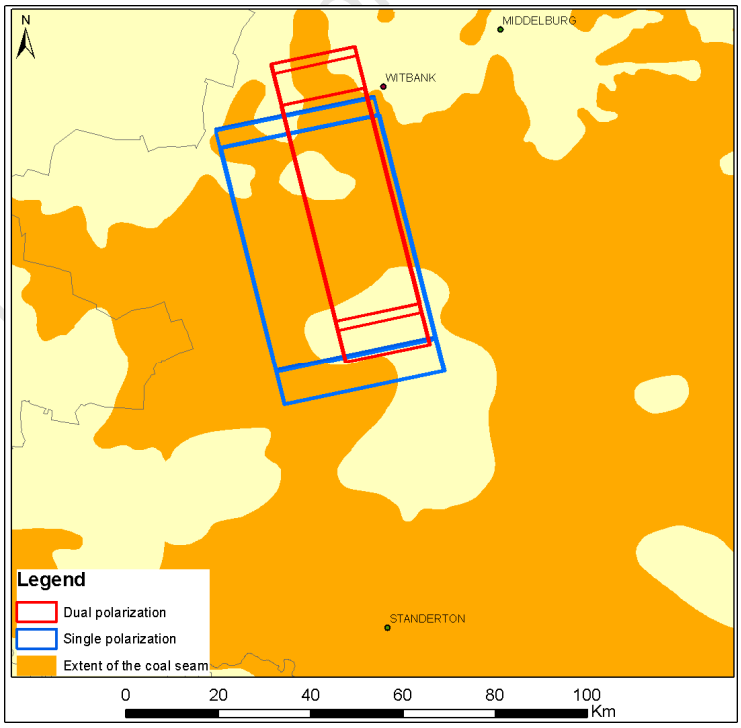

Figure 17: TerraSAR-X footprints in the area of interest.

Table 4: TerraSAR-X image description.

Date of image capture	Polarisation
2008/01/13	VV
2008/02/04	VV
2008/03/19	VV
2008/05/02	VV
2008/11/16	HH
2008/12/19	HH
2009/01/10	HH
2009/02/01	HH
2009/02/23	HH
2009/03/17	HH
2009/04/08	HH
2009/04/30	HH
2009/05/22	HH
2009/06/24	HH
2009/07/16	HH/VV
2009/08/29	HH/VV
2009/09/20	HH/VV
2009/10/23	HH/VV
2009/11/25	HH/VV
2009/12/28	HH/VV
2010/07/14	HH/VV

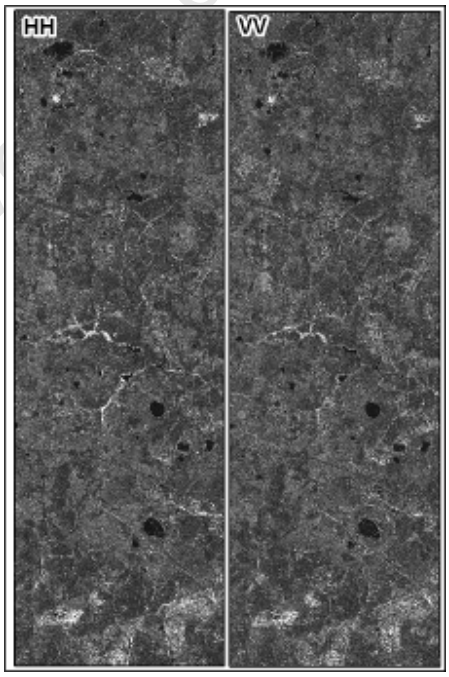

Figure 18: The backscatter amplitude for the TerraSAR-X dual polarisation scene captured on 2009/07/16 in HH and VV polarisations respectively.

3.1.5 Ancillary data required

For the removal of topographic phase contributions from interferograms, an external source of elevation data was used. The digital elevation model used in this investigation was the 90 m SRTM digital elevation model, a joint National Geospatial-Intelligence Agency (NGA) and National Aeronautics and Space Administration (NASA) project. In addition to the satellite data, precise orbital state vectors for ERS-2 and RADARSAT-2 data were obtained. For ERS-2 data, the PRARE Precise Orbit Product was provided by the European Space Agency. The RADARSAT-2 orbital information was provided by MDA corporation. The orbital state vectors were updated during the stage where data was imported and the precise orbital information was consequently available during further processing.

Since the characteristics of the land surface and how it evolves over time has a significant influence on the ability to extract reliable deformation measurements from interferometric SAR data, the dynamic agricultural nature of the area (Section 1.5) was expected to limit successful deformation measurements over long timeframes. To get an estimation of land surface conditions and how it evolves over time, the MODIS Time Series Viewer (available at http://afis.meraka.org.za/wamis/time-series-viewer) were used to extract information on the phenology of vegetation in the study area. The viewer, developed by South Africa's CSIR Meraka Institute, provides access to enhanced vegetation index (EVI) data derived from a long time-series of MODIS data. The EVI is responsive to canopy structural variations including leaf area index (one half of the total green leaf area per unit ground surface), canopy type, plant physiognomy and canopy architecture. Using the EVI, the phenology of vegetation can be derived including information on the start of the growing season and the end of the growing season.

Information on the phenology of the vegetation in the area was extracted for RADARSAT-2 (Figure 19), ERS-2 (Figure 20), PALSAR (Figure 21) and TerraSAR-X data (Figure 22). The data reveals that the first 3 RADARSAT-2 scenes captured for the study area (2011/01/26 to 2011/03/15) were captured during a time period where EVI values were higher than average for the 12 month period between 2010/11/01 and 2011/11/01. This suggests that a high leaf area index (LAI) was experienced during this period and coincides with the peak of the growing season. Scenes captured after 2011/03/15 experienced EVI values lower than the average suggesting a low leaf area index and low vegetation density. Although EVI data for the first 4 ERS-2 scenes were unavailable, the remainder of the ERS-2 scenes were captured either before, or after the peak of the growing season (Figure 20).

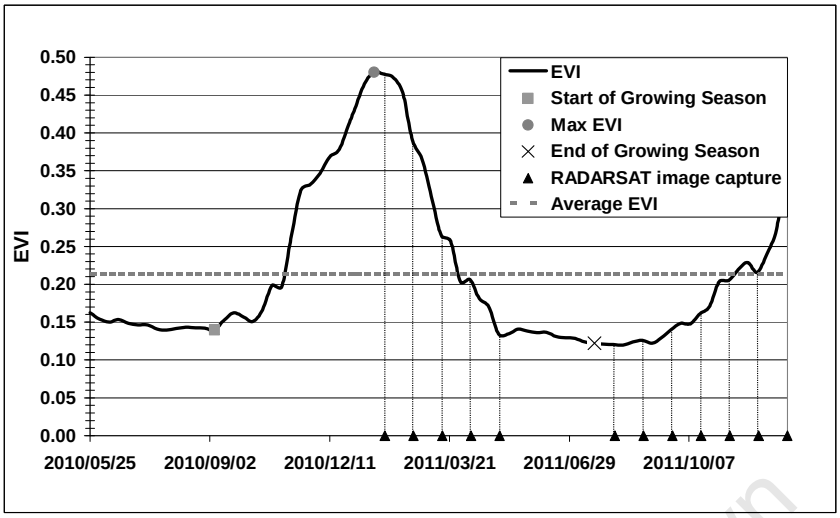

Figure 19: The phenology of the vegetation at the time of RADARSAT-2 image capture with the start and end of the growing season indicated (adapted from http://afis.meraka.org.za/wamis/time-series-viewer). The average EVI was calculated for a period between 2010/05/25 and 2011/12/27. The dates of RADARSAT-2 image acquisition are also indicated.

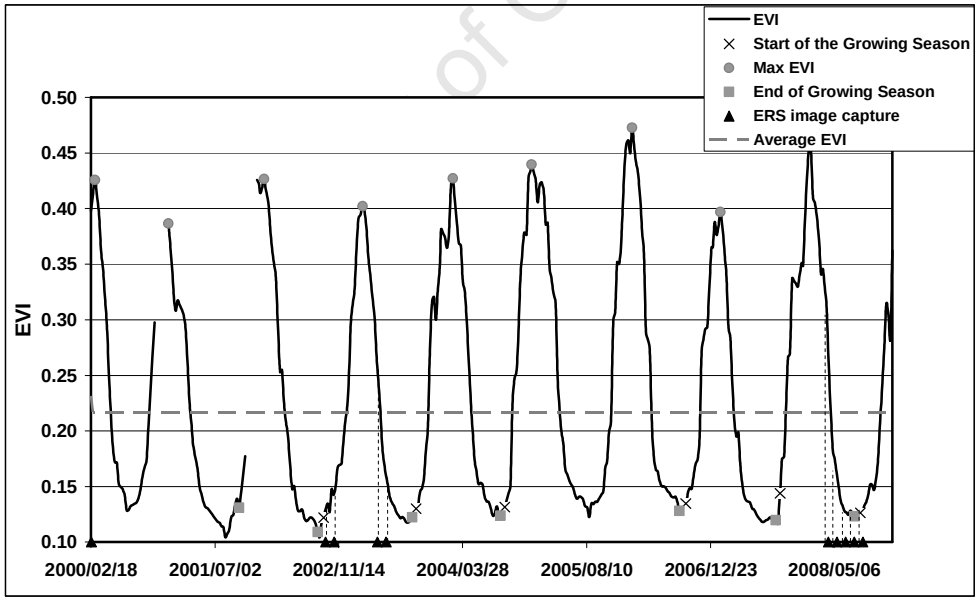

Figure 20: The phenology of the vegetation at the time of ERS-2 image capture with the start and end of the growing season indicated (adapted from http://afis.meraka.org.za/wamis/time-series-viewer). The average EVI was calculated for a period between 2000/02/18 and 2008/12/26. The dates of ERS-2 image acquisition are also indicated.

The PALSAR scenes were captured over 4 phenological cycles with 9 scenes being captured at a time when the vegetation density was low, and 7 scenes captured during high EVI periods (Figure 21). It is observed that the scenes captured in single polarisation mode (FBS) were captured during or close to the peaks of the growing seasons at a time when the vegetation density was high. On the other hand, the scenes captured in dual polarisation mode (FBD) were captured during periods where the vegetation densities were low.

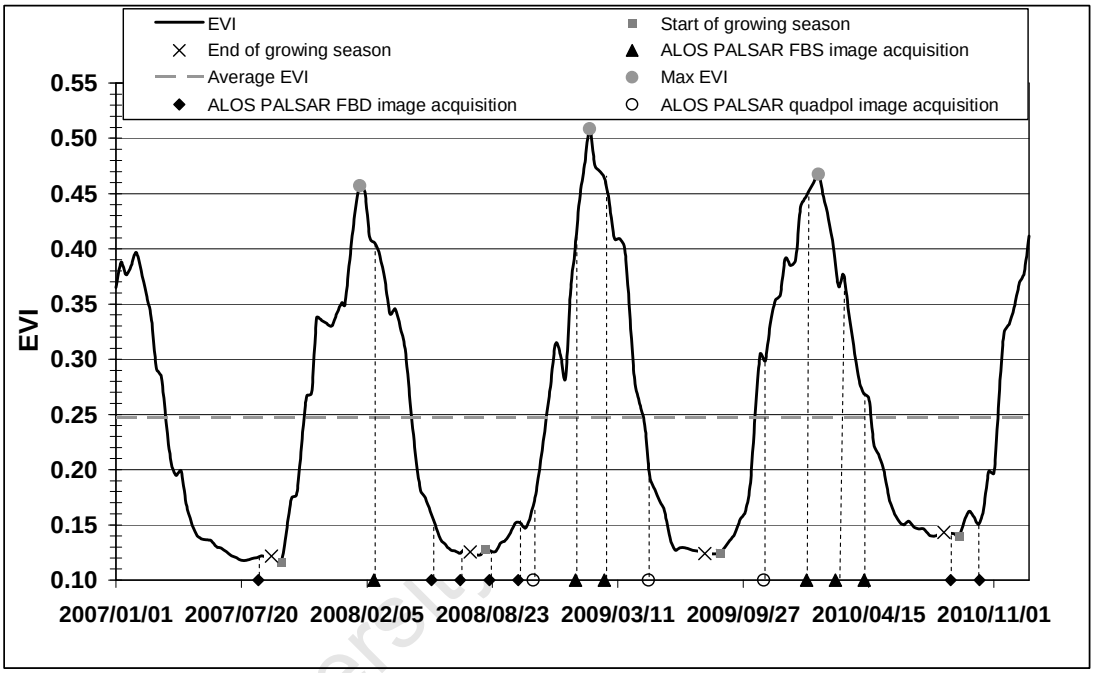

Figure 21: The phenology of the vegetation at the time of PALSAR image capture with the start and end of the growing seasons indicated (adapted from http://afis.meraka.org.za/wamis/time-series-viewer). The average EVI was calculated for a period between 2007/01/01 and 2010/12/27. The dates of PALSAR image acquisition are also indicated.

The majority of single polarisation TerraSAR-X scenes (both HH and VV polarisations) were captured during periods where the EVI values were high (Figure 22). On the other hand, most of the TerraSAR-X dual polarisation scenes were captured when the EVI was below average for the time series. The vegetative conditions at the time of image capture will play an important role in determining the viability of using dInSAR techniques for deformation monitoring. These effects will be further explored in Section 4.

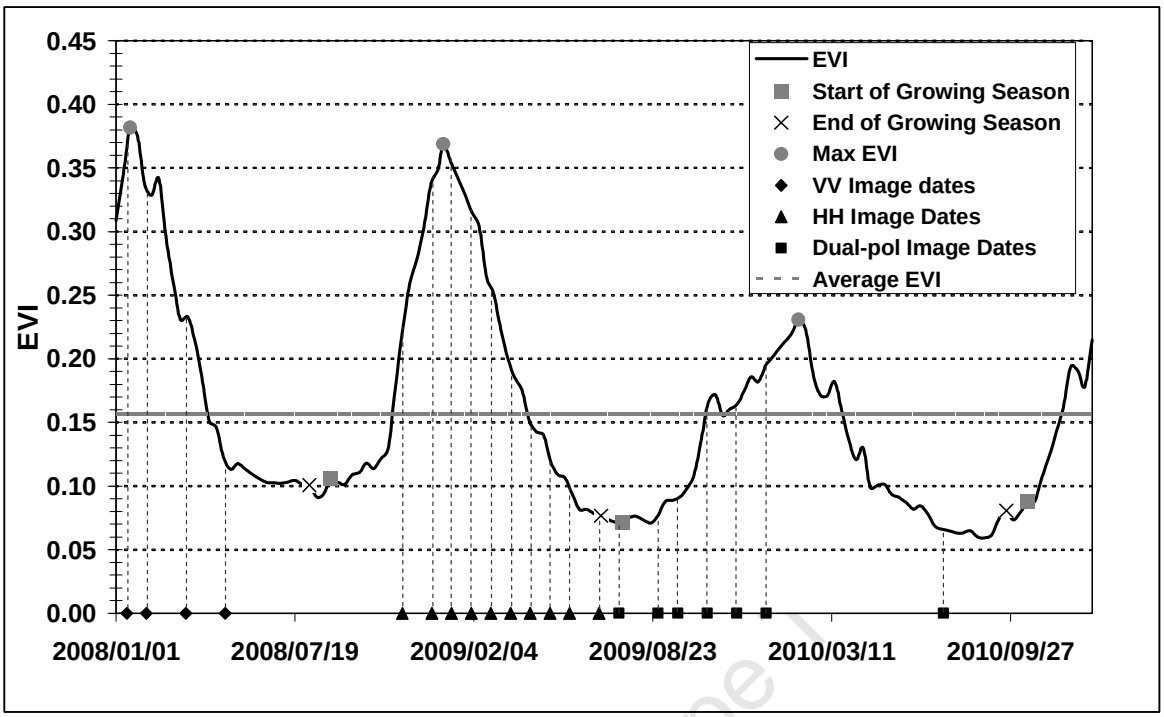

Figure 22: The phenology of the vegetation at the time of TerraSAR-X image capture with the start and end of the growing seasons indicated (adapted from http://afis.meraka.org.za/wamis/time-series-viewer). The average EVI was calculated for a period between 2008/01/01 and 2010/12/27. The dates of TerraSAR-X image acquisition are also indicated.

It should be noted that the EVI values used for the creation of Figure 19, Figure 21 and Figure 22 and used in this investigation are based on the EVI of a single representative point in the area of interest as extracted from the MODIS Time Series Viewer. To compare the point-based EVI values with the actual average MODIS EVI values for the area of interest, a subset of MODIS EVI scenes were obtained for a period between 2011/01/07 and 2011/02/11. When the MODIS EVI scenes were considered, it was found that the EVI values across the scenes are fairly homogeneous, especially after the growing season with standard deviation in EVI ranging between 0.089 and 0.019 in the summer and winter respectively. Additionally, a comparison between the average MODIS EVI and the point-based EVI values extracted from the MODIS Time Series Viewer (Figure 23) revealed that the EVI measurements from both sources varied only minimally with an average difference between MODIS Average EVI and the point-based EVI of 0.008.

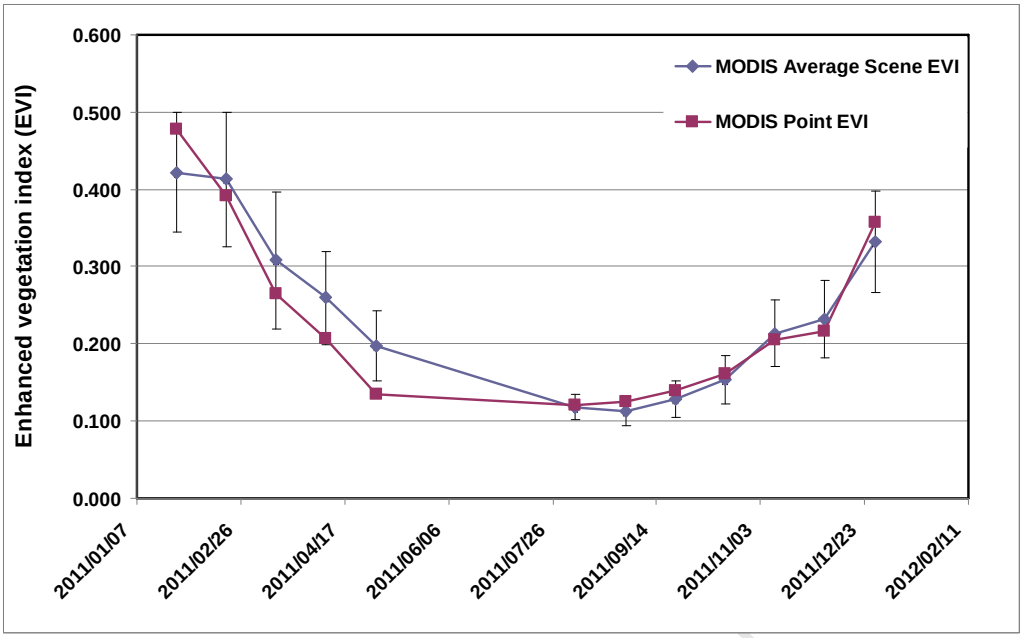

Figure 23: Comparison between the average scene EVI of a MODIS Scene and the point-based EVI measurements from the MODIS Time Series Viewer.

3.2 DATA PROCESSING

The dInSAR and polInSAR processing was performed using SARScape software that runs on the ENVI platform. Polarimetric image analysis (Section 4.4.1) was also performed in PolSARpro v4.2.0 software.

For interferometric analysis, the SAR scenes were imported into the SARscape platform which included the updating of orbital state vectors for ERS-2 and RADARSAT-2 scenes. Prior to interferometric analysis, the interferometric compatibility of two images (known as master/slave image pairs) needed to be verified in terms of baseline difference and Doppler centroid difference. The perpendicular baseline and Doppler centroid difference values were calculated and compared to the critical baseline and critical Doppler. The critical parameters for ERS-2, RADARSAT-2, ALOS PALSAR and TerraSAR-X data are summarised in Table 5. If the critical values were exceeded, the scenes were considered to be unsuitable for further processing. For dInSAR processing, suitable pairs underwent the processing sequence depicted in Figure 24.

Table 5: The critical baseline and Doppler for each data type.

	Critical Baseline	Critical Doppler
ERS-2	~950	~1673
RADARSAT-2	~3295	~1281
ALOS PALSAR (FBD Master)	~7761	~2124
ALOS PALSAR (FBS Master)	~15524	~2122
TerraSAR-X (Dual Pol)	~6205	~2945
TerraSAR-X (Single Pol)	~6063	~3716

Interferograms for each image pair was generated which included spectral shift filtering to filter out the effect of the shift in range spectra induced by baseline effects. Furthermore, the topographic and flat earth phase was removed by calculating the synthetic phase from topographic information obtained from the external digital elevation model. The synthetic phase essentially contains the low-frequency phase contribution due to topography as well as a constant phase contribution due to orbital variations between master/slave scenes. Following the removal of synthetic phase, the flattened differential interferogram was filtered and, during this step, the scene coherence was calculated that acted as an indication of the quality of the phase measurement. The filtering and coherence estimation was performed using the Goldstein filter with range and azimuth window size of 32 pixels and a low-pass filter percentage of 5%. The number of looks in range and azimuth direction for each scene type is reported in Table 6. Although the coherence information is not used explicitly for further processing and deformation measurement, the information was used to analyse the effect of various temporal and geometric decorrelation effects on the phase quality (Section 4). Filtered differential interferograms were then unwrapped using the Minimum Cost flow phase unwrapping process (SARscape 2009). Phase unwrapping problems due to phase noise resulted in residual phase islands and could be rectified using phase editing processes. Additionally, orbital refinement and re-flattening was performed to correct for the effects of orbital inaccuracies (especially important for datasets for which precise orbital state vectors were unavailable). The orbital refined and unwrapped phase was then converted to displacement maps.

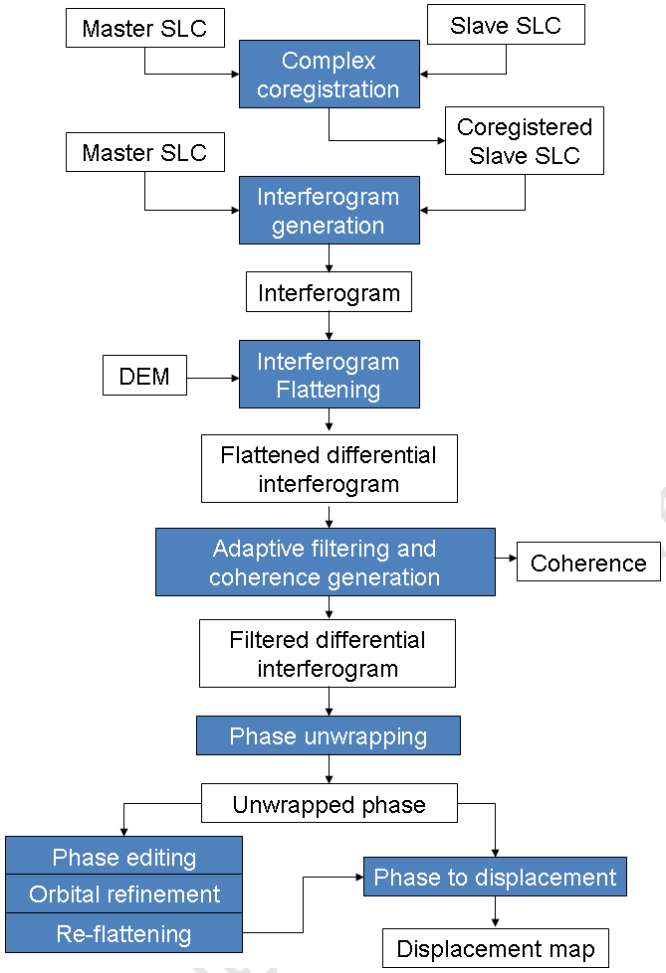

Figure 24: DInSAR processing sequence (adapted from (Kemp 2010)).

Table 6: Multilook processing in range and azimuth for each scene type.

	Azimuth Looks	Range Looks
ERS-2	4	1
RADARSAT-2	1	1
ALOS PALSAR (FBD Master)	3	1
ALOS PALSAR (FBS Master)	3	1
TerraSAR-X (Dual Pol)	1	1
TerraSAR-X (Single Pol)	1	1

To exploit polarimetric information for the purpose of coherence optimisation, the polInSAR processing sequence as illustrated in Figure 25 was performed. Since significant changes in the scattering mechanisms over time were experienced in the area (4.4.1), the Equal Scattering Mechanism (ESM) was deemed to be an unsuitable approach for the selection of the optimal polarisation and the MSM technique was used (Section 2.3.2). The coregistration of master/slave scenes were performed ensuring sub-pixel co-registration of all HH, HV, VH and VV channels. The coregistered data was then used together with a digital elevation model to generate the synthetic phase information which was used for the removal of flat earth and topographic phase. The coregistered single look complex (SLC) data and synthetic phase information was then used as input into the coherence optimisation process. The coherence optimization algorithm operates by the identification of the main scattering mechanisms in the fully polarimetric scenes and identifies the scattering mechanisms that correspond to the highest interferometric coherence as well as intermediate and minimum coherence products. The interferogram associated with the maximum coherence product then underwent flatting and phase unwrapping processes to derive deformation maps.

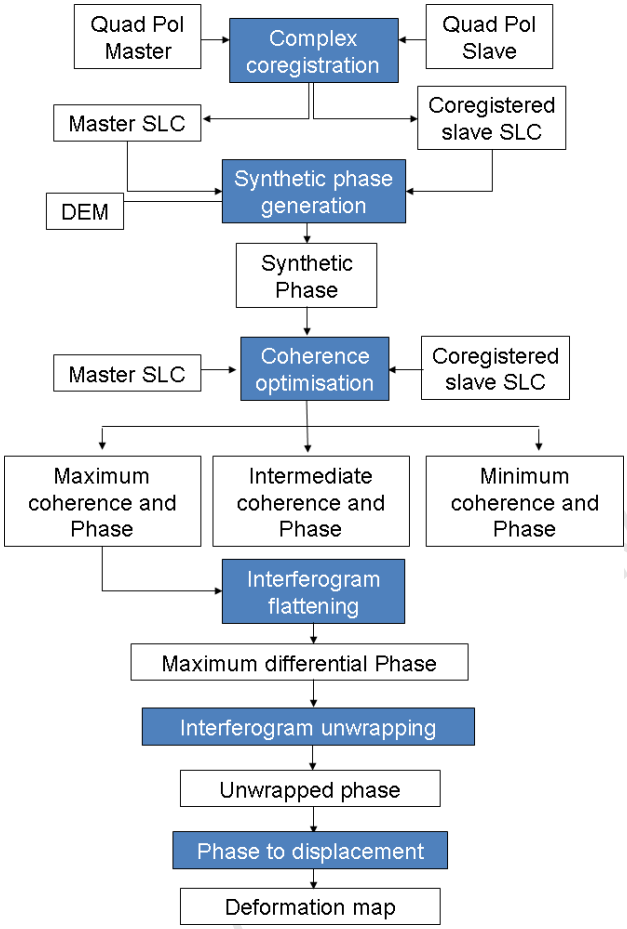

Figure 25: PolInSAR processing sequence.

4 RESULTS: DINSAR ANALYSIS – PARAMETERS AFFECTING SCENE COHERENCE

Since temporal and geometric decorrelation effects will influence the ability to successfully measure and monitor surface deformation due to mining activities, the ideal would be to identify the optimal image acquisition strategy in terms of wavelength, temporal frequency and orbital attributes that can be used for the long term operational monitoring of subsidence due to mining. However, since the tasking of satellite borne image acquisitions can be expensive, the ideal would be to minimise the temporal frequency of acquisitions until such a time that free and open access data becomes routinely available.

The availability of C-band, L-band and X-band data captured at a variety of different polarisation states as well as different orbital and temporal configurations implies that the effects of temporal and

geometric decorrelation could be investigated in detail. Statistical analysis of the parameters and their effect on average scene coherence was achieved through the calculation of statistical correlation coefficients. Where plots of the average scene coherence against the parameters affecting coherence revealed that the relationship between variables was non-linear, the data was transformed into the linear domain to facilitate statistical analysis through Pearson correlation coefficients. Sections 4.1, 4.2 and 4.3 present the results of the analysis of the parameters affecting scene coherence for C-band, L-band and X-band data respectively. This was performed to establish the different sensitivities of scene coherence to the various temporal and geometric parameters for data captured at different wavelengths. The information can be used to design an optimal image acquisition strategy for long term operational monitoring of subsidence due to mining in a dynamic agricultural environment.

4.1 C-BAND DATA

Both ERS-2 and RADARSAT-2 scenes were available to investigate the effects of temporal and geometric decorrelation on C-band data. The parameters considered to affect scene coherence include temporal baseline, land surface evolution, perpendicular baseline and Doppler centroid difference. Additionally, since the RADARSAT-2 data was captured at quadrature polarisation (HH, HV, VH and VV) the effect of polarisation on interferometric coherence could be investigated. In this regard, HH, HV and VV polarisation data was used to create interferograms for each interferometric pair. The VH polarisation was not used for interferometric analysis since, assuming a monostatic radar system and reciprocity of the target, the HV and VH polarisations are the same (Stebler et al. 2002).

All RADARSAT-2 scenes were interferometrically compatible in terms of B_{perp} and Doppler centroid difference. This yielded 66 interferometric pairs for further analysis. To simplify the process of the statistical analysis of coherence values for each interferometric pair, the average scene coherence for each interferometric pair was determined as a global average for each pair. Since different crop types occur in the investigated area, the average scene coherence for each crop type was also calculated to confirm if the global average coherence was representative for different land cover types as well. For RADARSAT-2 data, the global average coherence for each interferometric pair indicated a strong positive correlation with the average coherence calculated for each crop type. This is illustrated in Figure 26 for a subset of interferometric pairs. Consequently, only the global average coherence for

each interferometric pair was considered for further analysis. The frequency distribution of the average scene coherence for each RADARSAT-2 interferometric pair is summarised in Figure 27 for HH, HV and VV polarisations. Additionally, the frequency distribution of Doppler centroid difference, B_{perp} and temporal baseline for each RADARSAT-2 pair is summarised in Figure 28 A, B and C respectively.

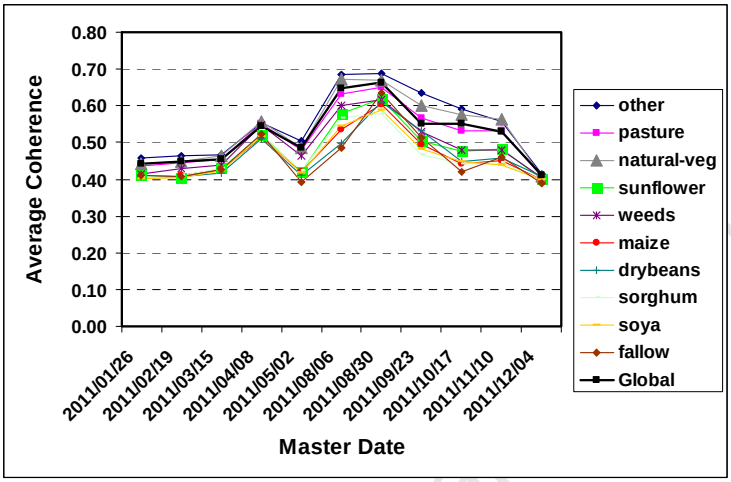

Figure 26: The global average scene coherence for a selection RADARSAT-2 pairs compared to the average coherence per land cover class

On calculation of the perpendicular baseline and DC difference for ERS-2 scenes, it was observed that a large number of pairs were not suitable for interferometric analysis since the Doppler centroid difference exceeded the critical Doppler or the perpendicular baseline exceeded the critical baseline. This reduced the number of interferometrically compatible scenes from the theoretical 91 pairs if all scenes were compatible with one another, to 38 scenes that could be used for interferogram generation. The frequency distribution of the Doppler centroid difference, perpendicular baseline and temporal baseline for the interferometrically compatible ERS-2 scenes is presented in Figure 29 A, B and C respectively. The frequency distribution of average scene coherence obtained for ERS-2 data is presented in Figure 30.

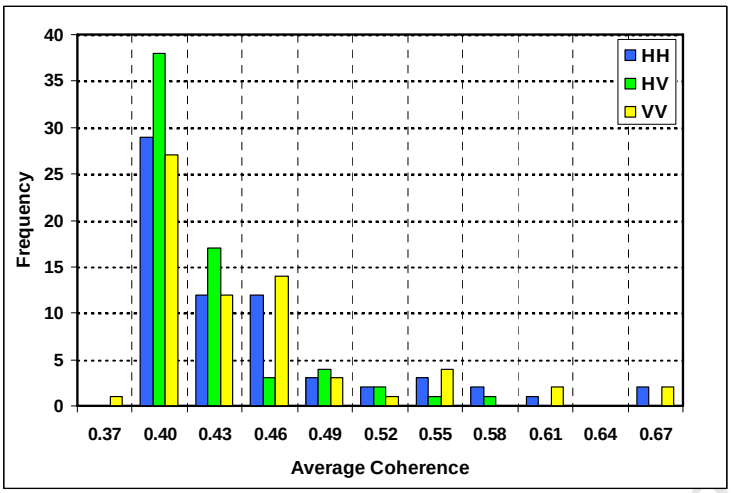

Figure 27: The frequency distribution of average scene coherence values obtained from dInSAR processing of RADARSAT-2 data in HH, HV and VV polarisations.

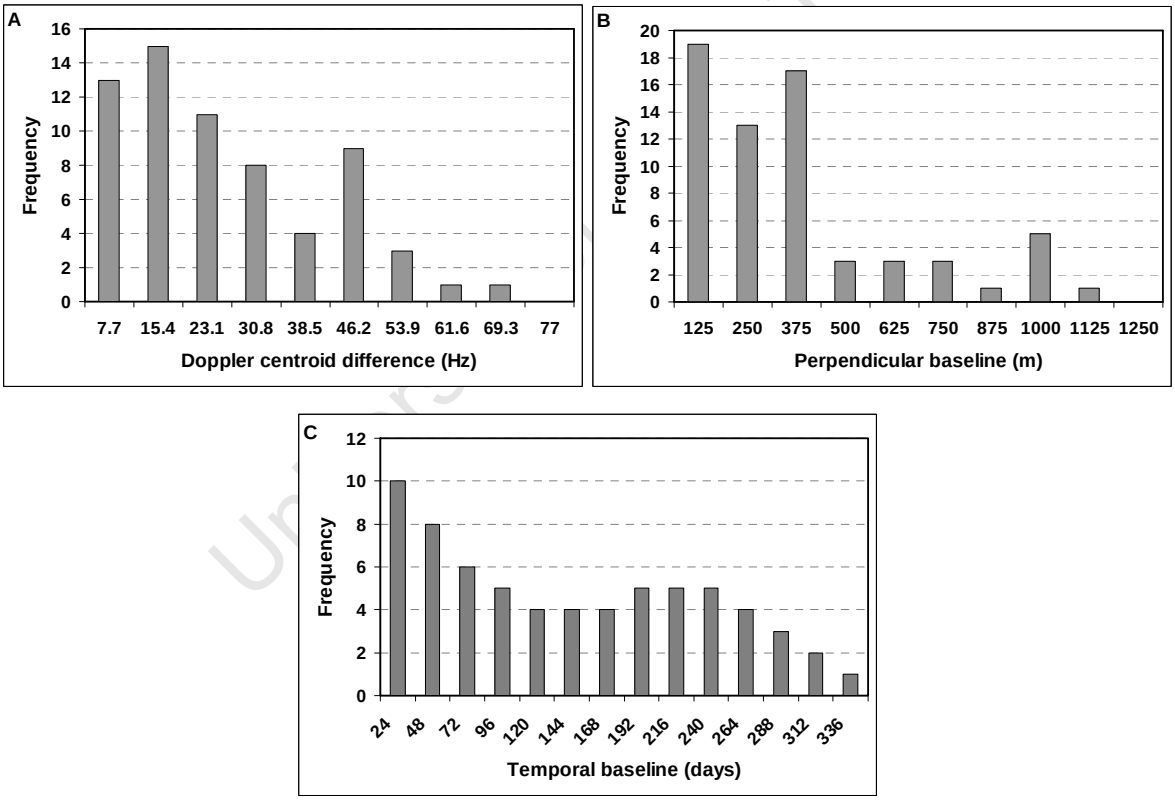

Figure 28: The frequency distribution of RADARSAT-2 parameters considered to affect interferometric coherence. A: Doppler centroid difference, B: Perpendicular baseline and C: temporal baseline.

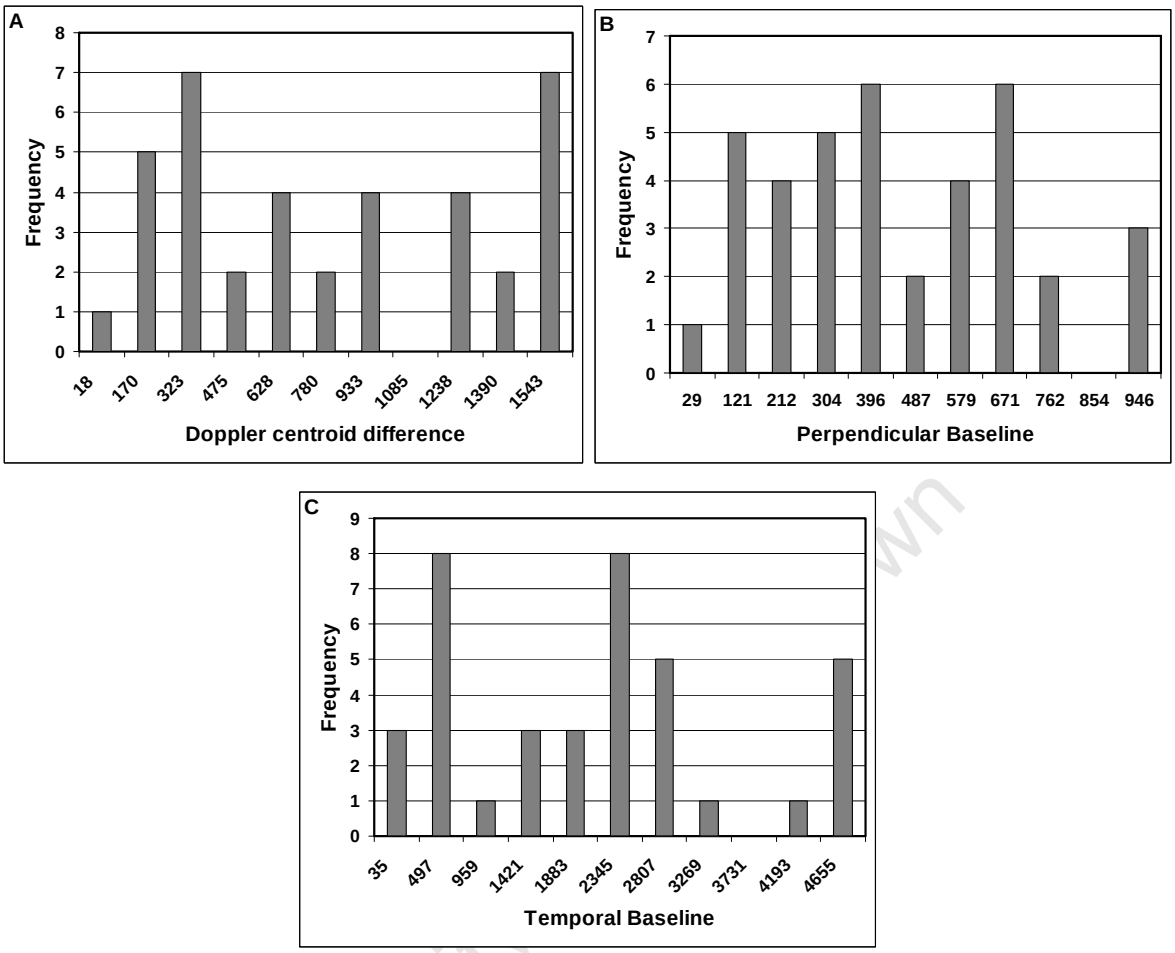

Figure 29: The frequency distribution of parameters considered to affect interferometric coherence. A: Doppler centroid difference, B: Perpendicular baseline and C: temporal baseline for ERS-2 data.

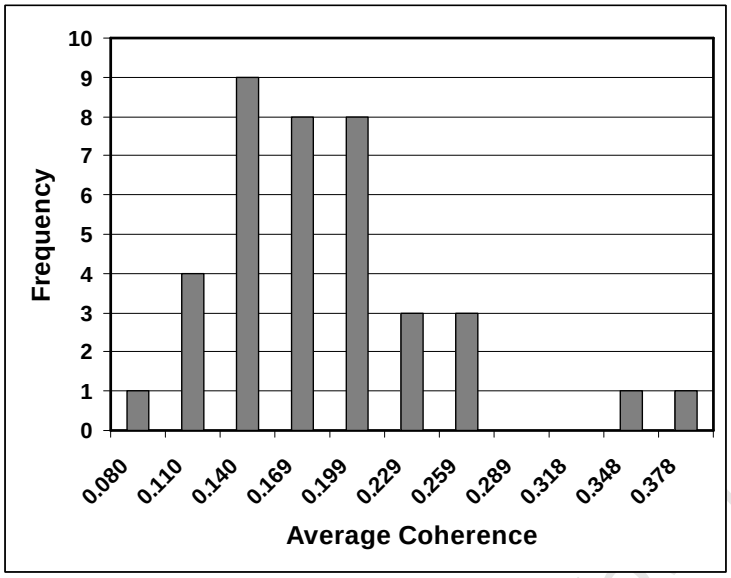

Figure 30: The frequency distribution of average scene coherence values obtained for ERS-2 data.

Sections 4.1.1 to 4.1.2 examine the temporal and geometric effects on C-band interferometric coherence to determine those parameters that are most detrimental to successful interferogram generation and deformation mapping.

4.1.1 The effect of perpendicular baseline and Doppler centroid difference

Since an increase in both perpendicular baseline and Doppler centroid difference is associated with a loss of interferometric coherence (Section 2.2), the effect of these parameters on the average scene coherence was assessed. To determine the sensitivity of C-band data to these effects, ERS-2 and RADARSAT-2 average scene coherence were correlated to the respective DC difference and perpendicular baseline conditions (Table 7). The results reveal that ERS-2 data is most sensitive to Doppler Centroid difference with Pearson correlation (ρ) of -0.533 and slightly less sensitive to effects of perpendicular baselines (ρ = -0.523). The results further show that no correlation exists between the DC difference of a RADARSAT-2 pair, and the coherence of the resulting scene (ρ = 0.071, 0.056 and 0.065 for RADARSAT-2 HH, HV and VV polarisation respectively). This is in contrast to the findings with ERS-2 data in the same area for which DC difference was found to have the strongest correlation (ρ = -0.533). The explanation for this inconsistency is that, given a critical DC difference of ~1281 Hz for the RADARASAT-2 InSAR pairs, the actual Doppler centroid difference values of between 2.032 Hz and 51.310 Hz for the pairs is relatively small (0.2 – 4.0% of critical Doppler). In contrast, the ERS-

2 data provided a critical Doppler of ~1679 Hz and exhibited DC difference values between 17.56 and 1543 Hz (Figure 29 A).

Table 7: The Pearson correlation between average scene coherence and DC difference and B_{perp} for C-band (ERS-2 and RADARSAT-2 HH (RS HH), HV (RS HV) and VV (RS VV)) data.

	ERS-2	RS HH	RS HV	RS VV
Correlation with B_{perp}	-0.523	-0.331	-0.291	-0.340
Correlation with DC difference	-0.533	0.071	0.056	0.065

For B_{perp}, a weak negative correlation exists with average scene coherence of RADARSAT-2 data (-0.331, -0.291 and -0.340 for HH, HV and VV polarisation respectively) (Table 7). This correlation is weaker than the correlation observed for ERS-2 data for which the correlation between coherence and B_{perp} was ρ= -0.523. While an increase in B_{perp} is expected to yield a decrease in coherence, the fact that this correlation for RADARSAT-2 data is fairly low is also most likely related to the critical baseline for RADARSAT-2. The RADARSAT-2 pairs used had perpendicular baselines of between 5 and 1251 m (average 326 m) (Figure 28), while the critical baseline for RADARSAT-2 is ~ 3219 m. However, it is observed that only 21% of the data points were captured with a B_{perp} > 15% of the critical baseline. The effect of smaller B_{perp} values are illustrated in Figure 31 where it is observed that a higher variance in coherence values are observed for B_{perp} < 505 m (15% of critical baseline) whilst larger B_{perp} values are associated with a lower variance in coherence values. The results suggest that, at B_{perp} < 15% of the critical baseline, factors other than B_{perp} are affecting the average scene coherence in a more prominent way.

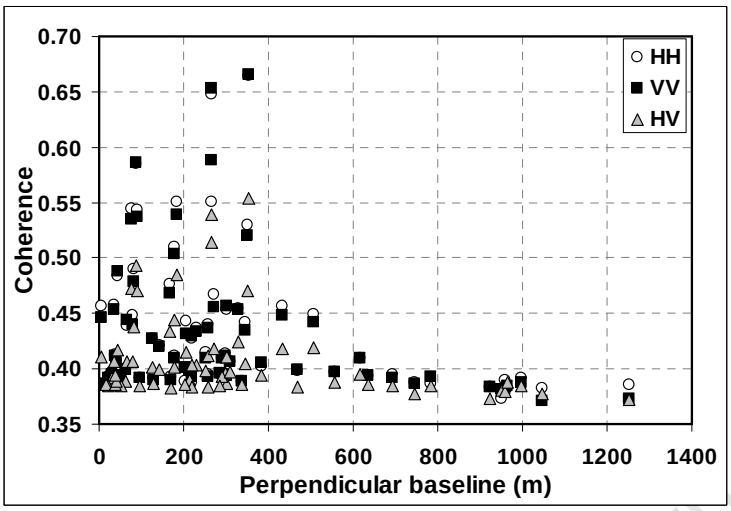

Figure 31: Average scene coherence as a function of perpendicular baseline.

4.1.2 Temporal baseline and land surface evolution

Temporal decorrelation in dInSAR occurs due to two processes: 1) changes that occur due to the evolution of the land cover conditions (such as crop growth, harvesting, tilling etc.) and 2) temporal decorrelation due to random rearrangement of scattering elements (such as movement of twigs and leaves) (also referred to as volume decorrelation) (Section 2.2). When the effect of increasing temporal baseline is considered, a strong negative correlation is observed between average scene coherence and temporal baseline for RADARSAT-2 data in all polarisations (ρ = -0.669, -0.654 and -0.646 for HH, HV and VV polarisation respectively) (Table 8). On the other hand, a weaker correlation between ERS-2 coherence and temporal baseline is observed (ρ = -0.346). The apparent decreased sensitivity of ERS-2 data to temporal decorrelation effects is due to the increased effect of geometric decorrelation (perpendicular baseline and Doppler centroid difference) for ERS-2 data (Section 4.1.1). Additionally, ERS-2 scenes were captured either before or after the peak of the growing seasons during periods with lower vegetation densities (Section 3.1.5). This would result in a decrease in volume decorrelation and, consequently, an apparent decrease in sensitivity to temporal decorrelation.

Table 8: The correlation between temporal baseline and average scene coherence for ERS-2 and RADARSAT-2 data (RS = RADARSAT-2).

	ERS-2	RS HH	RS HV	RS VV
Correlation with B_{temp}	-0.346	-0.669	-0.654	-0.646

To investigate the effect of land surface evolution, the change in enhanced vegetation index (EVI, Section 3.1.5) between the master and slave image acquisitions (δEVI) were calculated as a proxy for the change in land surface conditions. Since either positive or negative changes would influence the scene coherence, the absolute value of the δEVI (|δEVI|) was used to investigate the effect of changing land surface conditions on average scene coherence. The frequency distribution of |δEVI| values for RADARSAT-2 interferometric pairs is presented in Figure 32. Since EVI values were available only since 2000/02/26, the effect of evolving land surface conditions on ERS-2 could be considered only for 11 interferometric pairs (Figure 33) with data captured after 2000/02/18 and was not considered for statistical analysis.

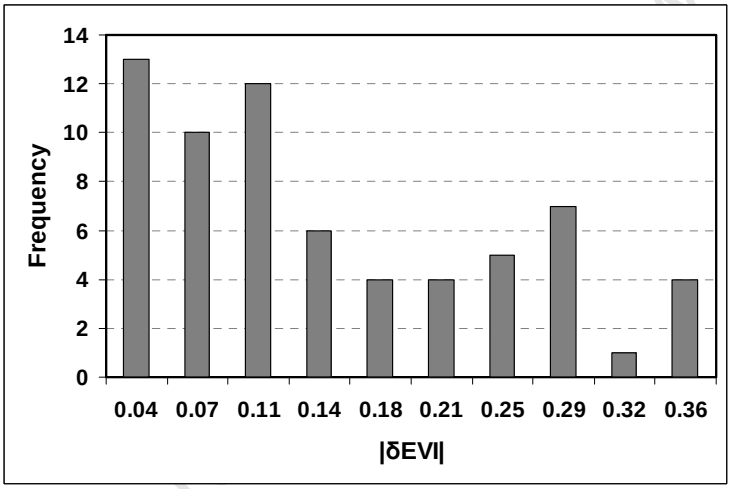

Figure 32: The frequency distribution of the change in EVI ($|\delta EVI|$) of the surface between the RADARSAT-2 master/slave image pairs.

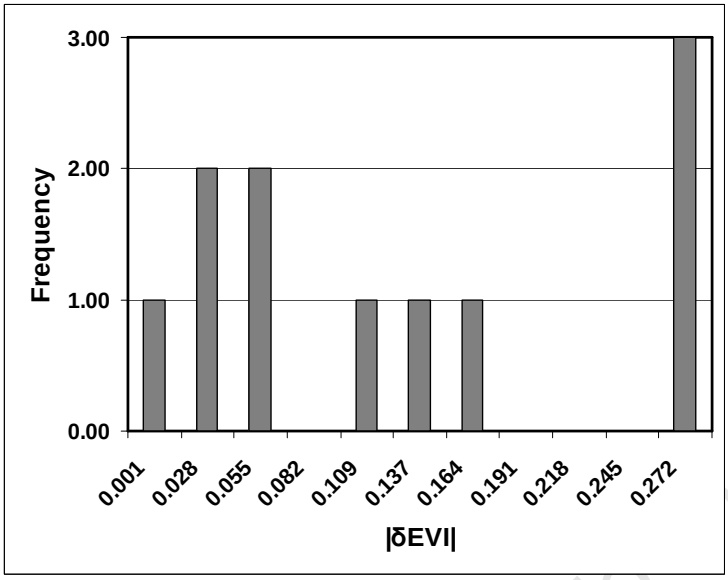

Figure 33: The frequency distribution of $|\delta$EVI| for ERS-2 master/slave image pairs captured after 2000/02/18.

When considering the effect of land surface evolution on average scene coherence, the results suggest that a moderate negative correlation exists between |δEVI| and average scene coherence of RADARSAT-2 scenes, with ρ = -0.589, -0.595 and -0.539 for HH, VV and HV polarisations, respectively. Presenting the relationship between land surface evolution and average scene coherence graphically (Figure 34) reveals that, for |δEVI| > 0.15, the effect of land surface evolution on average scene coherence in all polarisations becomes less pronounced with average scene coherence ranging between 0.37 and 0.46. This suggests a saturating logarithmic decrease in average scene coherence with increasing land surface evolution. This suggests that the average scene coherence will decrease exponentially until a saturation point is reached after which any additional changes in the land surface would no longer affect the average scene coherence.

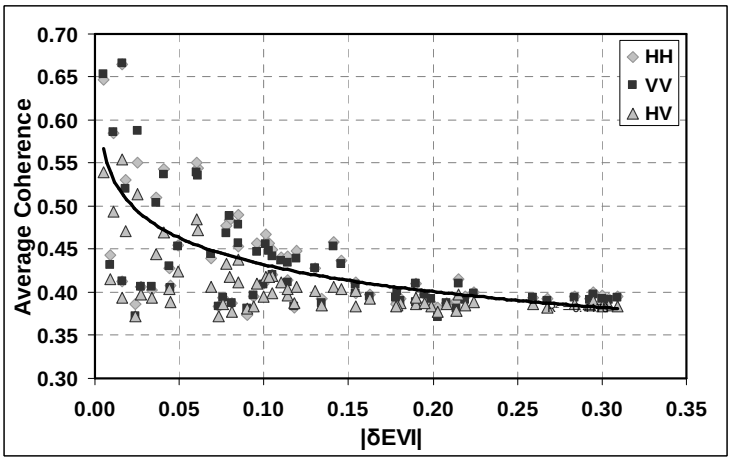

Figure 34: The effect of the evolution of the land surface on average scene coherence for RADARSAT-2 interferometric pairs.

It was observed that, for |δEVI| < 0.10, a greater variability in coherence values is present and that low |δEVI| values could also be associated with low coherence. The apparent decrease in sensitivity of coherence values in the low |δEVI| region is related to the vegetation densities at the time of master and slave image acquisition. If both master and slave images are captured during high EVI timeframes, the resulting |δEVI| may be low. However, the higher densities of vegetation at the time of image acquisition are expected to result in an increase in volume decorrelation and, consequently, a decrease in coherence. This can be examined by considering the EVI at the specific time that the master and slave scene was captured. To illustrate this effect, the average scene coherence of pairs with the same temporal baseline (24 days) was considered in relation to the recorded EVI values on the day that the RADARSAT-2 master and slave scenes were captured (Figure 35). It was observed that, when used in pairs with 24-day temporal baseline, master scenes captured during a period where the EVI is low would result in higher scene coherence than master scenes captured during a period where EVI is high. Similarly, interferometric coherence for pairs with low EVI during slave image acquisition were higher than the coherence for pairs captured during a time where high EVI values were recorded at the time of slave image acquisition.

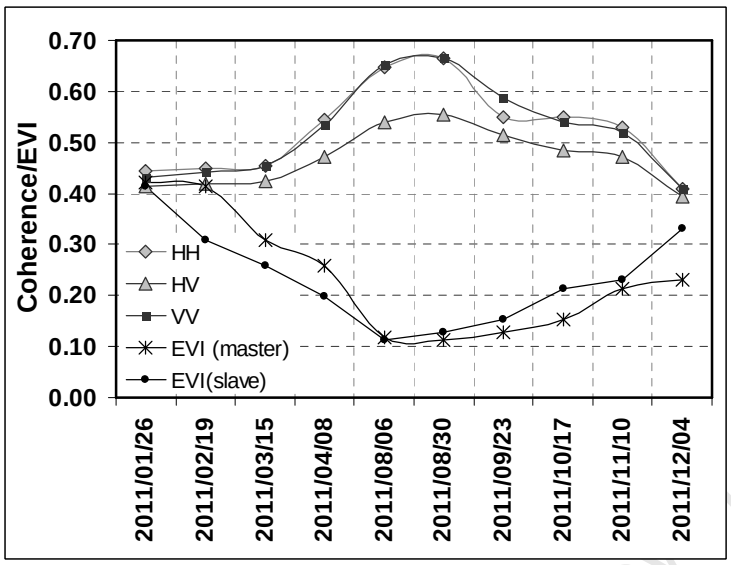

Figure 35: The average scene coherence for InSAR pairs with 24-day temporal baselines compared to the EVI at the time of master and slave image capture.

4.1.3 The effect of polarisation

The availability of RADARSAT-2 scenes captured at multiple polarisations allowed for the exploration of the effects of polarisation on scene coherence. To investigate the effect of polarisation on the average scene coherence in the study area, each InSAR pair was processed using HH, HV and VV polarisation and the average scene coherence was determined. Figure 36 is a graphic presentation of the average scene coherence (for HH, HV and VV polarisation data) in relation to the temporal baseline. The results reveal that the average coherence of HH polarisation interferograms was consistently higher than coherence associated with HV interferograms while being similar to VV interferograms. However, it is observed that the differences between scene coherence in different polarisations become less pronounced as temporal baseline increases. This convergence suggests that, as the temporal baseline increases, the average scene coherence in HH, HV and VV polarisation approaches similarity and, for large temporal baselines, the influence of polarisation on the average scene coherence decreases. This is due to a general decrease in coherence with an increase in temporal baseline across all polarisations which is discussed in Section 4.1.2.

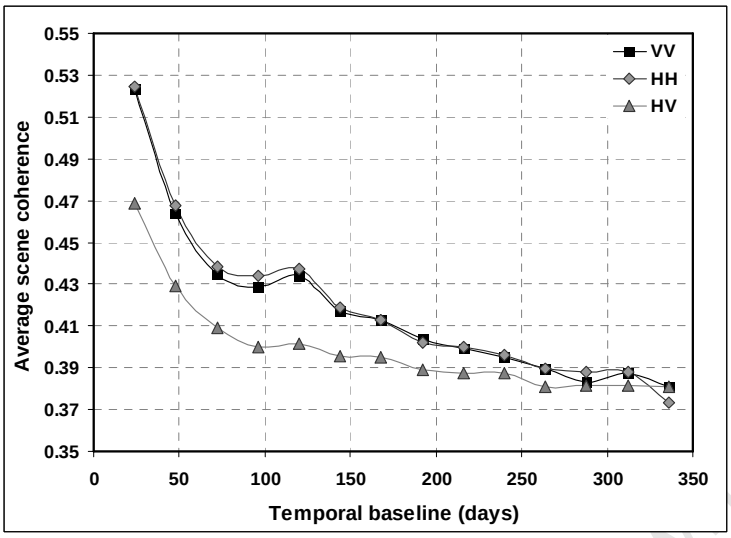

Figure 36: The mean scene coherence of each interferometric pair for HH, HV and VV polarisation.

The results also suggests that the different polarisations are strongly correlated with each other with a Pearson correlation coefficient of 0.994 for HH and VV polarisation, 0.982 for HH and HV polarisation and 0.988 for VV and HV polarisation. This suggests that external effects affecting the average scene coherence affects all polarisations in a similar way, most prominently for HH and VV polarisations. Since the coherence of pure volume scattering contributions are known to be independent of polarisation whilst the coherence of surface scattering contributions will be polarisation dependent, the results suggest that volume scattering effects may have a significant influence on the scene coherence.

Since the interaction of electromagnetic radiation with a specific land cover is different for the different polarisations, the strong correlation between the average scene coherence in the different polarisations is surprising. Specifically, since vertical crops dominate the land surface, HH polarisation data is expected to interact predominantly with the surface whilst VV polarisation signals will interact with the vertical crops (Section 2.3.2). Therefore, a change in land surface conditions, including crop growth and harvesting, is expected to affect the VV polarisation data more significantly when compared to HH polarisation. However, changes due to crop growth would change the leaves and smaller branches but will not significantly change the vertical stalks of crops with which the VV polarisation interacts. Therefore, the VV polarisation signal appears not to be affected by the crop growth phase as significantly as expected. Additionally, since the HH polarisation is expected to interact predominantly with the ground surface which is not affected by crop growth, the average scene coherence in HH and

VV polarisation is similar. It should be noted that, as described in Section 2.3.2, the interaction of the different polarisations with different surfaces (stalk surface for VV signals and ground surfaces for HH signals) will introduce a topographic phase component in differential interferograms if VV polarisation signals are used.

Although HH polarisation exhibits higher coherence values than VV polarisation in most cases, the difference in coherence values is less than 0.01. However, in certain cases, VV polarisation exhibits higher scene coherence than HH polarisation. It is observed that instances where VV polarisation exhibits higher average scene coherence than HH polarisation predominantly occurred during the times of image capture between 2011/05/02 and 2011/12/04, which is the period after harvesting took place but before the peak of the next growing season is reached. The lower EVI values exhibited during this period (Section 4.1.2) suggest that vegetation biomass was low, which increased the probability of surface interaction, even for VV polarisation data. Land surface conditions and the evolution of the land surface therefore affect the choice of optimal polarisation data required for long term monitoring with HH polarisation being more suitable in the peak of the growing season where vegetation density is high. VV polarisation, in contrast, is more suitable after harvesting and before the peak of the next growing season is reached.

4.2 L-BAND DATA

The use of PALSAR data for deformation monitoring was investigated since the longer wavelength (~ 23 cm) compared to C-band data (~5 cm) is expected to penetrate further into vegetation, thereby decreasing the effect of land cover evolution on the average scene coherence. The scene acquisition times for PALSAR scenes were not as regular as the acquisition times for the RADARSAT-2 scenes obtained. For PALSAR datasets, image acquisitions took place at time intervals of between 46 and 322 days. Datasets were acquired in single (FBS) and dual polarisation (FBD) modes. Additionally, three scenes were captured in fully polarimetric mode. The FBS and FBD polarisation images were interferometrically compatible as long as the same polarisation (HH and HH as opposed to HH and HV) were used for interferogram generation. The three scenes, captured in quad polarisation mode although limited in number, could be used to investigate the effect of polarisation on the average scene

coherence and for coherence optimisation in Section 4.4.2. Furthermore, the FBS and FBD scenes were used to investigate temporal and geometric decorrelation effects.

To simplify the statistical analysis of interferometric coherence with the various parameters affecting the coherence, the global average coherence for each interferometric pair was used. To confirm that global coherence for each pair was representative for different land cover types as well, the average coherence for each crop type was extracted for a subset of interferometric pairs. Similar to the observation for RADARSAT-2 data, the global average coherence for each PALSAR interferometric pair indicated a strong positive correlation with the average coherence calculated for each crop type. This is illustrated in Figure 37 for a subset of interferometric pairs. Consequently, only the global average coherence for each interferometric pair was considered for further analysis.

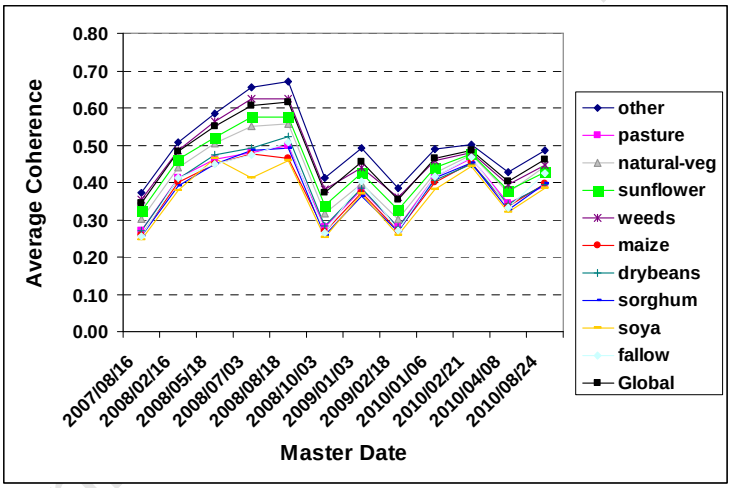

Figure 37: The global average scene coherence for a selection PALSAR pairs compared to the average coherence per land cover class

Since FBS and FBD scenes were interferometrically compatible, interferometric combinations with FBS as master and FBS as slave (FBS-FBS), FBD as master and FBD as slave (FBD-FBD), FBS as master and FBD as slave (FBS-FBD) and FBD as master and FBS as slave (FBD-FBS) were possible. The frequency distribution of the average scene coherence for all interferometric combinations is presented in Figure 38. Additionally, the Doppler centroid difference, perpendicular baseline, temporal baseline and $|\delta \mathrm{EVI}|$ for each pair are presented in Figure 39 A, B, C and D respectively. The average scene coherence values for PALSAR polarimetric pairs are presented in Table 11, Table 12 and Table

13 for HH, HV and VV polarisations respectively. It is observed that the average scene coherence values for the PALSAR data are generally lower than the average scene coherence values observed for RADARSAT-2 data. This is likely due to the significantly larger temporal baselines associated with ALOS PALSAR interferometric pairs (Figure 39 C) compared to the temporal baselines for RADARSAT-2 scenes (Figure 28 C).

Sections 4.2.1 to 4.2.2 analyses the effect of the various parameters on the interferometric coherence to determine those parameters that are most detrimental to successful interferogram generation and deformation mapping.

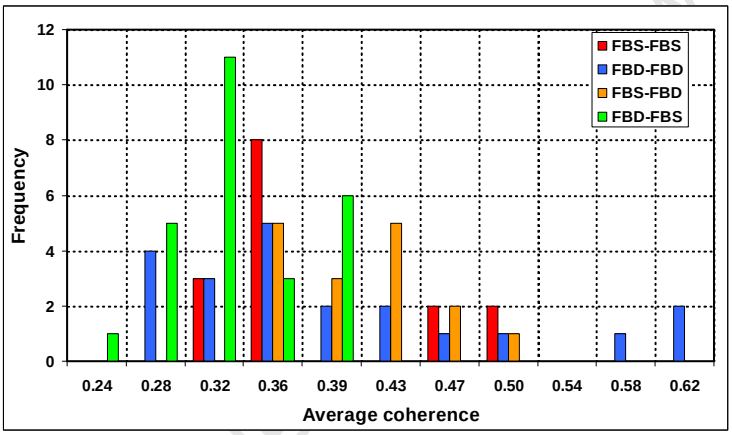

Figure 38: The frequency distribution of the average scene coherence of PALSAR HH polarisation interferometric pairs.

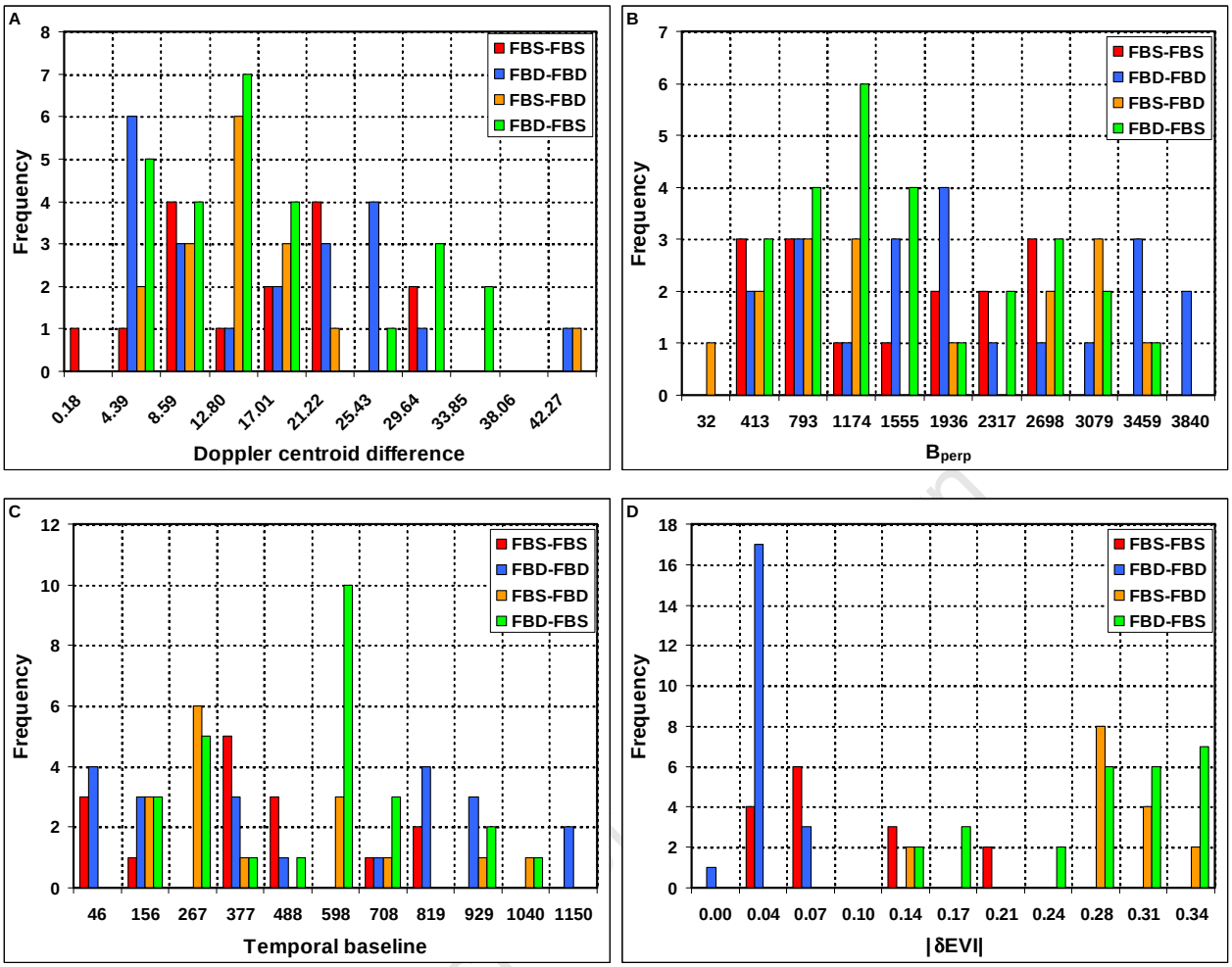

Figure 39: The frequency distribution of the parameters affecting coherence for PALSAR HH interferometric pairs. A: Doppler centroid difference, B: Perpendicular baseline and C: temporal baseline.

4.2.1 The effect of perpendicular baseline and Doppler centroid difference

To determine the effect of an increase in perpendicular baseline on the interferometric coherence for L-band data, the correlations between the two parameters were calculated. It should be noted that both dual polarisation (FBD) and single polarisation (FBS) scenes were available for interferometric processing and that FBD scenes are interferometrically compatible with FBS scenes and vice versa. However, different range resolutions (R_r) apply for the different image modes with R_r = 5.547 for FBS scenes and R_r = 11.094 for FBD scenes which translates to different critical baselines. The reported

critical baselines for interferometric pairs created using a dual polarisation scene (FBD) as master was ~ 7 762 m whereas pairs using a single polarisation scene (FBS) as master reported critical baselines of ~ 15 520 m.

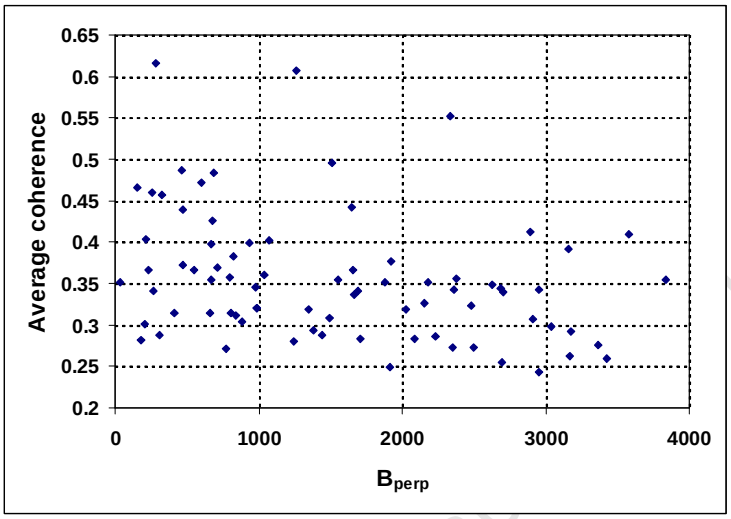

Figure 40: The effect of perpendicular baseline on PALSAR interferometric coherence.

The different interferometric combinations of FBS and FBD scenes lead to different sensitivities to B_{perp} (Table 9). For FBS-FBS scenes, the correlation between B_{perp} and interferometric coherence was ρ = -0.540, higher than the correlation between B_{perp} and FBS-FBD pairs (ρ = -0.314), even though the critical baselines were similar. Similarly, the correlation between FBD-FBS scenes and B_{perp} was ρ = -0.640, higher than FBD-FBD scenes (ρ = -0.371) although their critical baselines were equal.

Table 9: The correlation between average scene coherence and B_{perp} for different interferometric combinations of PALSAR FBS and FBD scenes (N is the number of pairs for each combination).

	B_{perp}
Average coherence FBS-FBS (N = 15)	-0.540
Average coherence FBD-FBD (N = 21)	-0.371
Average coherence FBS-FBD (N = 16)	-0.314
Average coherence FBD-FBS (N = 26)	-0.640

When the B_{perp} is considered as a percentage of the critical baseline (Figure 41), it is observed that a large number of FBD-FBD scenes have B_{perp} higher than 15% of the critical baseline. This suggests that a higher sensitivity of average scene coherence to B_{perp} could be expected. However, as mentioned

in Section 2.2, the interferometric coherence of ground scattering mechanisms are less sensitive to baseline decorrelation effects, even at higher perpendicular baselines. Since FBD scenes are captured during periods where the vegetation densities were low (Section 3.1.5), it is expected that the larger portion of backscatter is contributed from surface scattering mechanisms, thereby minimising the baseline decorrelation effects of FBD-FBD pairs. The FBS scenes on the other hand were captured during the peak of the growing seasons, a time during which the vegetation densities were high. Even though B_{perp} values were lower than 20% of the critical baseline for all instances, a high sensitivity to B_{perp} is reported (ρ = -0.540). This suggests that an increase in volume scattering and a decrease in ground scattering contributions are increasing the sensitivity to baseline decorrelation effects for these scenes.

The highest sensitivity to B_{perp} is reported by FBD-FBS scenes with (ρ = -0.640). It is observed that 19 FBD-FBS scenes exceed 15% of the critical baseline with 8 of these scenes exceeding 30% of the critical baseline. Additionally, since the FBS slave scenes are captured during the peaks of the growing seasons, the increase in volume scattering contributions are increasing the sensitivity to baseline decorrelation effects. Therefore the highest sensitivity of FBD-FBS pairs to baseline decorrelation effects is expected. Although the FBS-FBD scenes are also associated with an increase in volume scattering contributions, only 7 B_{perp} values exceeds 15% of the critical baseline and none exceed 30% of the critical baseline. Therefore a reduced sensitivity to baseline decorrelation effects of ρ = -0.314 is observed. The characteristics of the land cover at the time of image capture appear to be influencing the sensitivity to baseline decorrelation effects. The land cover effects will be further explored in Section 4.2.2.

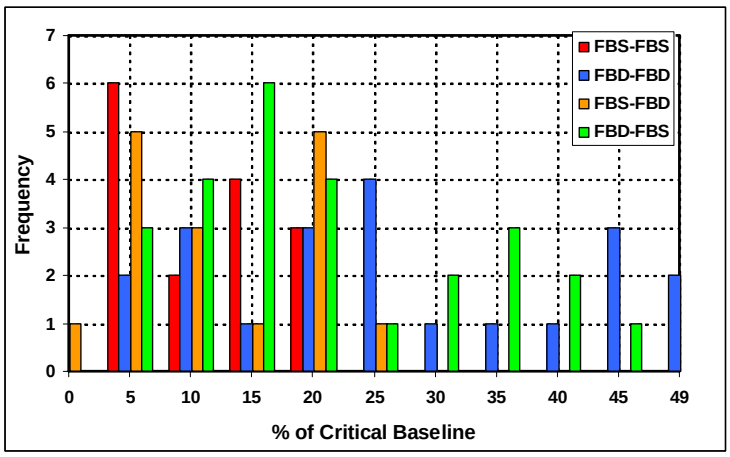

Figure 41: Perpendicular baseline as a percentage of the critical baseline.

A weak correlation between Doppler centroid difference and average scene coherence was also observed with ρ = 0.122. It is observed that the critical Doppler for PALSAR scenes was between 2118.64 and 2127.66 (irrespective of acquisition mode) whilst the actual Doppler centroid difference recorded was between 0.18 and 42.27 (0.01% - 2.00% of critical Doppler). This suggests that, since the Doppler Centroid difference for each interferometric pair is relatively small when compared to the critical Doppler, the effect of Doppler centroid difference on average scene coherence is minimal and other parameters are affecting the average scene coherence in a more prominent way. It is expected that larger Doppler centroid differences would affect the average scene coherence more significantly.

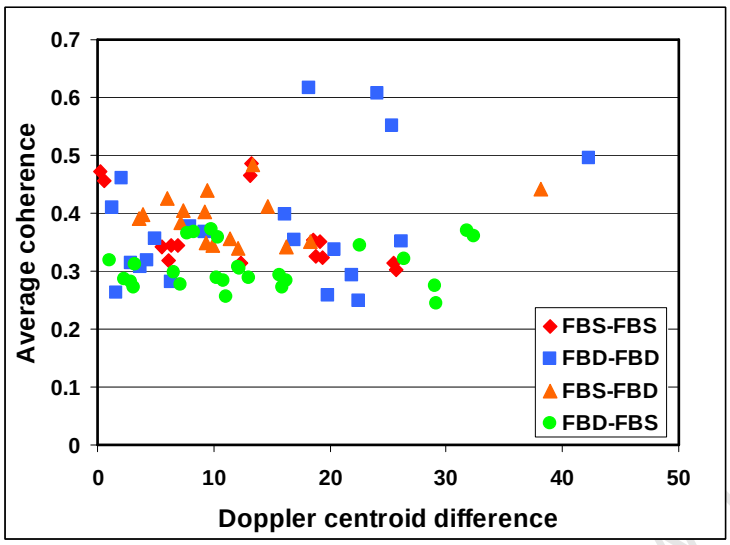

Figure 42: The relationship between average scene coherence and Doppler centroid difference for PALSAR data.

4.2.2 The effect of temporal baseline and land surface evolution

Since temporal effects on C-band data was a significant source of decorrelation (Section 4.1.2), the use of L-band data to alleviate the temporal decorrelation effects was considered. The longer wavelength L-band data was expected to provide a decreased sensitivity to volume decorrelation effects due to the ability of the long wavelength data to penetrate through vegetation, thereby increasing the surface scattering contribution. However, as suggested in Section 4.2.1, the volume scattering contribution was not entirely minimised, since the sensitivity to baseline decorrelation effects appeared to be correlated with different phonological stages at the time of image capture.

To further explore the effect of land cover at the time of image capture, the evolution of the land surface and temporal baseline decorrelation effects, the average scene coherence of the PALSAR dInSAR pairs were correlated to the temporal baseline associated with each interferometric pair (Table 10). It is observed that a strong negative correlation between average scene coherence and temporal baseline effects is observed with FBS-FBS combinations providing the strongest correlation (ρ = -0.903). Although still a strong correlation (ρ = -0.688), the FBD-FBS pairs appear to have the lowest sensitivity to temporal decorrelation effects.

Table 10: The correlation between average scene coherence and temporal baseline.

	Temporal baseline
Average coherence FBS-FBS (N = 15)	-0.903
Average coherence FBD-FBD (N = 21)	-0.820
Average coherence FBS-FBD (N = 16)	-0.853
Average coherence FBD-FBS (N = 26)	-0.688

The different sensitivities of the different PALSAR pairs to temporal decorrelation effects are likely due to the characteristics of the land surface at the time of master image acquisition. Specifically, for C-band data it was demonstrated that the phenology of the vegetation at the time of master and slave image acquisition had a significant effect on the average scene coherence (Section 4.1.2, Figure 35). A similar observation is made when the coherence values for PALSAR interferometric pairs with 46-day temporal baselines are compared to the EVI values at the time of master and slave image acquisition (Figure 43). It is observed that pairs with either master or slave scenes captured during periods where the EVI is low resulted in higher average scene coherence compared to pairs created with master or slave scenes captured when the EVI is high.

When the frequency distribution of EVI values at the date of image acquisition for FBS and FBD polarisation scenes are considered (Figure 44), it is observed that FBS scenes were associated with high EVI values at the time of image capture whereas FBD scenes were associated with low EVI values at image acquisition. This suggests that pairs created with FBS scenes as either master or slave or both are more sensitive to volume decorrelation effects leading to incoherent changes in scattering elements (Section 3.1.5). Lower densities of vegetation at the time of image capture for FBD-FBD scenes are associated with a lower sensitivity to volume decorrelation (ρ = -0.820). However, the lowest sensitivity to volume decorrelation is exhibited by the FBD-FBS pairs (ρ = -0.688). This may be due to the increased sensitivity to baseline decorrelation exhibited by FBD-FBS pairs (Section 4.2.1).

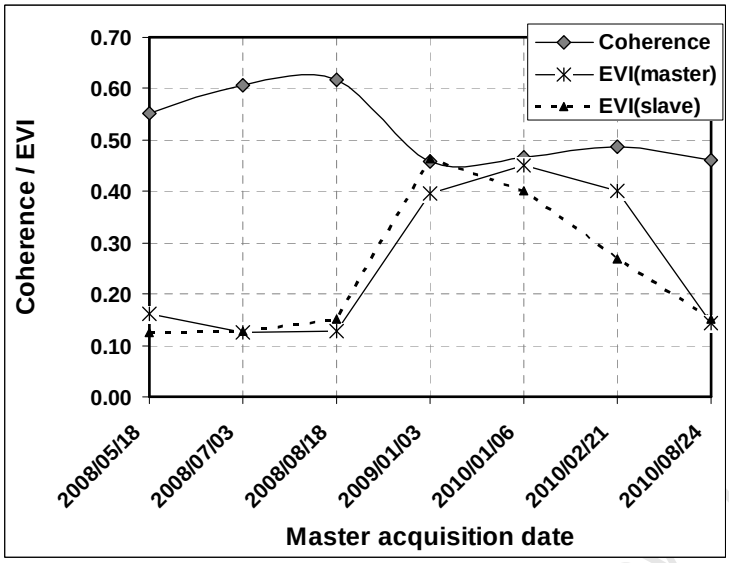

Figure 43: Average scene coherence for PALSAR pairs with 46-day temporal baselines compared to the EVI at the time of master and slave image capture.

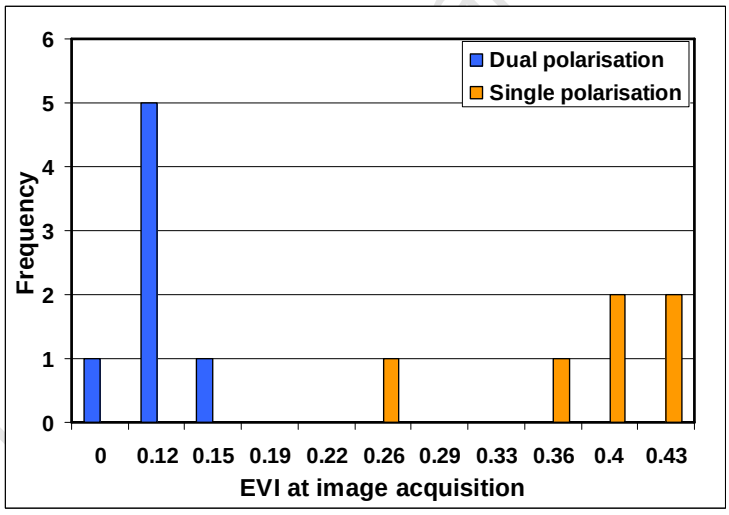

Figure 44: The EVI (as a proxy for vegetation density) at the time of single and dual polarisation image capture.

To investigate the effect of evolving land surface conditions of the average scene coherence, the correlation between average scene coherence and $|\delta \text{EVI}|$ was considered. The results suggest that a weak correlation between $|\delta \text{EVI}|$ and average scene coherence is observed (ρ = -0.166). This effect is illustrated graphically in Figure 45.

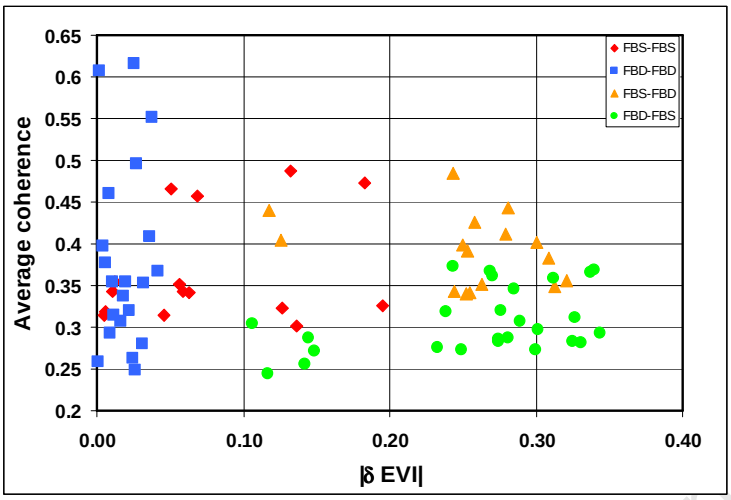

Figure 45: The effect of land surface evolution ($|\delta$ EVI|) on average scene coherence.

The very low sensitivity to the evolution of the land surface was expected since the longer wavelength L-band data was expected to increase the interaction of the surface, thereby minimising the effect of vegetation growth, planting and harvesting. However, practices such as tilling, planting and harvesting were expected to affect the roughness of the surface which creates the possibility of incoherent phase changes. However, since long wavelength data is used, the fields are likely to appear smooth, an effect that will be considered in Section 4.4.1.

4.2.3 The effect of polarisation

Since the number of fully polarimetric PALSAR scenes are limited to only 3 scenes, accurate conclusions regarding the effect of polarisation on PALSAR scenes can not be investigated. However, if the average scene coherence for the HH, HV and VV polarisation data is considered (Table 11, Table 12 and Table 13 respectively), it is observed that the average scene coherence of pairs processed in VV polarisation is higher than for the HH polarisation pairs.

Table 11: Average scene coherence for PALSAR polarimetric data in HH polarisation.

	2008/10/27	2009/04/29	2009/10/30
2008/10/27			
2009/04/29	0.355		
2009/10/30	0.294	0.424	

Table 12: Average scene coherence for PALSAR polarimetric data in HV polarisation.

	2008/10/27	2009/04/29	2009/10/30
2008/10/27			
2009/04/29	0.193		
2009/10/30	0.182	0.223	

Table 13: Average scene coherence for PALSAR polarimetric data in VV polarisation.

	2008/10/27	2009/04/29	2009/10/30
2008/10/27			
2009/04/29	0.376		
2009/10/30	0.315	0.464	

The polarisation dependency of average scene coherence suggests that significant ground scattering contributions are contributing to the signal since, as described in Section 2.3.2, the coherence of pure volume scattering contributions is independent of polarisation whilst the coherence of ground scattering contributions is polarisation dependent.

4.3 X-BAND DATA

The TerraSAR-X data obtained for the study area covers a time span of more than 2 years with 21 scenes being acquired at three different acquisition modes. 4 scenes were captured at VV polarisation, 10 scenes at HH polarisation and 7 scenes in dual-polarisation (HH/VV). Only scenes acquired in the same acquisition mode could be used for interferometric processing. Since fully polarimetric data was not available for the area of interest, the influence of polarisation could only be investigated using the dual-pol acquisition pairs for HH and VV polarisations. All scenes could be used to consider the effect of perpendicular baseline, Doppler Centroid difference and the effect of land surface evolution. The frequency distribution of the perpendicular baselines, Doppler centroid difference, temporal baseline and $|\delta \mathrm{EVI}|$ are presented in Figure 46 A, B, C and D respectively.

To simplify the statistical analysis of interferometric coherence with the various parameters affecting the coherence, the global average coherence for each interferometric pair was used. To confirm that global coherence for each pair was representative for different land cover types as well, the average coherence for each crop type was extracted for a subset of interferometric pairs. Similar to the observation for RADARSAT-2 and PALSAR data, the global average coherence for each TerraSAR-X

interferometric pair indicated a strong positive correlation with the average coherence calculated for each crop type. This is illustrated in Figure 47 for a subset of interferometric pairs. Consequently, only the global average coherence for each interferometric pair was considered for further analysis. The frequency distributions of average scene coherence values are presented in Figure 48. Section 4.3.1 to 4.3.2 presents the results of the analysis of the sensitivity of average scene coherence to temporal and geometric decorrelation effects.

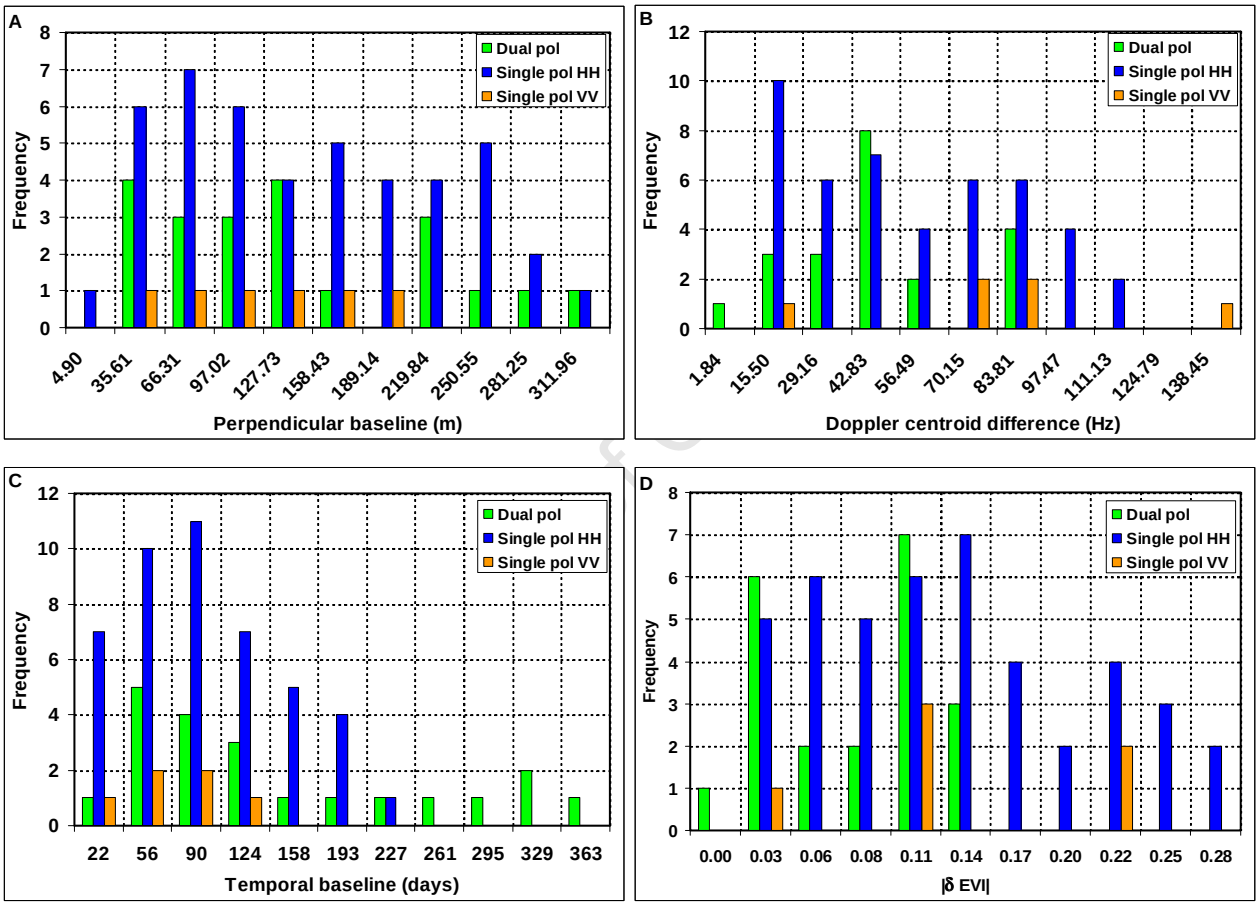

Figure 46: The frequency distribution of parameters affecting scene coherence for TerraSAR-X Dual polarisation and Single polarisation HH and VV datasets.

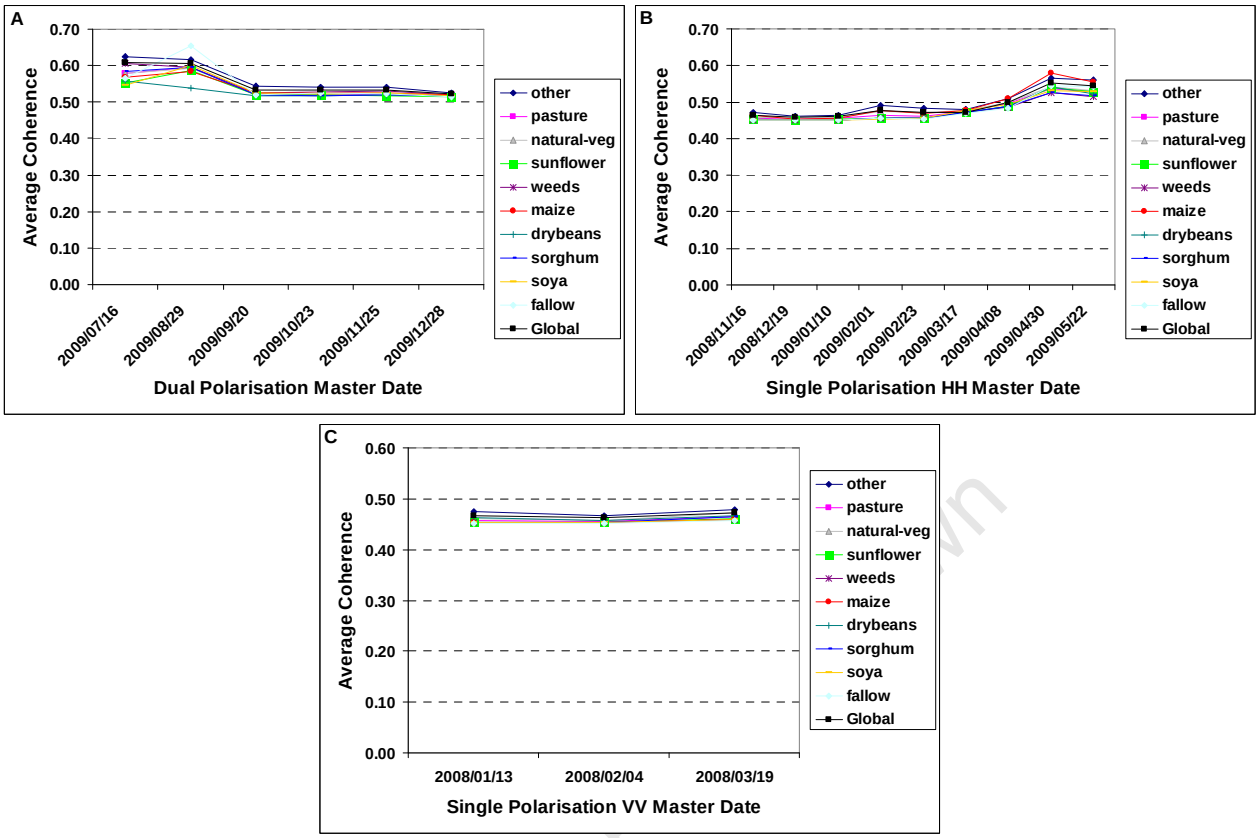

Figure 47: The average coherence per land cover category compared to the global average scene coherence.

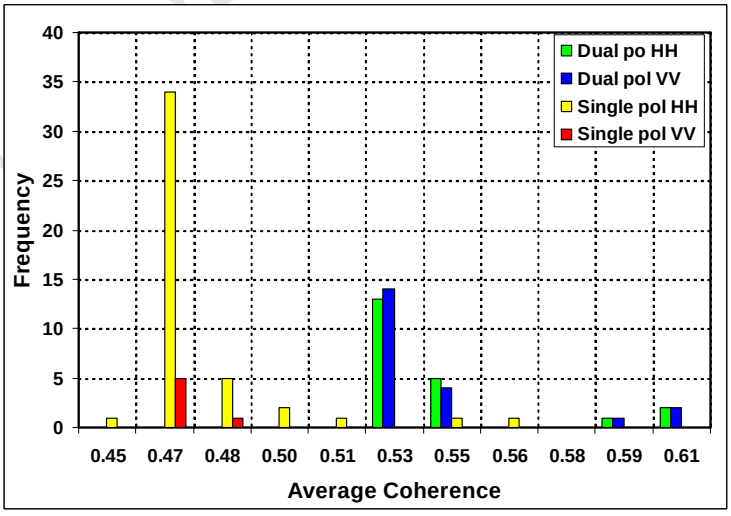

Figure 48: The frequency distribution of average scene coherence values for TerraSAR-X Dual polarisation HH and VV interferograms, as well as single polarisation HH and VV interferograms.

4.3.1 The effect of perpendicular baseline and Doppler centroid difference

When the influence of Doppler centroid difference and B_{perp} of the TerraSAR-X scenes are considered, it is observed that the critical baseline for single polarisation VV and HH data was ~ 6063 m and critical Doppler was 3716 Hz. The critical baseline for dual polarisation data was slightly higher at ~ 6205 m whilst the critical Doppler was lower at ~ 2945 Hz. The observed B_{perp} and Doppler centroid differences were 5.08 and 4.16 % of the critical values. Not surprisingly, a correlation between average scene coherence and perpendicular baseline and Doppler centroid difference (Figure 49 and Figure 50 respectively) was absent. For similar B_{perp} and DC difference values however, the HH and VV polarisation scenes captured in Dual Polarisation mode exhibited higher average scene coherence values than the single polarisation HH and single polarisation VV scenes respectively. This observation will be explored further in Section 4.3.3 and Section 4.3.2.

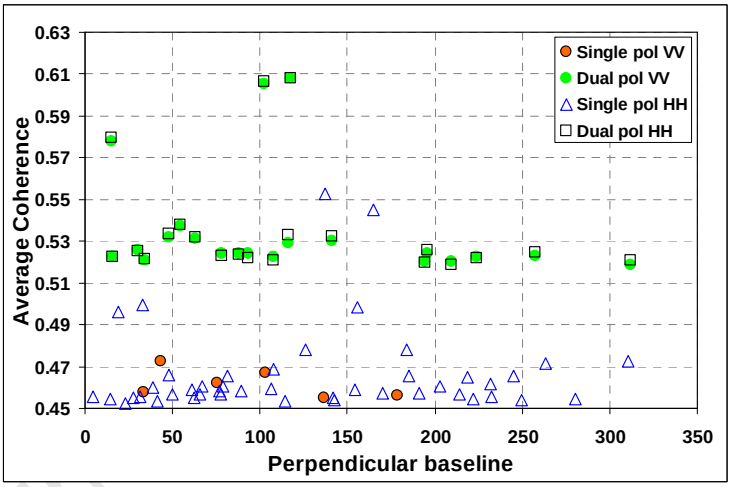

Figure 49: The effect of perpendicular baseline on average scene coherence.

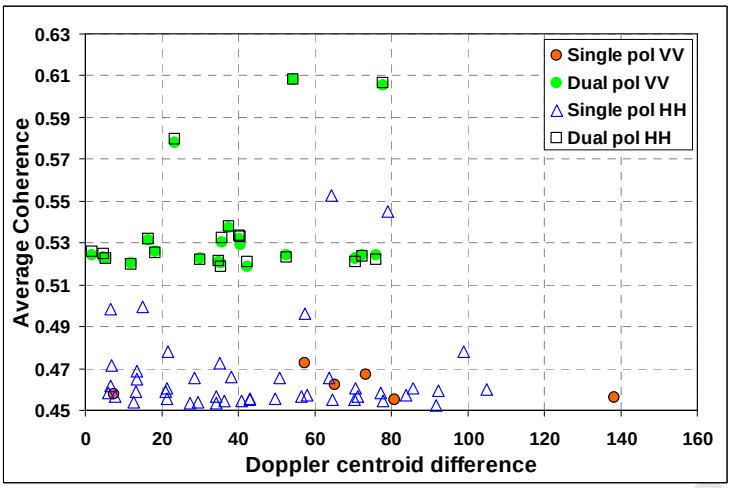

Figure 50: The effect of Doppler centroid difference on average scene coherence.

The short wavelength TerraSAR-X data is expected to exhibit significant volume scattering contributions and consequently, a high sensitivity to baseline decorrelation is expected. However, if the frequency distribution of the B_{perp} as a percentage of the critical baseline is considered (Figure 51), it is observed that the baseline of none of the interferometric pairs exceeds 5 % of the critical baseline. With such low perpendicular baselines, the low sensitivity to geometric decorrelation effects induced by perpendicular baselines is expected.

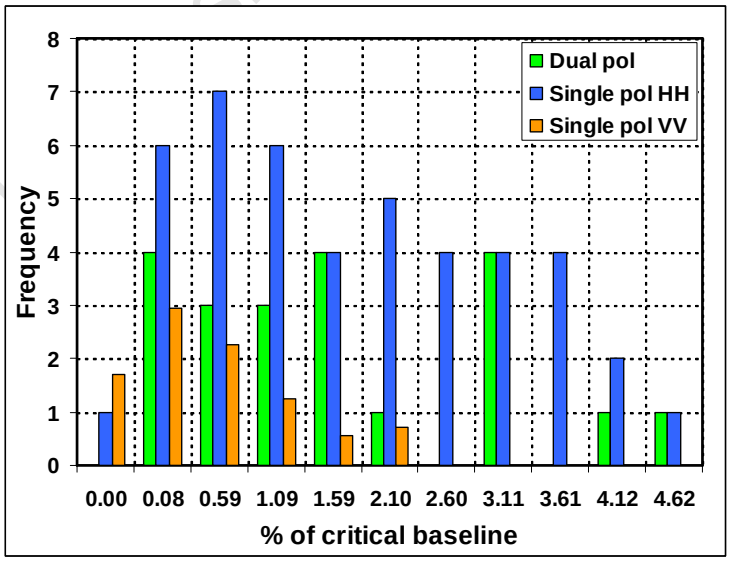

Figure 51: The perpendicular baseline of the TerraSAR-X interferometric pairs as a percentage of the critical baseline.

4.3.2 The effect of temporal baseline and land surface evolution

When temporal decorrelation effects on the TerraSAR-X average scene coherence is considered, an intermediate negative correlation between temporal baseline and average scene coherence is observed (Table 14). Similarly, an intermediate negative correlation between average scene coherence and $|\delta \text{EVI}|$ as a proxy for land surface evolution is observed. It should be noted that, since only 6 interferometric pairs in single polarisation VV mode were available, the correlation coefficients were not calculated. When graphically illustrated (Figure 52), a saturating dependency is suggested between average scene coherence and temporal baseline with minimal additional decreases in average coherence at temporal baselines higher than 150 days. It is also observed that dual polarisation pairs exhibit higher average scene coherence values compared to the single polarisation HH and VV pairs.

As observed for PALSAR (Section 4.2.2) and RADARSAT-2 (Section 4.1.2) data, the EVI at the time of Master and Slave image acquisition has a significant impact on average scene coherence. When considered in isolation, dual polarisation HH and VV coherence values do not exhibit a significant dependency on EVI of master and slave image acquisition (ρ = -0.292 and -0.309 respectively for the EVI at master image acquisition and ρ = -0.298 and -0.319 respectively for the EVI at slave image acquisition). When the frequency distributions of the EVI at master image acquisition of TerraSAR-X interferometric pairs are considered (Figure 54), it is observed that the majority of Dual polarisation scenes were captured during a time when EVI was low. The lower densities of vegetation at dual pair image acquisition are therefore attributed to the higher average scene coherence values observed for dual polarisation interferometric pairs. In contrast, a strong correlation between EVI at master image capture and coherence is observed for single polarisation HH data (ρ = -0.693). The stronger correlation between single polarisation HH coherence and the EVI at master image acquisition is due to a larger number of single polarisation HH master scenes captured at a time when EVI was high (Figure 54). This suggests that an increase in volume decorrelation is responsible for the decrease in coherence. In contrast, the coherences of single polarisation HH interferometric pairs indicate a low sensitivity to the EVI at slave image acquisition. This is due to the fact that the majority of slave scenes were captured when the EVI was low, resulting in an apparent decrease in sensitivity to the EVI at slave image acquisition.

Table 14: The correlation between temporal decorrelation effects (temporal baseline and land surface evolution) and average scene coherence for TerraSAR-X interferometric pairs (N is the number of pairs for each acquisition mode).

	Temporal baseline	$\lvert\delta$ EVI$\rvert$	EVI (master)	EVI (slave)
Dual HH (N = 21)	-0.449	-0.517	-0.292	-0.298
Dual VV (N = 21)	-0.424	-0.507	-0.309	-0.319
Single pol HH (N = 45)	-0.469	-0.490	-0.693	-0.259

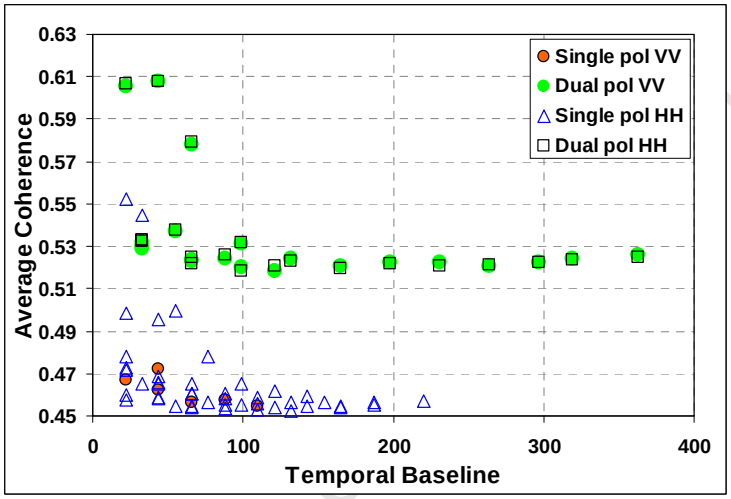

Figure 52: The effect of temporal baseline on average scene coherence.

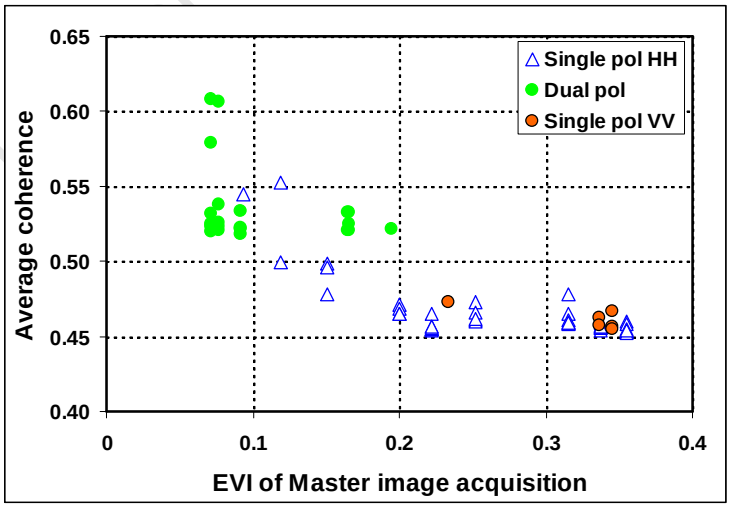

Figure 53: The average scene coherence as a function of the EVI of master image acquisition.

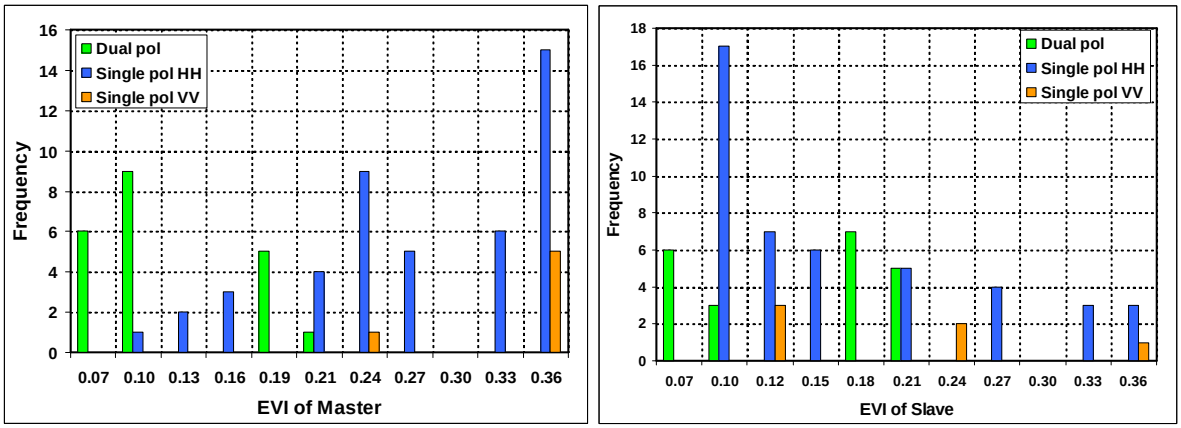

Figure 54: The frequency distribution of the EVI of the master and slave scenes for TerraSAR-X interferometric pairs.

The sensitivity of TerraSAR-X interferometric pairs to the effect of temporal baselines is surpassed by the sensitivity to the evolution of the land surface which as assessed by using $|\delta \mathrm{EVI}|$ as proxy. The high sensitivity of X-band data to temporal decorrelation effects including changes due to land surface evolution is expected since the short wavelength radiation is expected to interact predominantly with the smaller vegetation components such as twigs and leaves in the presence of vegetation. Therefore, agricultural activities such as planting, harvesting and tilling between image acquisitions would have a significant effect on interferometric coherence.

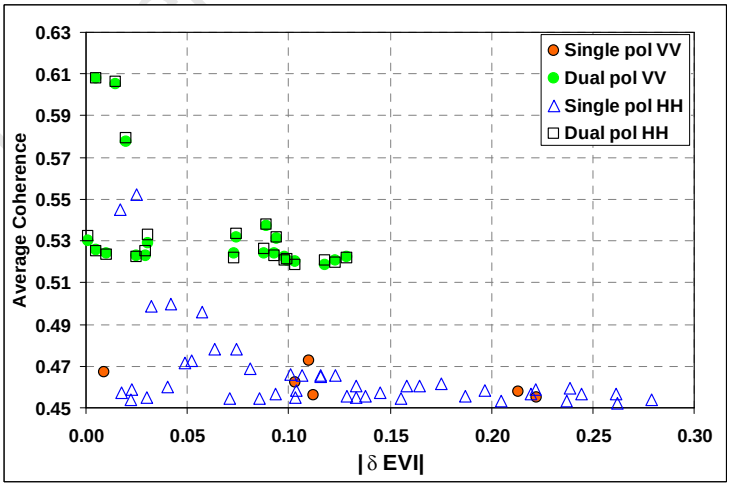

Figure 55: The effect of a change in land surface conditions on average scene coherence.

4.3.3 The effect of polarisation

To exclude effects of the variations in orbital parameters and temporal baseline, only the dual polarisation data was considered when analysing the effects of polarisation on average scene coherence. It was observed that there was virtually no difference in the average scene coherence observed for HH polarisation and VV polarisation data (ρ = 0.998) with the average difference between HH and VV coherence of 0.0012 (Figure 56). This result is expected since the short wavelength of TerraSAR-X data (~ 3 cm) will interact with smaller plant components (branches, twigs and leaves) irrespective of polarisation and, consequently, the backscatter will be returned from the highly dynamic components of plants which exhibits changes even after a short amount of time. As discussed in Section 2.3.2, the coherence produced by pure volume scattering contributions is independent of polarisation and the polarisation dependency increases as ground scattering contributions increases. This suggests that the very low sensitivity of average coherence to polarisation is due to the predominance of volume scattering contributions and the near absence of ground scattering contributions.

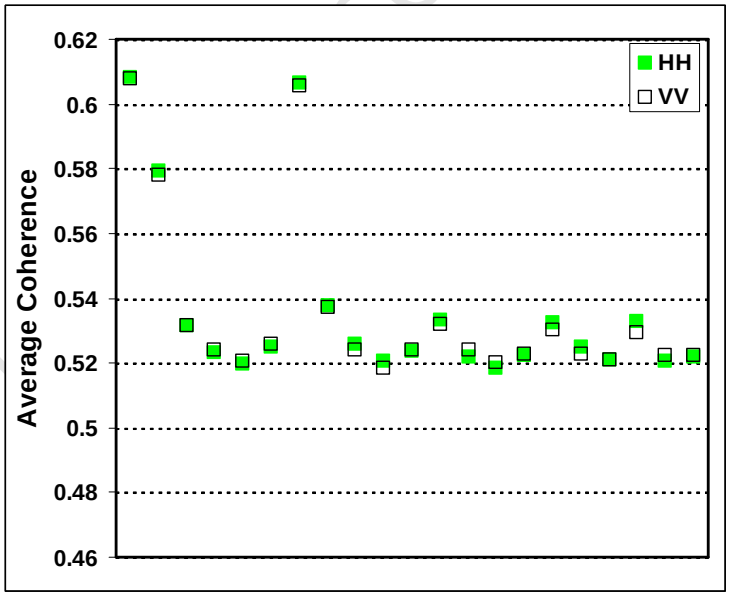

Figure 56: The effect of polarisation on average scene coherence.

4.4 ADVANCED INTERFEROMETRY: ANALYSIS OF SCATTERING MECHANISMS AND POLARIMETRIC INTERFEROMETRY

Traditional dInSAR techniques allows for the estimation of the height of a scatterer by examining the phase difference between two images and, with accurate information on height and orbital parameters, the change in height of a scatterer over time can be estimated. However, as described in Section 4.1.3, 4.2.2 and 4.3.2, the sensitivity of interferometric coherence to the presence of vegetation and the evolution of the land surface over time creates difficulties for the long term monitoring of specific areas. Generally, short temporal baseline data is needed to minimize the phase noise introduced by vegetation and evolving surface conditions. However, the systematic acquisition of SAR data for specific areas can be costly, especially when using sensors that do not have a systematic coverage of the entire globe and acquisitions have to be tasked. Additionally, scheduling conflicts frequently prevents the timely acquisition of datasets. In the absence of systematically acquired datasets over time at regular intervals, higher temporal baseline interferometric pairs are frequently the only alternative which becomes problematic for long-term monitoring if successful deformation measurement is not possible due to temporal decorrelation effects.

Advance dInSAR techniques discussed in Section 2.3 provide an opportunity to investigate ways to overcome the land cover evolution and temporal decorrelation effects thereby increasing the maximum temporal baseline requirements. However, the problem with the persistent scatterer and SBAS techniques is their reliance on a large number of stable pixels, which are generally not present in dynamic agricultural environments. Additionally, a large number of datasets are needed, especially for the PS technique, limiting its usefulness in terms of decreasing the number of scenes required for interferometric monitoring. For this reason, and due to limited number of available scenes for PALSAR and RADARSAT-2 data, these techniques were not considered further in this investigation.

The sensitivity of interferometric coherence and interferometric phase to the density and height of vegetation is well known (Papathanassiou et al. 2000a). Additionally, the quality of interferometric measurements and its dependence on the coherence between images have been described (Cloude & Papathanassiou 1997). To minimize the impact of vegetation and evolving land surface conditions on interferometric coherence, the fully polarimetric data was exploited. As described in Section 2.3.2, different polarisations of data interact differently to different scattering mechanisms and are dependent

on the shape, orientation and dielectric properties of the surface being observed. Although the strong dependency of interferometric coherence on polarisation has been previously described (Cloude & Papathanassiou 1998; Stebler et al. 2002), the results achieved in Section 4.1.3 show that the average scene coherence in HH and VV polarisation for shorter wavelength datasets varied only minimally. However, although HH polarisation was expected to be optimal for a study area dominated by vertical crops, the choice of polarisation was not straightforward and depended on the season during which the scenes were captured.

The interactions of the various scattering mechanisms with different polarisations implies that polarimetric image analysis can provide information on the dominant scattering mechanisms observed in a resolution cell (i.e. surface scattering from the ground or volume scattering from a vegetation canopy etc.). Consequently, time series analysis of fully polarimetric scenes can provide information on how the scattering processes evolve over time. The ability to identify different scattering mechanisms also introduces the potential to separate the phase contributions produced by the different mechanisms. In theory, it would be possible to define the scattering mechanism (scattering surface) that provides the highest possible interferometric coherence which is the aim of coherence optimization algorithms (Section 2.3.2). These algorithms essentially focus on maximizing the ground return in a pixel whilst minimizing the volume scattering contribution form vegetation canopies (Papathanassiou & Cloude 2001). The ideal is therefore to actually optimize the coherence based on the analysis of scattering mechanisms as opposed to merely selecting the polarisation providing the highest coherence as performed in Section 4.

The potential to optimize interferometric coherence even in the presence of evolving land surfaces and high vegetation densities is promising since, if successful, it will allow for the acquisition of SAR scenes with longer temporal baselines. This implies lower data costs whilst still enabling the long-term monitoring of surface deformation. The following sections show the results of polarimetric analysis of the fully polarimetric RADARSAT-2 data with the aim of identifying the dominant scattering mechanisms and how they evolve over time (Section 4.4.1). Additionally, the results of the application of the coherence optimization through polInSAR techniques are presented in Section 4.4.2.

4.4.1 The analysis of scattering mechanisms through SAR polarimetry

To exploit the ability of the fully polarimetric RADARSAT-2 data to provide an interpretation of the scattering mechanisms within the study area and how it evolves over time, the H-A-alpha decomposition and classification scheme was employed (Cloude & Pottier 1997). The technique relies on the calculation of three parameters: 1) polarimetric entropy (H), 2) polarimetric anisotropy (A), and 3) the alpha angle (α) (Cloude & Pottier 1997; European Space Agency 2012). Entropy (H) represents the randomness of the scattering contributions in a resolution cell with H = 0 indicating a single scattering mechanisms and H = 1 representing a random mixture of scattering mechanisms (European Space Agency 2012; Natural Resources Canada 2012). The α angle provides an indication of the dominant scattering mechanism with $\alpha = 0^0$ indicating single bounce surface scattering produced by a rough surface, $\alpha = 45^0$ indicates volume scattering and $\alpha = 90^0$ indicates dihedral reflector or multiple scattering (Natural Resources Canada 2012). The anisotropy parameter is complementary to the entropy and provides and additional source of information in a high Entropy scenario (European Space Agency 2012).

The co-occurrence of the H and α parameters can be used to determine the dominant scattering mechanism as illustrated in Figure 57. The H-α co-occurrence planes for each of the RADARSAT-2 scenes are presented in Figure 58. It is observed that, during the peak of the growing season and prior to harvesting (i.e. between 2011/01/26 and 2011/04/08) the highest density of data points (warmer colours) is concentrated in the medium entropy environment with dominant volume scattering taking place. However, surface and multiple scattering is also taking place suggesting that there is a backscatter contribution from the surface. Additionally, multiple interactions between the surface and the stems of vegetation are also taking place.

The soya and sunflowers that are cultivated in the area usually ripen towards the end of March/ beginning of April at which time the plant leaves disintegrate significantly lowering the leaf area index and vegetation biomass. On the other hand, when maize ripens, the leaves do not disintegrate and will retain its biomass, even when completely dry. This implies that, even when unproductive, the radar signal will interact with the maize biomass until the crop is harvested. The disintegration of soya and sunflower plants leads to a decrease in the volume scattering contribution as exhibited in the 2011/05/02 H-α co-occurrence plane. However, it is only after harvesting of maize (usually in June)

that the dominating scattering mechanism changes from predominantly volume scattering mechanisms to predominantly surface scattering mechanisms (visible in the 2011/08/06 to 2011/08/30 H-α co-occurrence planes).

During 2011/08/06 and 2011/08/30, the scattering mechanisms are dominated by both low and medium entropy surface scattering mechanisms. The low entropy surface scattering mechanisms are indicative of relatively smooth surfaces such as soya and sunflower fields after harvesting. The harvesting of maize however causes leaves, stalks and other debris to be scattered throughout the fields (significant amount off crop residue) which leads to a significant contribution of medium entropy scattering mechanisms (surface roughness propagation effects). The medium entropy surface scattering mechanisms are associated with rough surfaces and potential propagation through plant canopies.

The medium entropy scattering mechanisms dominates during 2011/09/23 and 2011/10/17 although these periods are associated with a slight increase volume scattering mechanisms. The period between the start of October until the end of November is associated with the planting of sunflowers, soya and maize. These periods are associated with a steady increase in volume scattering mechanisms and a medium entropy environment as indicated on the H-α co-occurrence planes between 2011/10/17 until 2011/12/28.

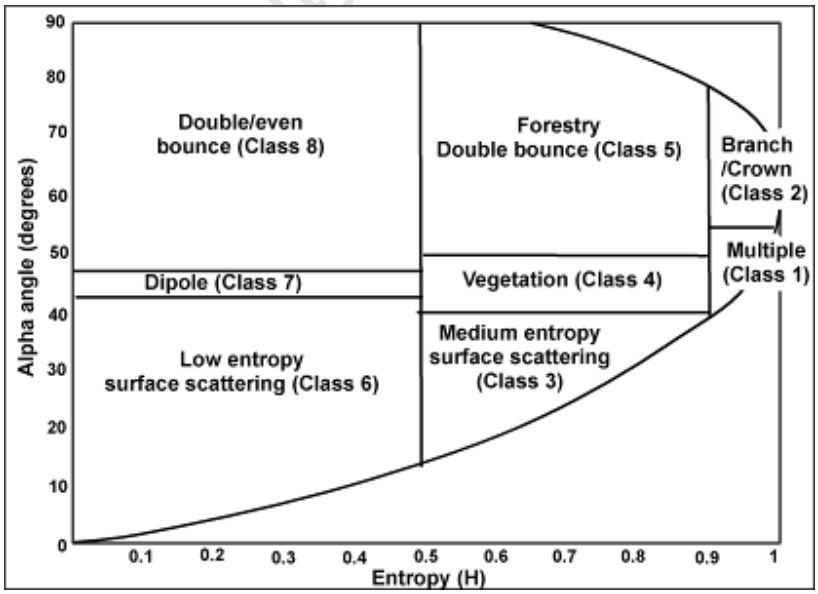

Figure 57: The interpretation of scattering mechanisms based on the H-α co-occurrence plane (adapted from (Cloude & Pottier 1997)).

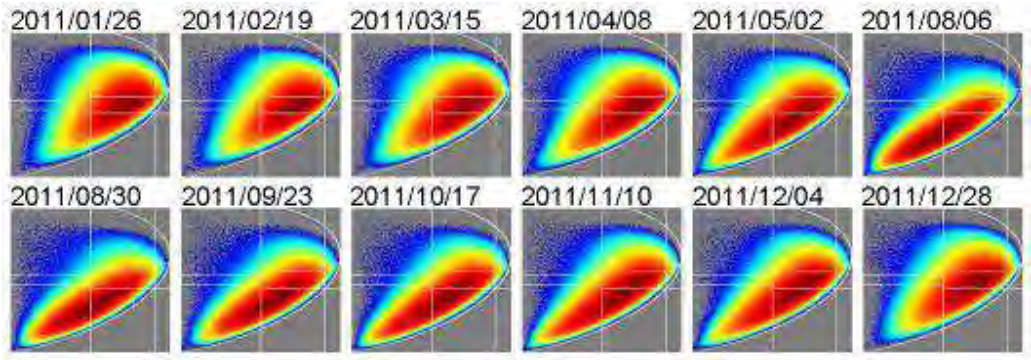

Figure 58: The H-α co-occurrence planes calculated for each RADARSAT-2 scene indicating the dominant scattering mechanisms at the time of image capture.

The consideration of the Anisotropy (A) parameter provides another dimension for the interpretation of the surface. The interpretation/classification of surfaces in the H-A co-occurrence plane is presented in Figure 59 (Natural Resources Canada 2012). The H-A co-occurrence planes for the RADARSAT-2 scenes is presented in Figure 60. The results suggest that the highest concentration of data points coincides with the medium entropy, high anisotropy environment which is indicative of rough, 1-dimensional surfaces. However, for the 2011/08/06 scene, the H-A co-occurrence plane exhibits an increase in the number of points is the medium-to-low entropy environment, indicative of smoother surfaces. This is associated with the period after the ripening of soya and sunflowers and their harvesting. A systematic increase in entropy associated with the scenes captured between 2011/10/17 and 2011/12/28 is indicative of regrowth of crops after planting between the beginning October 2011 and November 2011.

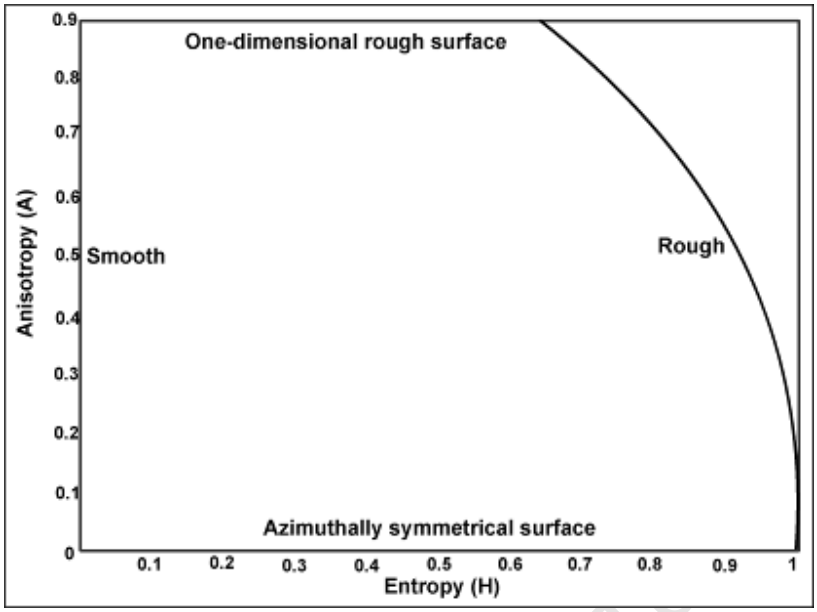

Figure 59: The interpretation of scattering mechanism based on the Entropy (H) and Anisotropy (A) co-occurrence plane.

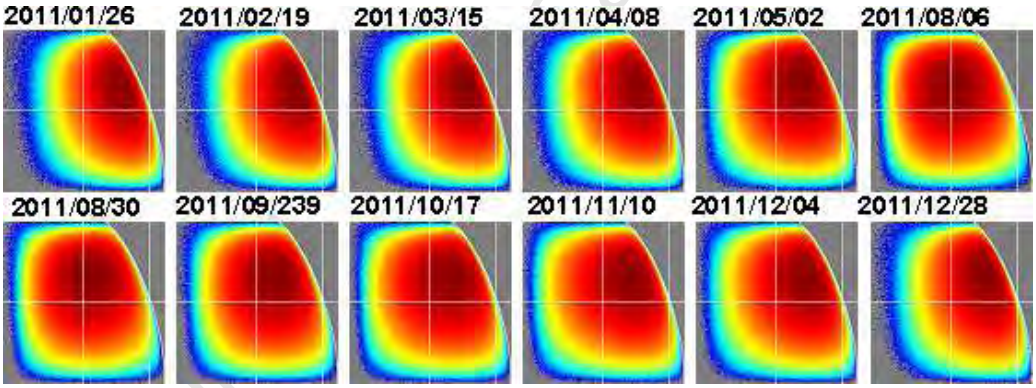

Figure 60: The Entropy (H) Anisotropy (A) co-occurrence planes for the RADARSAT-2 scenes.

Based on the H-A-alpha decomposition, each RADARSAT-2 scene could be classified based on the dominant scattering mechanisms present in the scene. The classification scheme identifies 8 possible classes as depicted in Figure 57. The total area dominated by each scattering mechanism was calculated for each scene as depicted in Figure 61. The results indicate that, similar to what was observed in the EVI data (Figure 19), during the peak of the growing season from 2011/01/26 to 2011/03/15; the dominant scattering mechanism is volume scattering mechanisms although surface roughness effects

are also prominent. During the same time, the contribution of low entropy surface scattering (Bragg surface scattering) is low.

A systematic increase in Bragg surface scattering is observed during and after harvesting between 2011/04/08 and 2011/08/06 where surface scattering is at a maximum. The increase in surface scattering is concurrent with a decrease in volume scattering from vegetation. After 2011/08/06, tilling and planting activities are associated with a systematic decrease in low entropy surface scattering and an increase in surface roughness effects as well as a systematic increase in volume scattering mechanisms. It is observed that, with the exception of the period between 2011/08/06 and 2011/08/30, surface scattering in the medium entropy environment (surface roughness propagation effects) dominate over low entropy surface scattering (Bragg surface scattering). This implies that, for the most part, agricultural fields appear rough at C-band except for a window between 2011/05/02 and 2011/09/23 during which time fields appear smooth. It is also observed that the scattering mechanisms associated with a cloud of anisotropic needles, branch/crown structures, forestry/double bounce effects, dipole and dihedral scatterers are under presented in the scene and covers < 5% of the study area irrespective of the time of year.

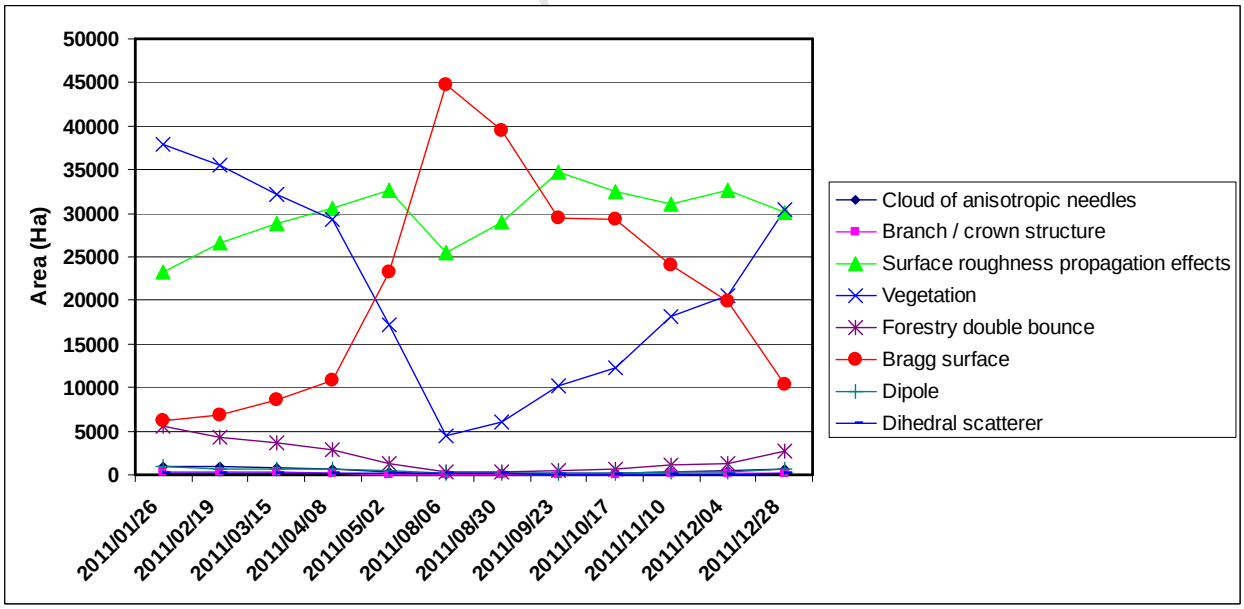

Figure 61: The total area dominated by various scattering mechanisms as calculated for each RADARSAT-2 scene.

The scattering mechanisms for longer wavelength PALSAR data is expected to be dominated by surface scattering mechanisms independent of the time of year since, in theory, the longer wavelength radiation penetrates through vegetation maximising interaction with the surface. This is confirmed when the H-A-alpha decomposition and subsequent classification of the three PALSAR fully polarimetric datasets are performed. The total area for each class of scattering mechanism was calculated and is presented in Figure 62. Similar to RADARSAT-2 data, the "cloud of anisotropic needles", "Forestry/Double bounce", "Dipole" and "Dihedral" scattering mechanisms are not present in the scene in significant quantities. However, unlike the RADARSAT-2 data, the PALSAR scenes are dominated by low entropy (Bragg) surface scattering mechanisms. The volume scattering contribution is low, even for the scene captured on 2009/10/30, a period during which the EVI data (Section 3.1.5) suggests that the vegetation density is high. Similarly, the low entropy surface scattering dominates during 2009/04/29, a timeframe generally associated with a period after harvesting of soya and sunflowers, as well as maize if it is used for fodder. The lack of surface roughness propagation effects suggests that the agricultural fields will appear smooth at L-band, irrespective of the time of year.

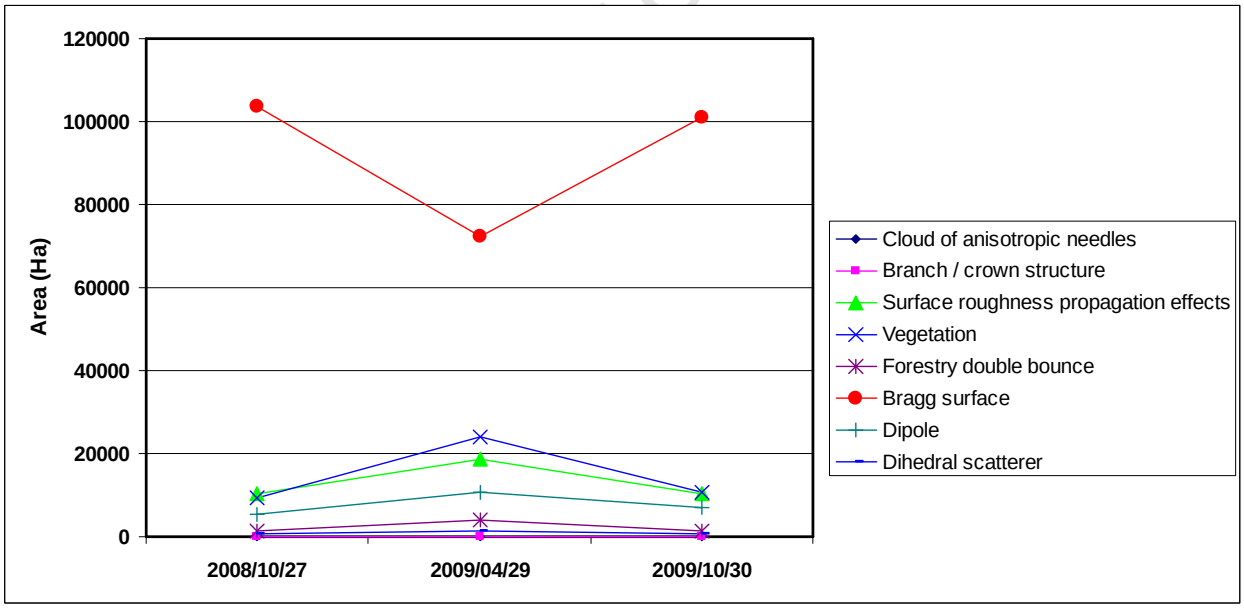

Figure 62: The total area of the scene covered by each scattering mechanism for PALSAR data.

4.4.2 Coherence optimization and polInSAR results

The polInSAR technique for coherence optimisation enables the optimisation of the interferometric coherence by choosing the polarisation basis that provides the highest possible coherence as described in Section 2.3.2. To determine if coherence optimisation algorithms can be used to decrease the phase noise components of the interferograms and, consequently, lengthen the maximum temporal baseline requirements, the coherence optimisation algorithm was applied to the RADARSAT-2 and PALSAR interferometric pairs. Since the dominant scattering mechanisms are highly variable over time (Section 4.4.1), similar polarimetric behaviour over time cannot be assumed and the polarimetric coherency matrices cannot be assumed to be equal. Therefore the equal scattering mechanisms (ESM) optimisation approach (Section 2.3.2) could not be used. The technique adopted in this investigation was the multiple scattering mechanism (MSM) approach (Section 2.3.2).

The result of the coherence optimization algorithm is 3 interferograms, representing high, medium, and low coherence products and their associated differential interferograms. The interferograms were constructed by identifying the dominant scattering mechanisms and separating those representing the highest coherence values from the scattering mechanisms exhibiting intermediate and low coherence values. The theoretical optimum coherence will have a value of 1, implying that only surface scattering mechanisms were present. However, an increase in volume scattering contributions is associated with a decrease in coherence and, consequently, coherence values < 1.

To compare the coherence optimisation (hereafter called polInSAR) results with the results obtained using traditional dInSAR techniques, the coherence values obtained for the different polarimetric channels processed using traditional dInSAR techniques were compared to the maximum, intermediate and low coherence data obtained by polInSAR. The frequency distribution of the average scene coherence for all polarisations and polInSAR coherence is presented in Figure 63. The results indicate a significant increase in average scene coherence for both the maximum and intermediate polInSAR coherence products compared to the dInSAR coherence in all polarisations. For all RADARSAT-2 and PALSAR datasets processed in this manner, the maximum coherence values obtained through coherence optimization techniques are significantly higher than the coherence values obtained through traditional dInSAR techniques.

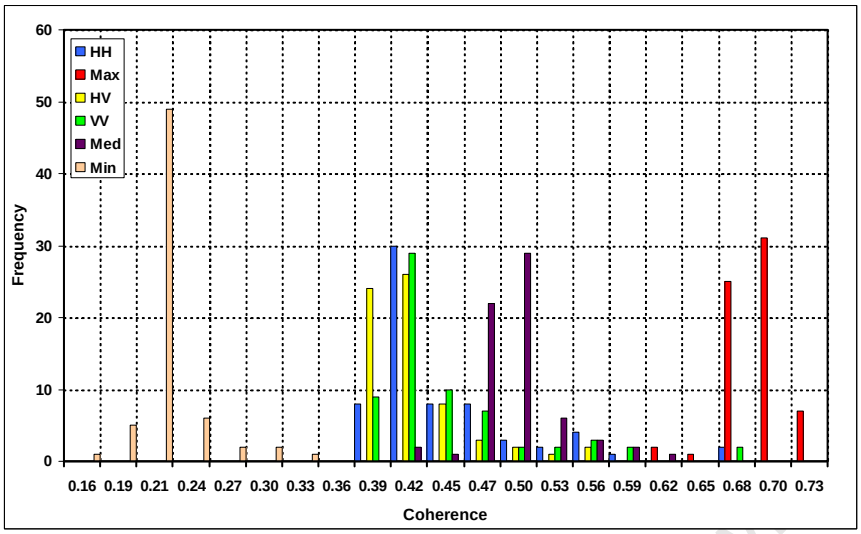

Figure 63: The RADARSAT-2 frequency distribution of average scene coherence values for dInSAR processing on HH, HV and VV polarisations and the maximum (Max), minimum (Min) and intermediate (Med) coherence optimisation results.

When comparing the average scene coherence achieved using polInSAR with the average scene coherence achieved using the traditional dInSAR techniques on the different polarisation channels (HH, VV and HV), correlation coefficients reveal a strong correlation between the coherence of traditional dInSAR (for HH, VV and HV polarisations) and polInSAR results for RADARSAT-2 data (Table 15). These results indicate that parameters affecting interferometric coherence using traditional dInSAR techniques will affect polInSAR results in a similar way. Table 15 also indicates the correlation between the polInSAR results (Max Cc, Med Cc and Min Cc) with perpendicular baseline (B_{perp}), Doppler centroid difference (Doppler), the change in land cover conditions (delta EVI) and temporal baseline (B_{temp}). The results reveals a slightly lower sensitivity to perpendicular baseline (p = -0.22 for Max Cc, p = -0.21 for Med Cc and p = -0.19 for Min Cc) when compared to the sensitivities achieved using traditional dInSAR techniques (p = -0.33 for HH Cc, p = -0.29 for HV Cc and p = -0.34 for VV Cc). Similarly, a decreased sensitivity to a change in land cover conditions as described by $|\delta \text{EVI}|$ is observed. An increase in temporal baseline was revealed to be the most significant factor with correlations of p = -0.65, p = -0.66, and p = -0.64 for Max Cc, Med Cc and Min Cc respectively being observed. Since only three PALSAR interferometric pairs were available, statistical correlations for the L-band data could not be drawn.

Table 15: The Pearson correlation coefficients of the coherence using dInSAR and coherence obtained using polInSAR for RADARSAT-2 data. Correlations with perpendicular baseline, Doppler difference, $|\delta \text{EVI}|$ and temporal baseline are also indicated.

	HH Cc	VV Cc	HV Cc	Max Cc	Med Cc	Min Cc	B_{perp}	Doppler	$\|\delta \text{EVI}\|$	B_{temp}
HH Cc		0.98	0.99	0.80	0.89	0.94	-0.33	0.07	-0.59	-0.67
VV Cc			0.99	0.78	0.89	0.95	-0.29	0.06	-0.54	-0.65
HV Cc				0.80	0.90	0.95	-0.34	0.07	-0.60	-0.65
Max Cc					0.98	0.93	-0.22	0.08	-0.51	-0.65
Med Cc						0.98	-0.21	0.07	-0.51	-0.66
Min Cc							-0.19	0.04	-0.50	-0.64

Interferometric measurement on a single pixel is not sensible since single pixels can incorporate phase noise in an unpredictable way (Section 2.2). The noise effects can cause pixels to undergo random phase changes which visually manifest as randomly coloured speckles in interferograms. The random nature of the phase noise component of the interferograms can be estimated by calculating the coefficient of variation (CV), of the coherence values for each interferometric pair. The CV is defined as $CV = \frac{\sigma}{\mu}$ (where σ is the standard deviation of coherence and μ is the average coherence). The CV provides a means to assess the degree of variation between data series even if the averages are drastically different. Lower CV values indicate more homogenous data (lower variance) whilst higher CV values indicate more heterogeneous data (higher variance). Subsets of 11 x 11 pixel interferograms are used to illustrate the effect of homogeneous and heterogeneous areas on interferograms with high and low average coherence.

Figure 64 shows interferograms over relatively homogeneous areas associated with high average coherence (top) as well as low average coherence (bottom). Additionally, interferograms created over heterogeneous areas (CV = 0.431 and 0.457 respectively) with high average coherence (top) and low average coherence (bottom) are shown in Figure 65. The results indicate that, in a more homogeneous area with a high average coherence, there is a better agreement between neighbouring pixels implying a higher confidence in interferometric measurements. However, if the area is homogeneous but the average coherence is low, phase noise remains problematic. Similarly, high average coherence in a heterogeneous region (top row of Figure 65) is associated with some speckle effects although to a

lesser extent than low average coherence in a homogeneous region (bottom row of Figure 64). The results demonstrate that high coherence values, although needed for reliable interferogram generation, is not the only requirement and that homogeneity of coherence over several pixels (estimated here by coefficient of variation) is needed for high quality interferogram generation.

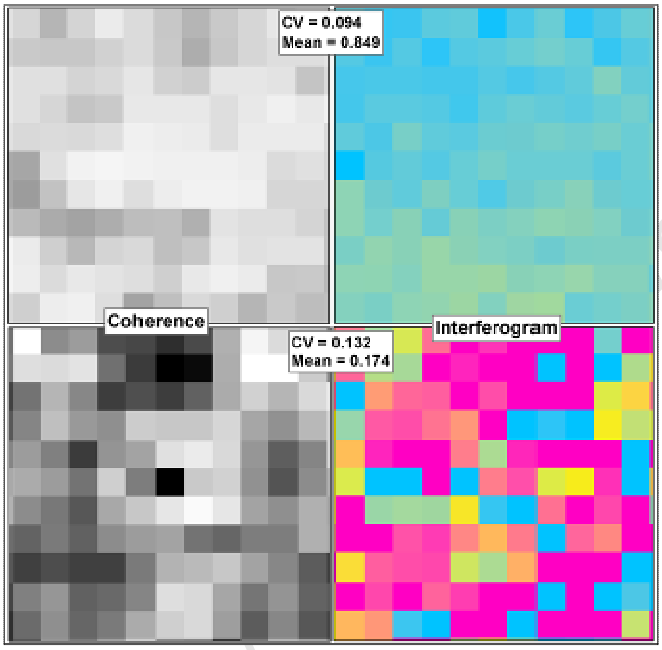

Figure 64: The interferograms over homogeneous areas (low CV) and high average scene coherence (top row) vs. interferograms over homogeneous areas with a low average scene coherence (bottom row).

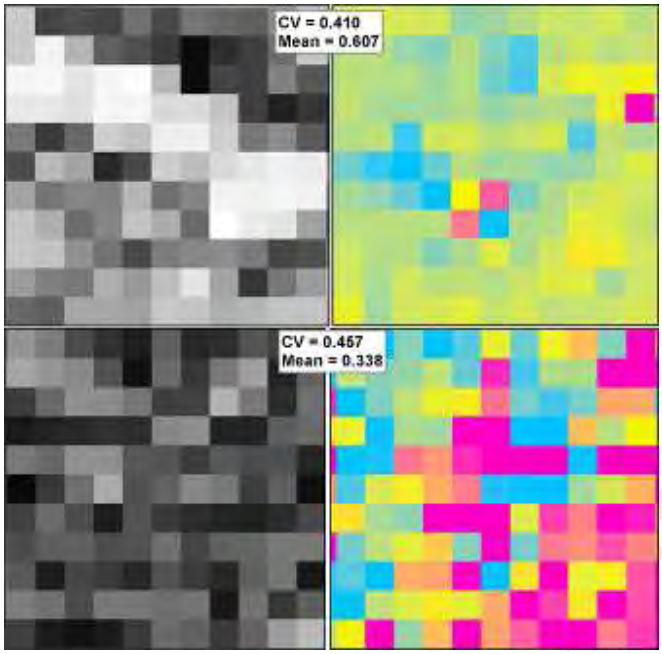

Figure 65: The interferograms over heterogeneous areas (high CV) and high average scene coherence (top row) vs. interferograms over heterogeneous areas with a low average scene coherence (bottom row).

The coefficient of variation of coherence values were calculated for each interferometric pair (in HH, HV and VV polarisation) for RADARSAT-2 data as well as the maximum coherence result of the coherence optimization algorithm (Figure 66). The results indicate that a consistently higher CV of coherence is achieved after coherence optimization is applied compared to a lower CV achieved prior to coherence optimization. This suggests that, although average coherence values may be higher after polInSAR, the phase noise manifested by random phase changes is not minimised using polInSAR on C-band data and, consequently, the phase agreement between neighbouring pixels that is needed for successful deformation measurement is not met.

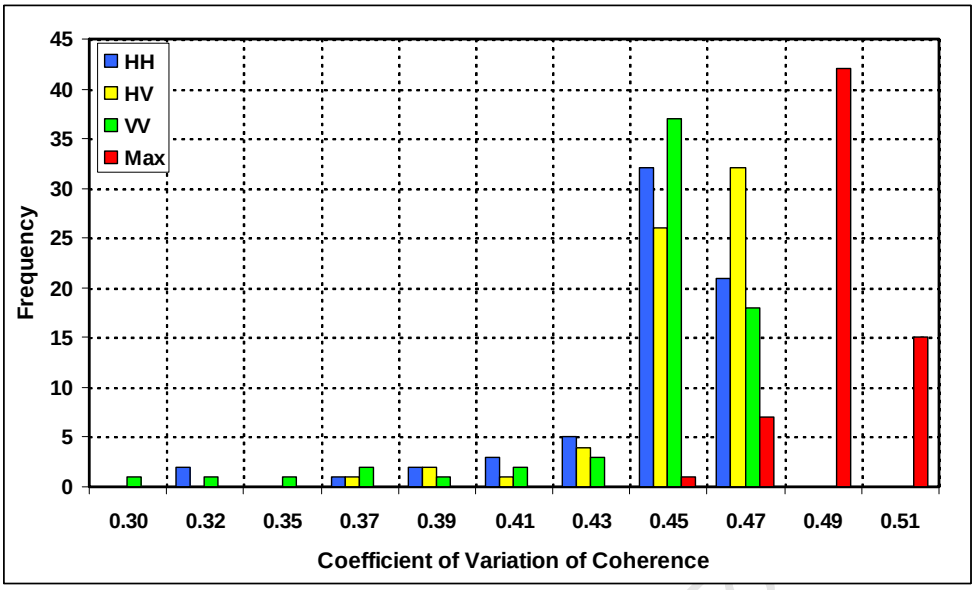

Figure 66: The coefficient of variation (CV) of coherence values calculated for HH, HV and VV polarisation processed using dInSAR techniques and the maximum coherence result of polInSAR (max) for RADARSAT-2 data.

Only three fully polarimetric PALSAR scenes were available for analysis which makes statistical interpretation of coherence optimization results impossible. However, for L-band data a significant decrease in CV of coherence is observed for the coherence optimized data. However, a higher temporal baseline dependency is suggested with the CV of the longer temporal baseline dataset exhibiting a 10% increase in the CV of coherence compared to traditional dInSAR results for which the CV of coherence increases by only 1.5 %. If the trend continues, the CV of coherence for coherence optimised data will continue to increase with temporal baseline, increasing the spatial heterogeneity of the coherence data. An increase in the spatial heterogeneity of the phase noise in L-band data will make successful interferogram interpretation impossible for long temporal baseline datasets even after coherence optimisation algorithms have been applied.

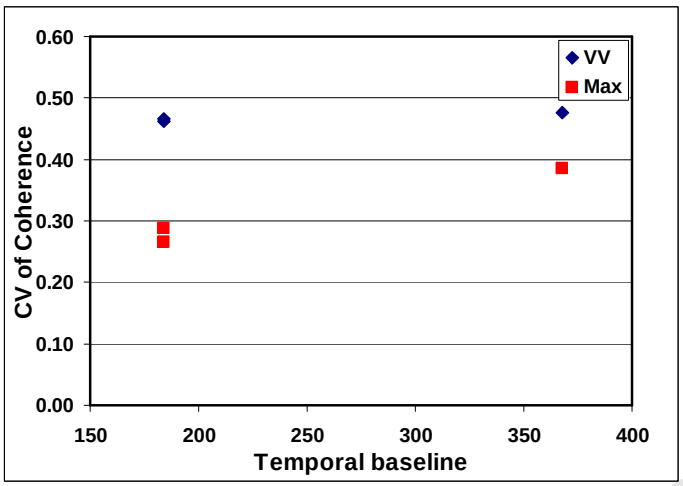

Figure 67: The coefficient of variation (CV) of coherence values calculated of VV polarisation data and the optimum coherence result of the coherence optimization algorithm for PALSAR data.

The spatial heterogeneity of the phase noise contributions as described by means of the coefficient of variation is visually confirmed by comparing the differential interferograms generated by traditional dInSAR and coherence optimisation techniques. The RADARSAT-2 interferograms generated for the master-slave pairs 2011/01/26 - 2011/02/19 and 2011/01/26 - 2011/03/15 are displayed in Figure 68 where the HH, VV and HV interferograms generated by traditional dInSAR techniques are displayed alongside the max (maximum coherence), med (intermediate coherence) and min (minimum coherence) interferograms generated by polInSAR. In general, noisy areas in interferograms generated through dInSAR techniques remain noisy on the interferograms generated through polInSAR techniques.

Figure 69 shows interferograms generated for master-slave pairs 2011/03/15-2011/04/08. Although the coherence optimized interferograms for the period 2011/03/15-2011/04/08 reveals fringes on the edges of the subsidence basins, the interferograms remain noisy and the extraction of deformation measurements would not be possible. The same observation is made when the coherence optimisation algorithm is applied to PALSAR data (Figure 70). The comparison between polInSAR results and the results obtained using dInSAR techniques reveals that there is no observable improvement in the interferograms generated using polInSAR. The results suggest that, although coherence optimization techniques results in a statistically significant increase in coherence, especially in the maximum

coherence results, the apparent decrease in phase noise is not translated to the interferograms generated using the coherence optimization technique.

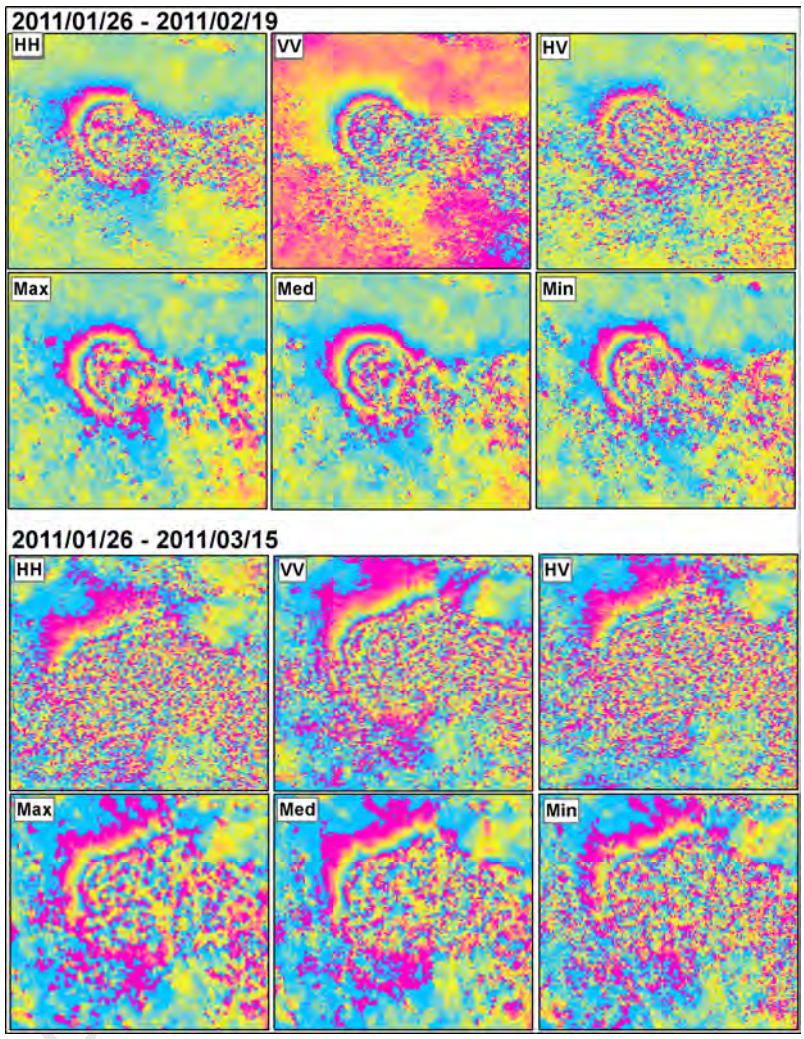

Figure 68: Comparison of RADARSAT-2 dInSAR interferograms (top row HH,VV and HV) and coherence optimized interferograms (bottom row max, med and min) for interferometric pairs 2011/01/26-2011/02/19 and 2011/01/26-2011/03/15 respectively.

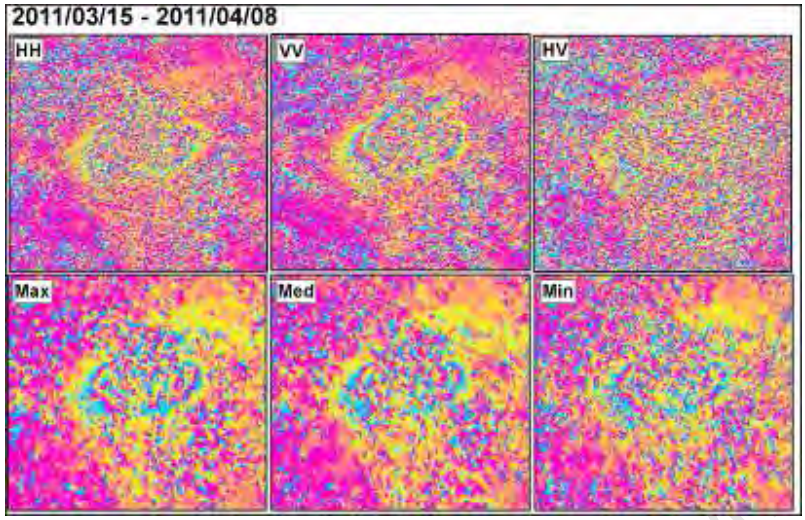

Figure 69: Comparison of RADARSAT-2 dInSAR interferograms (top row HH,VV and HV) and coherence optimized interferograms (bottom row max, med and min) for interferometric pair 2011/03/15-2011/04/08.

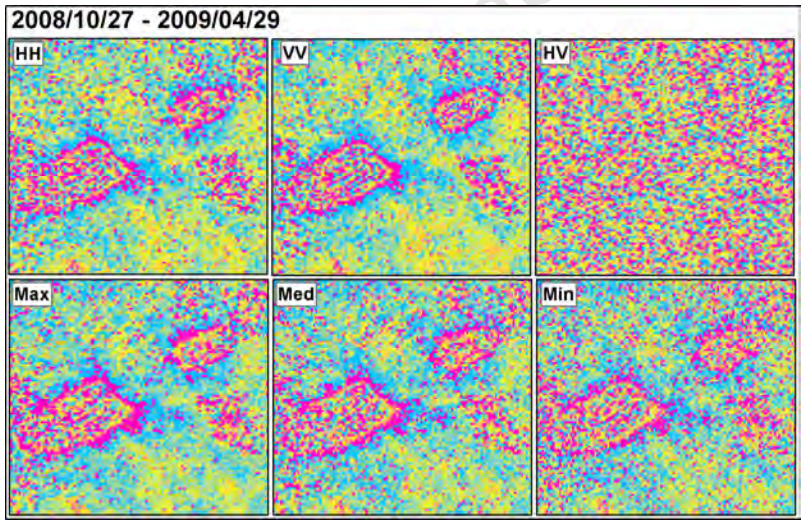

Figure 70: Comparison of PALSAR dInSAR interferograms (top row HH,VV and HV) and coherence optimized interferograms (bottom row max, med and min) for interferometric pairs 2008/10/27-2009/04/29.

5 DEFORMATION MEASUREMENT RESULTS

The various temporal and geometric decorrelation effects, investigated in Section 4, influence the ability to successfully derive deformation measurements. The differential interferograms produced during the processing sequence described in Section 3.2 are, in theory, datasets in which topographic and orbital phase contributions are removed. Any residual phase contributions are only due to surface deformation and possibly atmospheric artefacts. However, on inspection of differential interferograms, some residual topographic contributions remained present due to errors in the external DEM used to estimate and remove the topographic phase contributions. Residual topographic phase could be recognised due to the fact that they were present in all differential interferograms created using the same DEM. Additionally, since the sensitivity of interferograms to topographic phase is dependent on the perpendicular baseline, higher perpendicular baselines being more sensitive to topographic phase contributions exhibited a denser fringe frequency when compared to small perpendicular baseline interferograms. This effect is illustrated in Figure 71 for three TerraSAR-X differential interferograms.

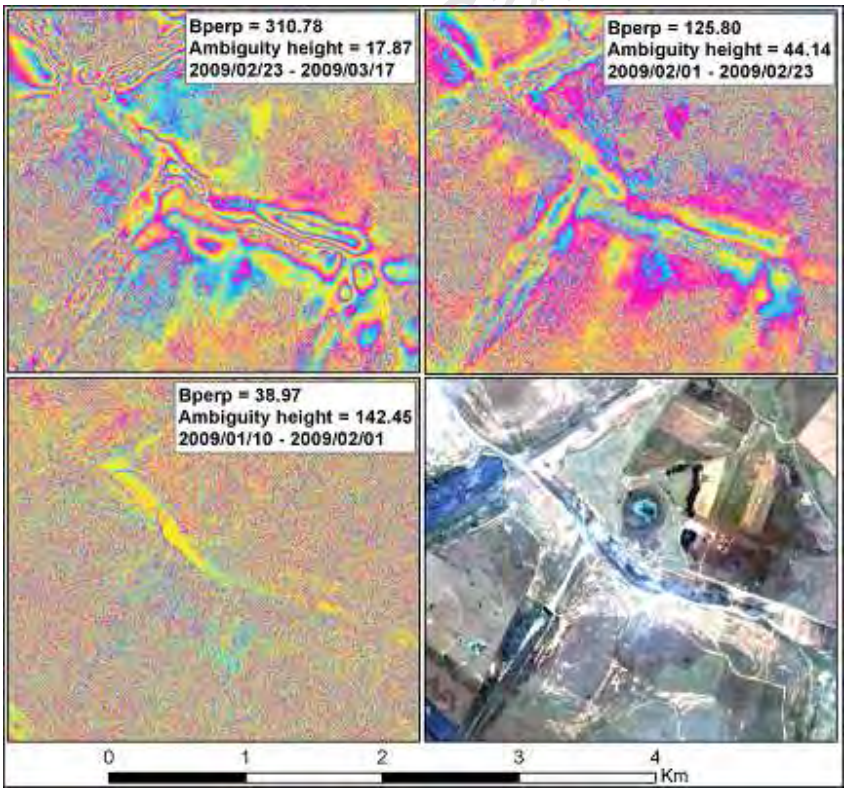

Figure 71: The effect of perpendicular baseline and ambiguity height on residual topographic phase for TerraSAR-X single polarisation HH scenes.

An additional source of topographic phase was introduced due to the agricultural nature of the study area. This residual topographic phase frequently matched the geometry of agricultural fields and manifested itself as either subsidence or uplift. An example of this phenomenon is provided in Figure 72 for an ERS-2 differential interferogram with master/slave image acquisitions on 1996/12/21 and 1997/01/25 respectively. The VV polarisation used to create the interferograms has the tendency to interact with the stalks of vertical crops implying that the scattering centre may be situated above the ground surface with backscatter originating from the stalks of the crops, thereby introducing a topographic phase contribution. However, the phase change exhibited in this agricultural field is a coherent change across the entire agricultural field. Therefore the change could also be due to the expansion of soils when wet and subsequent contraction when the field dried out.

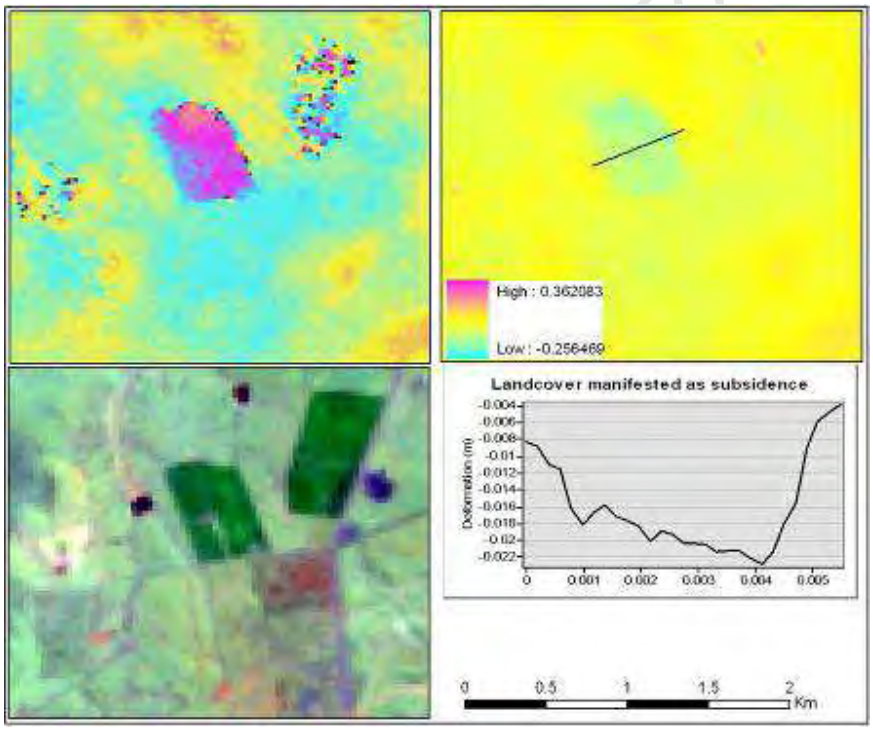

Figure 72: Residual topographic phase due to land surface characteristic.

Despite some false positive results produced by land cover and residual topographic phase, confirmed subsidence due to longwall mining activities was detected. The time series of RADARSAT-2 scenes proved to be successful in detecting surface subsidence basins in the study area. Additionally, the evolution of the subsidence basins as the working face of the mine advanced could be detected.

Figure 73 presents the time series of differential interferograms created for the area of interest. The first time series created with scene 2011/01/26 indicates that, with a 24 day temporal baseline, the deformation related interferometric fringes are visible despite some noise due to the presence of vegetation being visible. After 48 days however, the noise affects the scene in a more prominent way with deformation fringes only being visible on the edge of the subsidence basin. For temporal baselines of longer than 48 days, all interferometric fringes disappear and the scenes are dominated by noise as is evident in the interferogram presented by the third interferogram in the series (master-slave = 2011/01/26-2011/04/08).

The effect of temporal baseline worsens when the time series created using 2011/02/18 and 2011/03/15 is considered. Successful interferogram generation was only possible for the 24 day temporal baseline using 2011/02/18 as master image whilst with the 2011/03/15 scene as master, successful interferogram creation was not possible even with a temporal baseline of 24 days. As highlighted in Section 3.1.5, the scenes captured between 2011/01/26 and 2011/03/15 were captured during a time when the vegetation density was at a peak for the time of year and consequently, the evolution of the land surface is affecting the results.

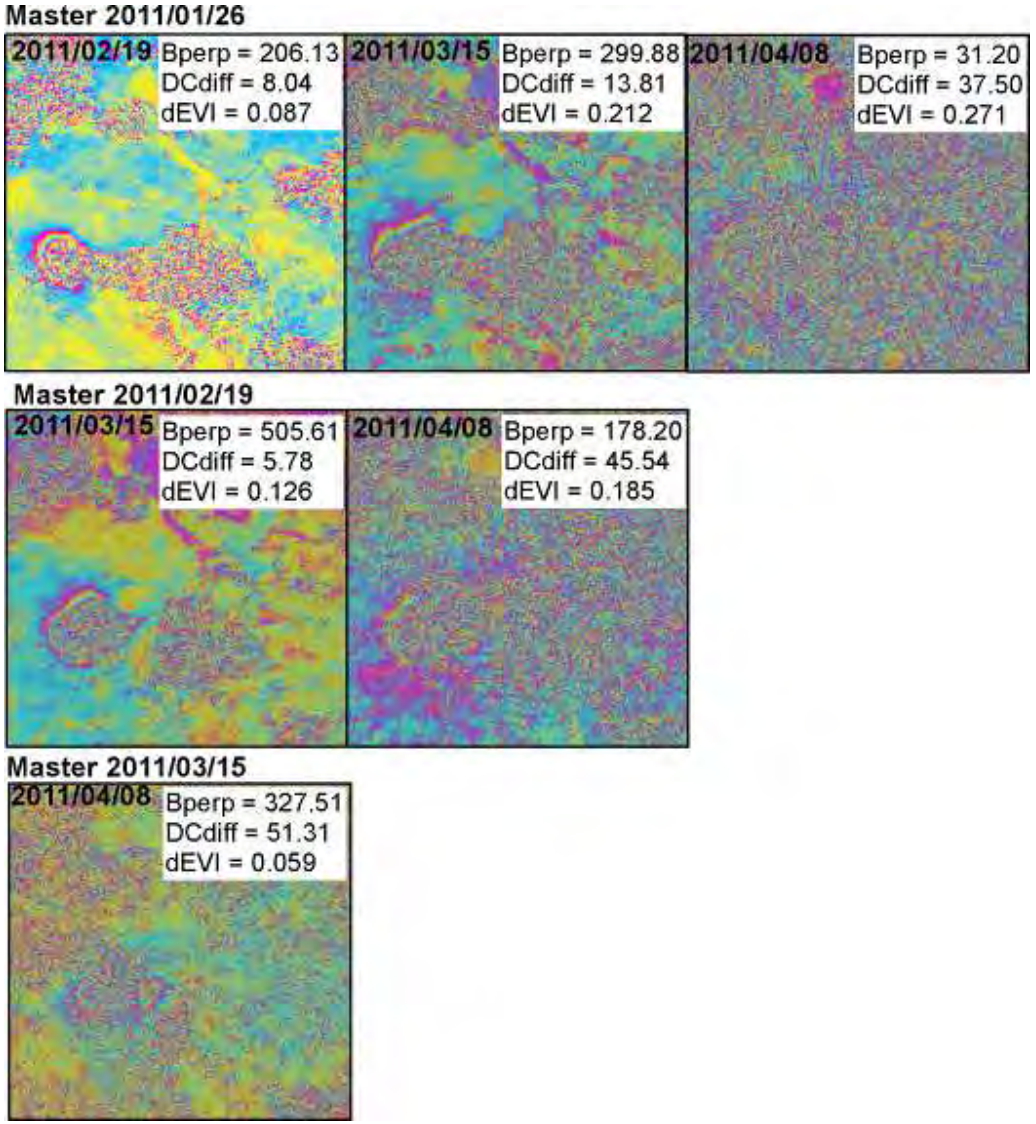
Master 2011/01/26
2011/02/19
Bperp = 206.13
DCdiff = 8.04
dEVI = 0.087
2011/03/15
Bperp = 299.88
DCdiff = 13.81
dEVI = 0.212
2011/04/08
Bperp = 31.20
DCdiff = 37.50
dEVI = 0.271
Master 2011/02/19
2011/03/15
Bperp = 505.61
DCdiff = 5.78
dEVI = 0.126
2011/04/08
Bperp = 178.20
DCdiff = 45.54
dEVI = 0.185
Master 2011/03/15
2011/04/08
Bperp = 327.51
DCdiff = 51.31
dEVI = 0.059

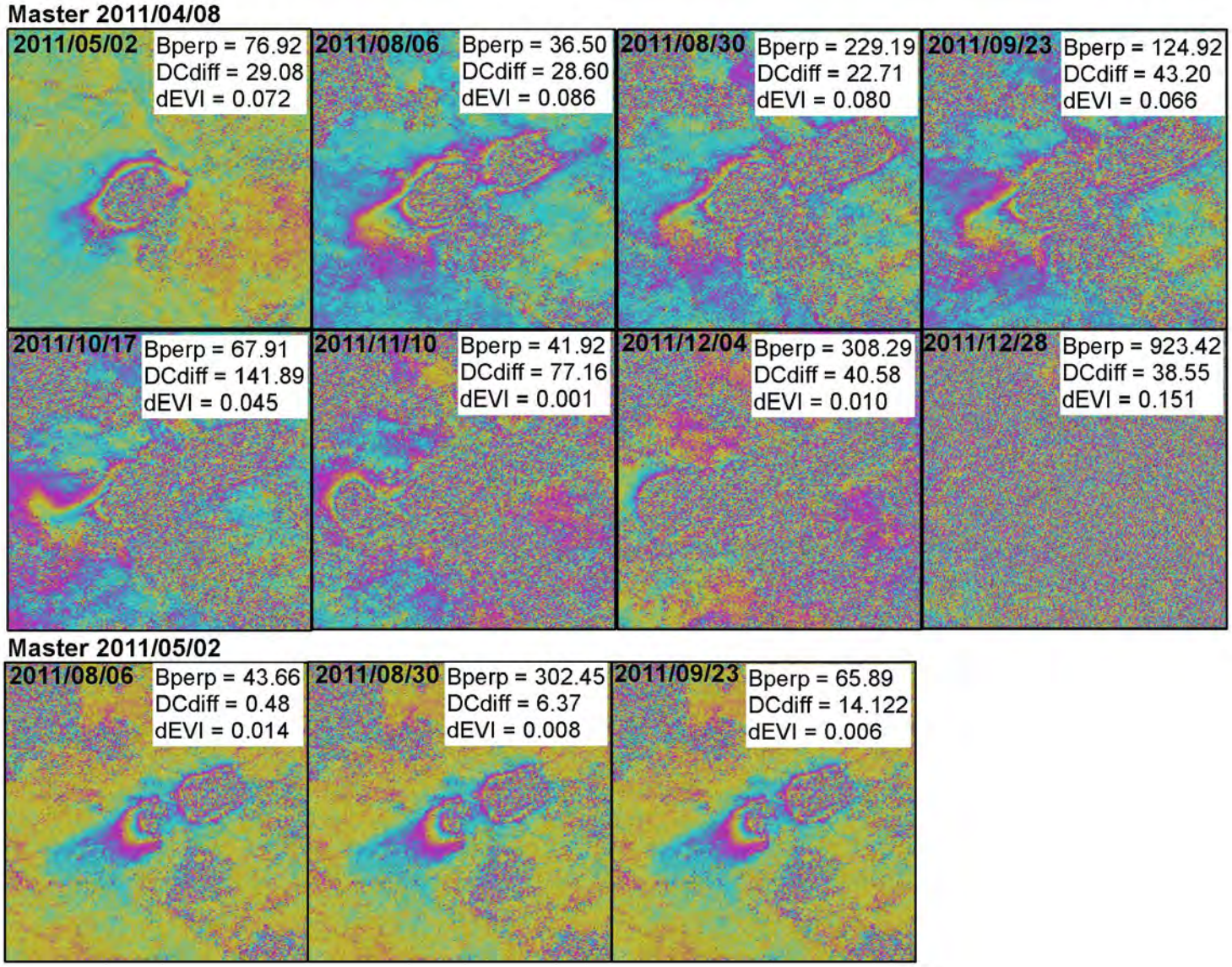
Master 2011/04/08
2011/05/02
Bperp = 76.92
DCdiff = 29.08
dEVI = 0.072
2011/08/06
Bperp = 36.50
DCdiff = 28.60
dEVI = 0.086
2011/08/30
Bperp = 229.19
DCdiff = 22.71
dEVI = 0.080
2011/09/23
Bperp = 124.92
DCdiff = 43.20
dEVI = 0.066
2011/10/17
Bperp = 67.91
DCdiff = 141.89
dEVI = 0.045
2011/11/10
Bperp = 41.92
DCdiff = 77.16
dEVI = 0.001
2011/12/04
Bperp = 308.29
DCdiff = 40.58
dEVI = 0.010
2011/12/28
Bperp = 923.42
DCdiff = 38.55
dEVI = 0.151
Master 2011/05/02
2011/08/06
Bperp = 43.66
DCdiff = 0.48
dEVI = 0.014
2011/08/30
Bperp = 302.45
DCdiff = 6.37
dEVI = 0.008
2011/09/23
Bperp = 65.89
DCdiff = 14.122
dEVI = 0.006

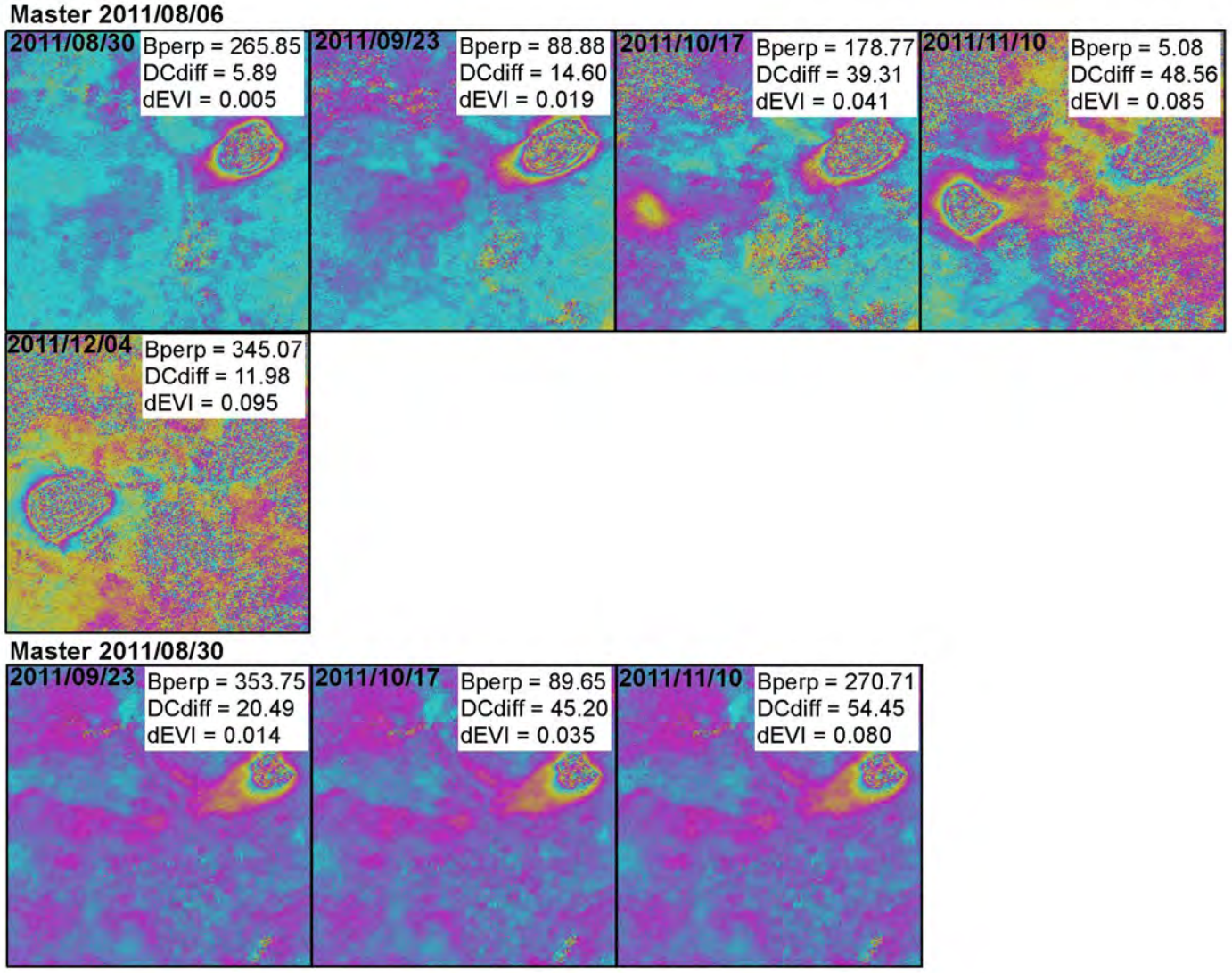
Master 2011/08/06
2011/08/30
Bperp = 265.85
DCdiff = 5.89
dEVI = 0.005
2011/09/23
Bperp = 88.88
DCdiff = 14.60
dEVI = 0.019
2011/10/17
Bperp = 178.77
DCdiff = 39.31
dEVI = 0.041
2011/11/10
Bperp = 5.08
DCdiff = 48.56
dEVI = 0.085
2011/12/04
Bperp = 345.07
DCdiff = 11.98
dEVI = 0.095
Master 2011/08/30
2011/09/23
Bperp = 353.75
DCdiff = 20.49
dEVI = 0.014
2011/10/17
Bperp = 89.65
DCdiff = 45.20
dEVI = 0.035
2011/11/10
Bperp = 270.71
DCdiff = 54.45
dEVI = 0.080

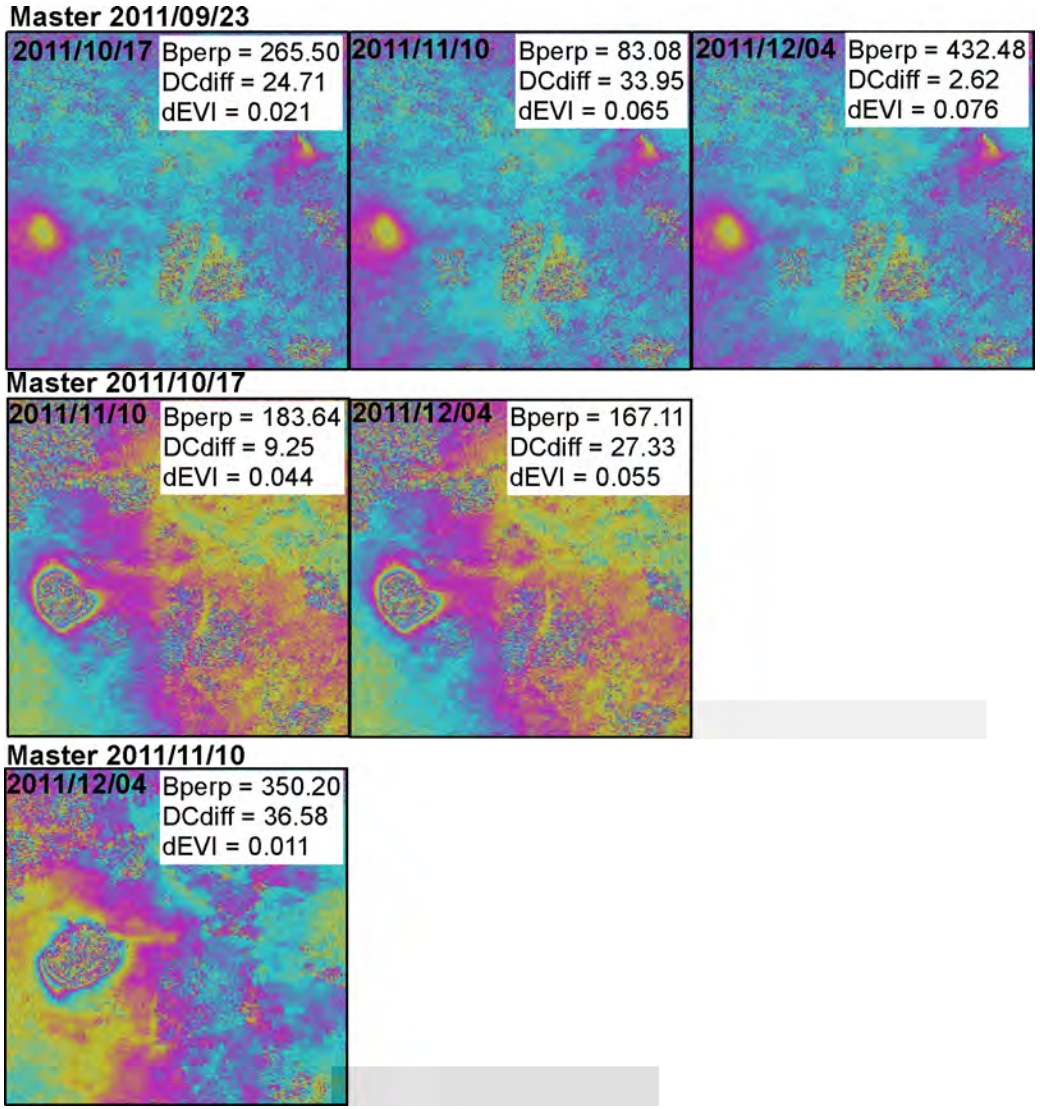

Figure 73: Time series of RADARSAT-2 differential interferograms showing deformation related fringes and the evolution of the subsidence basin over time.

For the time series created using the scene 2011/04/08 as master, the evolution of the subsidence basin over time can be observed with the extent of the subsidence basin being visible even with a temporal baseline of 168 days (master – slave = 2011/04/08 – 2011/09/23). The deformation related fringes on the edges of subsidence basins remain visible on interferograms created with temporal baselines up to 240 days. The final pair in the series, created with a temporal baseline of 264 days shows no visible fringes and the scene is dominated by noise.

Another successful time series was created using the 2011/08/06 scene as master. For this time series, the evolution of the subsidence basins over time is visible for temporal baselines of up to 72 days. For temporal baselines of 96 and 120 days, the deformation basin that was visible earlier in the series becomes dominated by noise although a new subsidence basin becomes visible to the southwest of the original basin. This suggests that work began on a new long-wall panel shortly before 2011/10/17. This is confirmed by the time series created using 2011/08/30 as master where the start of a deformation basin in the southwest corner of the scene is visible on the 2011/10/17 interferogram. The later interferometric time series also shows the ability to monitor surface subsidence in the area with the exception of interferograms created using 2011/12/28 as slave image for which all interferograms were dominated by noise and deformation detection and monitoring failed.

Although the extents of the surface subsidence basins for short temporal baseline interferograms are clearly visible, it is observed that the centres of the deformation basins are associated with a high degree of noise. This effect is due to the surface displacement exceeding the gradient limit of the sensor. In this case, deformation exceeds the 2.8 cm per pixel gradient limit imposed by the RADARSAT-2 sensor which leads to decorrelation and a decreased ability to accurately measure deformation in the centres of the subsidence basins. This implies that the maximum deformation experienced for each interferometric pair cannot be assessed even over a 24 day period. However, the extent of the subsidence basins could be extracted.

The accuracy of the monitoring of the extent of the deformation basins was confirmed by the mining companies operating in the area of interest. The extent of the longwall panels and the timeframe during which mining took place were provided. When the dates of active mining for various longwall panels are considered (Figure 74), a good agreement is found between the dates and positions of active mining

and the evolution of subsidence basins at the surface. The effect of pre-existing cavities adjacent to areas of active mining on the extent of subsidence basins is apparent. Specifically, there is an apparent reactivation of subsidence over old workings adjacent to areas of active mining. The subsidence over old workings is recognised as reactivation of subsidence over old workings as opposed to residual (or ongoing) subsidence over the workings. This is illustrated in Figure 75 where no deformation fringes are visible over the longwall panels mined between September 2010 and November 2010 (red boundaries) for the 2011/04/08 – 2011/05/02 interferogram. However, for the interferogram between 2011/08/06 and 2011/08/30, the longwall panel adjacent to these workings are being mined and deformation fringes become visible over the old workings.

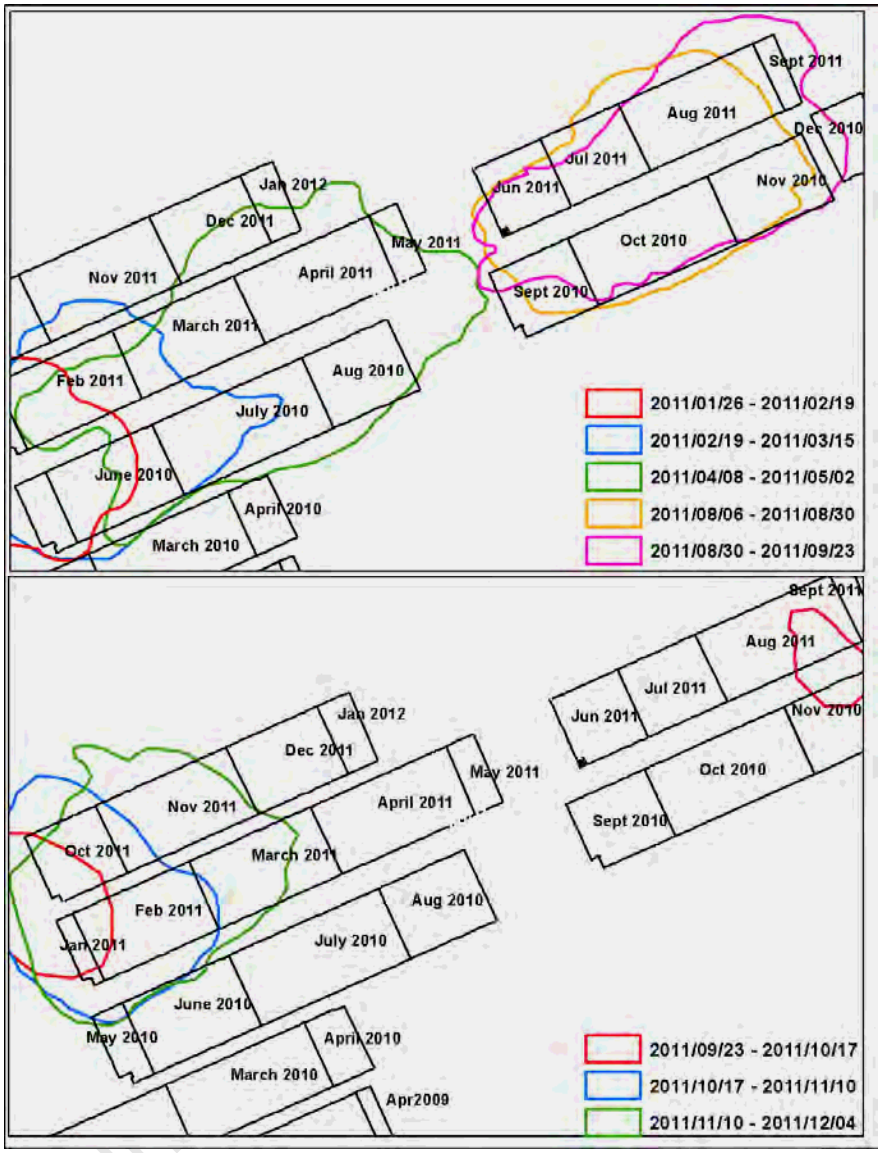

Figure 74: The extent of the surface subsidence basins and longwall mine panels. The dates of mining of the longwall panels are also indicated.

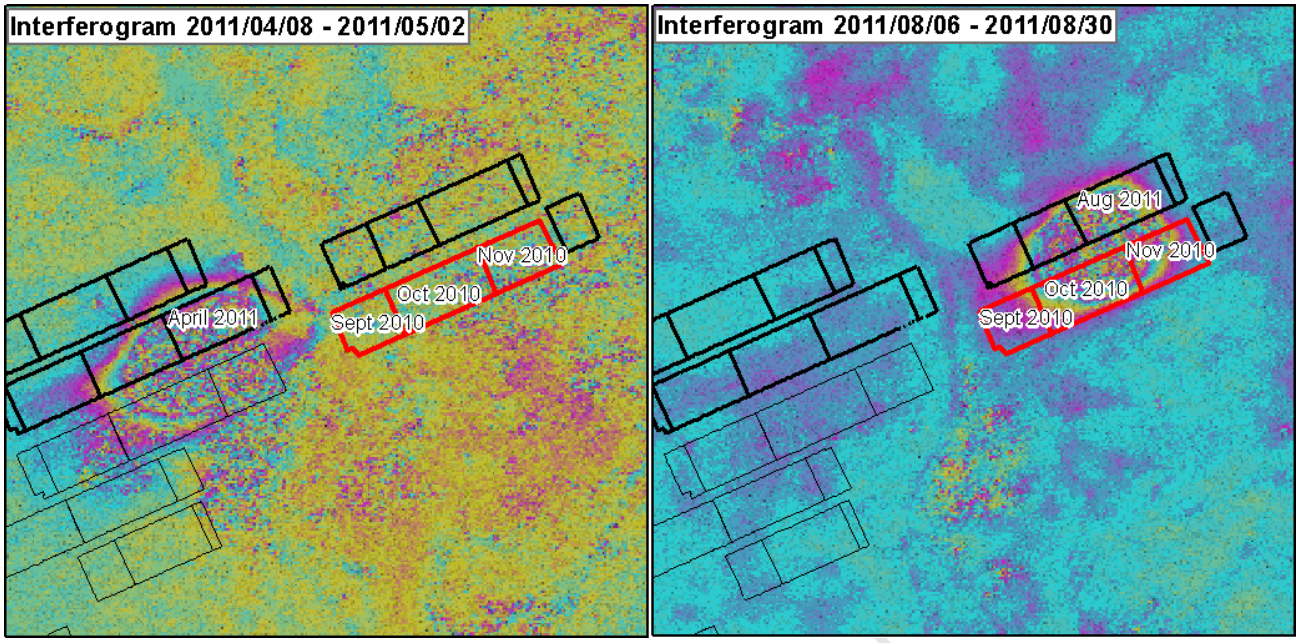

Figure 75: Recognising reactivation of subsidence as opposed to residual subsidence over old workings.

To further explore the effect of pre-existing panels (which are filled by unconsolidated roof material that collapsed during mining) and the reactivation of surface subsidence over these panels, the angle of draw for each subsidence basin was calculated. The angle of draw is defined as the angle between the side panel of the mine void and the line of zero subsidence at the surface (Figure 76). The concept of the angle of draw provided some insights into the evolution of subsidence basins and how they are affected by pre-existing longwall panels. The angle of draw for each subsidence basin was determined by calculating the centre point for each subsidence basin and drawing a line, perpendicular to the direction of mining through this centre point to the edge of the subsidence basin (Figure 77). The length of the line segments at the surface from the edge of the longwall panel to the edge of the subsidence basin was calculated for both the area adjacent to the pre-existing mine panel, and the area adjacent to the un-mined area (Figure 77).

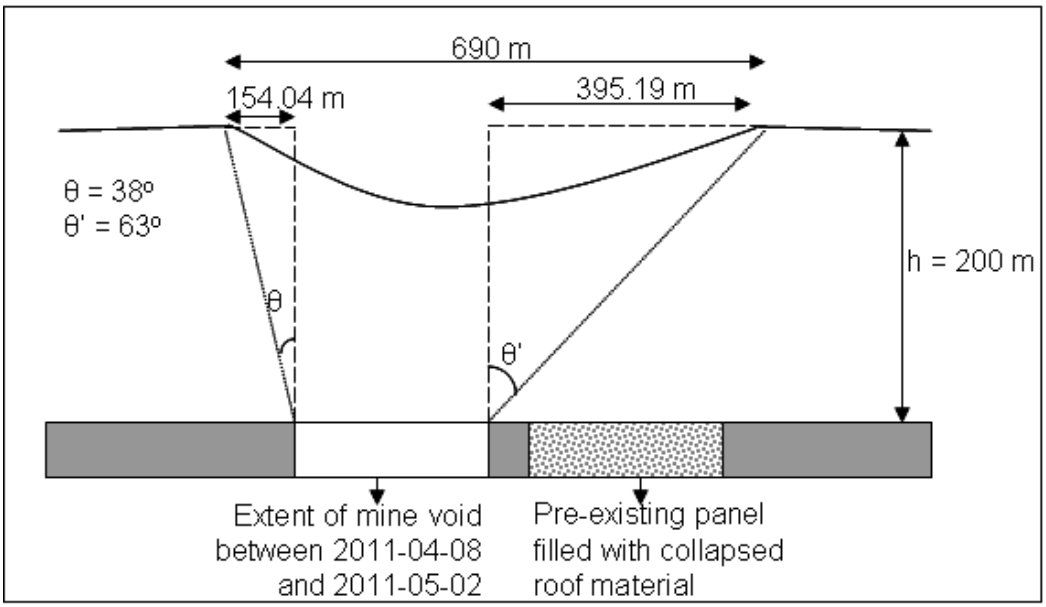

Figure 76: An illustration on the concept of the angle of draw with θ the angle of draw adjacent to an un-mined area and θ' the angle of draw adjacent to pre-existing cavities.

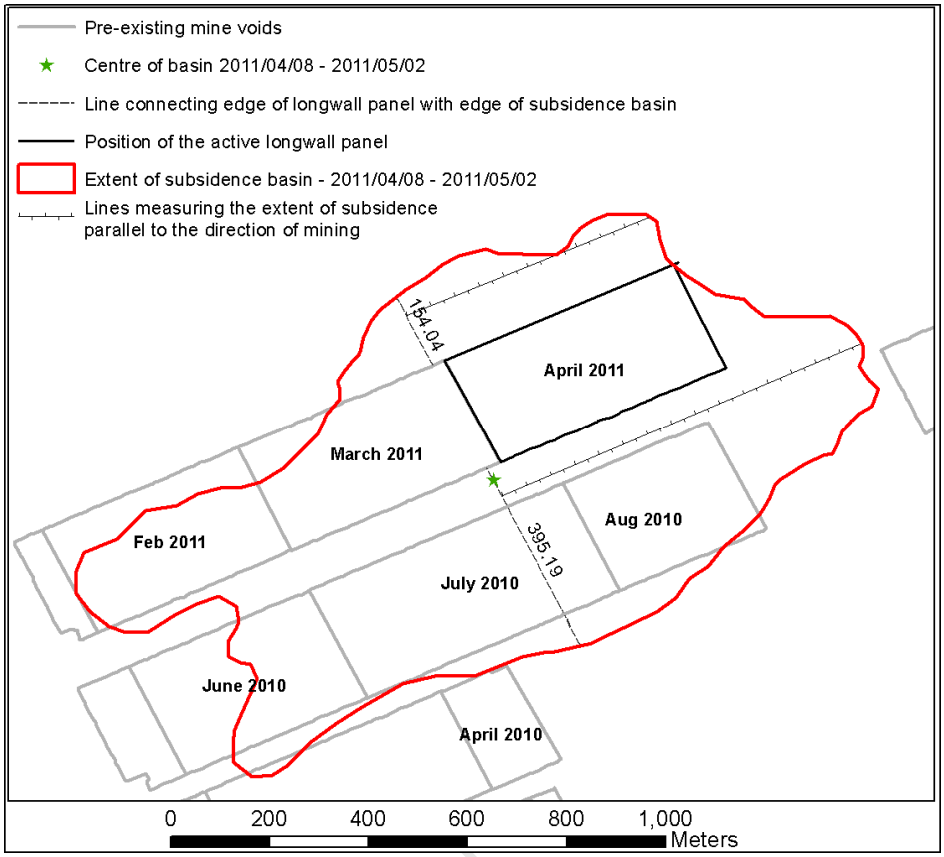

Figure 77: Calculation of the length of the lines connecting the edges of the longwall panel (at the surface) with the edges of the subsidence basin and lines used to measure the extent of the subsidence basin parallel to the mining direction.

The length of the line segments as well as the associated calculated angle of draw for each of the subsidence basins are presented in Table 16. The results confirmed that the angles of draw adjacent to un-mined areas (3.03^{o} to 42.24^{o}) were consistently lower than the angles of draw adjacent to pre-existing longwall panels (53.11^{o} to 63.16^{o}). Additionally, the effect of pre-existing panels appeared to affect the extent of the subsidence basin not only perpendicular to the direction of mining, but also parallel to the direction of mining. To confirm this, the distance from the centre line created for the calculation of the angle of draw was used as base to measure the extent of the subsidence basin parallel to the mining direction over both un-mined and previously mined areas. The results, presented in

Table 17 suggest that the maximum length-wise extension over previously mined areas is greater than the extent of the basin over un-mined areas. An exception is observed for the subsidence basin that formed between 2011/08/30 and 2011/09/23 for which the length of the subsidence basin was more or less the same over mined and un-mined areas. Another exception is observed for the period 2011/09/23 – 2011/10/17. Here the extent of the subsidence basin is slightly longer in the area of active mining. Since mining in this area commenced only shortly prior to the date that the slave image (2011/10/17) was captured, the results suggest that there may be a time-lag before pre-existing panels start affecting the extent of subsidence basins.

Table 16: Calculation of the angle of draw for subsidence basins adjacent to pre-existing panels and those adjacent to un-mined areas.

Dates	Distance adjacent to pre-existing cavities (m)	Distance adjacent to un-mined area (m)	Angle of draw adjacent to pre-existing cavities (degrees)	Angle of draw adjacent to un-mined area (degrees)
2011/01/26 – 2011/02/19	369.41	81.69	61.57	22.21
2011/02/19 – 2011/03/15	374.97	104.28	61.93	27.54
2011/04/08 – 2011/05/02	395.19	154.04	63.16	37.60
2011/05/02 – 2011/08/06	266.44	181.59	53.11	42.24
2011/08/06 – 2011/08/30	351.07	74.64	60.33	20.47
2011/08/30 – 2011/09/23	295.91	10.60	55.95	3.03
2011/09/23 – 2011/10/17	215.97	36.35	47.20	10.02
2011/10/17 – 2011/11/10	391.10	156.73	62.92	38.08
2011/11/10 – 2011/12/04	380.04	177.45	62.24	41.58

Table 17: The length-wise extension of the subsidence basin over pre-existing panels and un-mined areas parallel to the direction of mining.

Dates	Length over pre-existing cavities	Length over un-mined areas
2011/01/26 – 2011/02/19	311.68	205.04
2011/02/19 – 2011/0315	559.23	313.75
2011/04/08 – 2011/05/02	719.52	485.95
2011/05/02 – 2011/08/06	1250.20	1066.47
2011/08/06 – 2011/08/30	499.52	454.12
2011/08/30 – 2011/09/23	522.73	521.30
2011/09/23 – 2011/10/17	207.38	217.35
2011/10/17 – 2011/11/10	354.72	231.46
2011/11/10 – 2011/12/04	491.77	365.02

A time series of deformation maps was created for the interferograms least affected by noise (Figure 78). The results show that between 2.8 and 15.0 cm of subsidence was measured over a 24 day period. However, it should be noted that pixels with coherence below 0.3 were masked out (white regions in the deformation maps). This means that areas where the deformation exceeds the gradient limit could not be measured and that the actual maximum subsidence taking place over a 24 day period could be higher. Some positive deformation results are observed although these areas are associated with speckle noise and not associated with organised fringe patterns. Consequently, these areas are considered to be noise and, in theory, not suitable for deformation measurement. Ideally, noisy areas should be masked out for the process of converting differential phase to displacement. Summation of the subsidence results provided the total amount of surface subsidence due to mining activities for the period 2011/01/26 to 2011/12/04 for which a maximum of 34.7 cm of subsidence was recorded (Figure 79). The highest values are achieved in the area where the start of a new longwall panel between 2011/09/23 and 2011/12/04 resulted in the reactivation of the areas mined between 2011/01/26 and 2011/03/15. Since the deformation gradient limit was exceeded in nearly all the interferograms, the total amount of subsidence experienced is expected to be higher than the measured 34.7 cm.

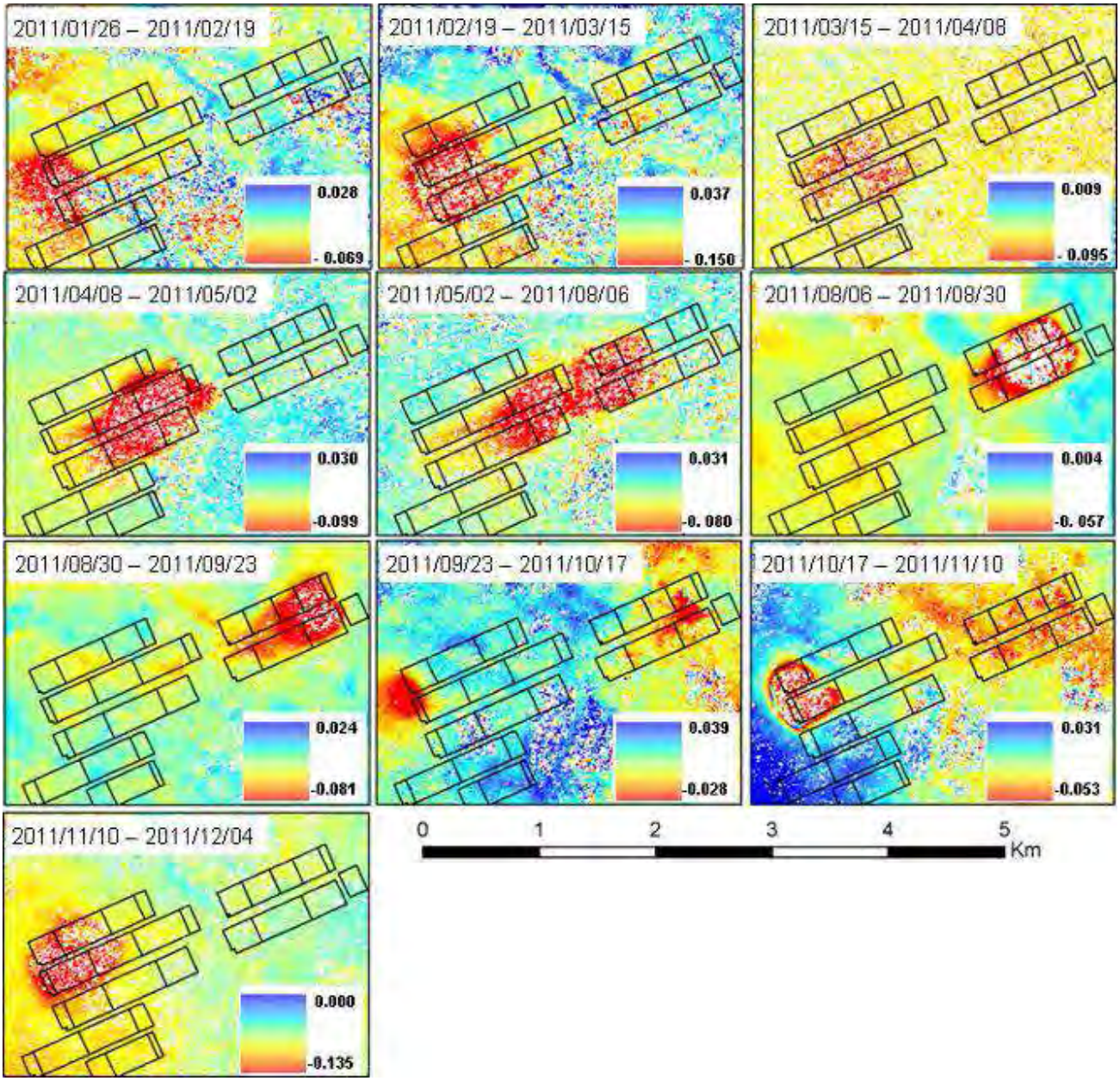

Figure 78: RADARSAT-2 time series of deformation maps derived depicting the evolution of surface subsidence over time. The deformation measurement (vertical) is in metres (m). White background is NoData.

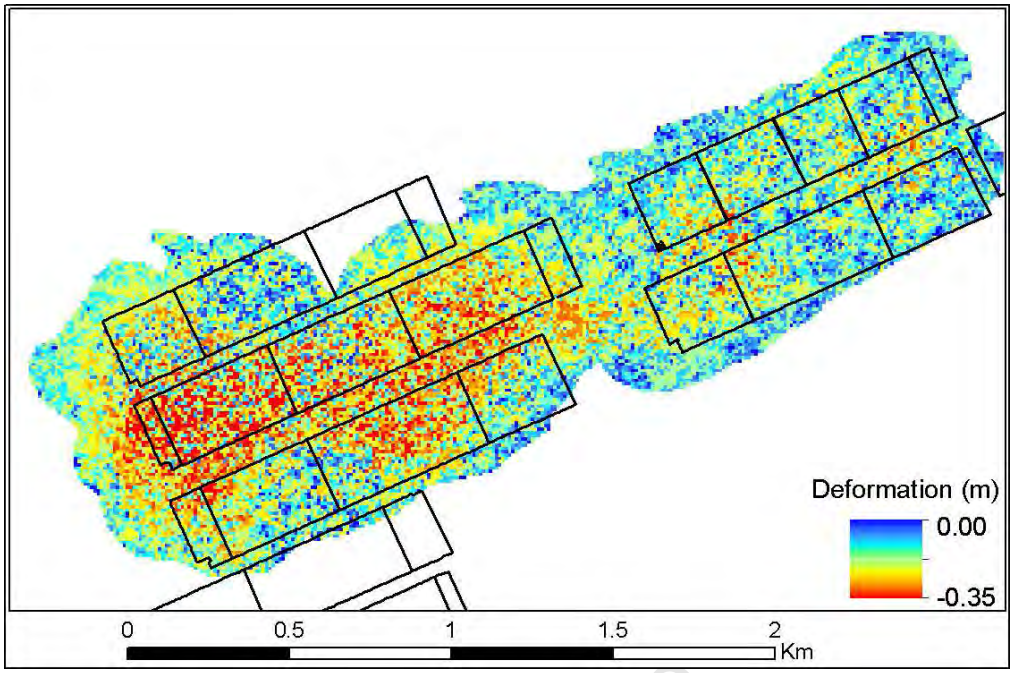

Figure 79: Total amount of subsidence (m) observed on RADARSAT-2 interferograms between 2011/01/26 and 2011/12/04.

The incoherence due to temporal decorrelation effects (including the incoherence due to the deformation exceeding the gradient limit) implies that C-band data, although successful in detecting subsidence basins and mapping their extent, was not successful in accurately measuring the total amount of subsidence experienced over a 24 day period. L-band data on the other hand is associated with a gradient limit of ~ 11.5 cm. In addition, the long wavelength data is expected to penetrate through vegetation thereby increasing the backscatter contribution from the surface implying that the temporal decorrelation effects are expected to be minimised when compared to C-band data.

The long time series for which PALSAR data was available (2007/08/16 to 2010/10/09) implied that the monitoring of the evolution of subsidence basins over a period of more than three years was a possibility. Figure 80 presents the time series of interferograms created using PALSAR data. Coherence limitations, particularly for long temporal baseline image pairs are evident. The PALSAR scenes captured on 2008/02/16, 2009/01/03, 2009/02/18, 2010/01/06 and 2010/02/21 were captured during a time where the vegetation density was higher than average for the period 2006/01/01 to 2011/11/01 (Section 3.1.5). Since the average scene coherence for L-band data was proven to be less

sensitive to the evolution of the land surface compared to C-band data (Section 4.2.2), successful interferogram creation is expected even when using these scenes as master. For the time-series created using the 2008/02/16 scene as master, it was demonstrated that successful interferogram creation was possible, even with a temporal baseline of 782 days (2010/04/08 scene as slave, Figure 80). However, the effect of land cover (speckle noise effect) is evident on the interferograms created using successively larger temporal baselines, especially along the western edge of the scenes. Although the noise introduced in these areas will not provide the ability to extract deformation measurement for these areas, the extent of subsidence basins and the monitoring of the evolution of the subsidence basin remains a possibility. The noise effect due to land cover is also evident on the interferometric series created using the 2009/01/03 and 2009/02/18 scenes as master. With the 2010/01/06 and 2011/02/21 scenes as master, interferograms with minimal noise effects were created for temporal baselines up to 92 days, in contrast with RADARSAT-2 data for which successful interferogram generation was only possible for up to 24 days when master scenes captured at the peak of the growing season were used.

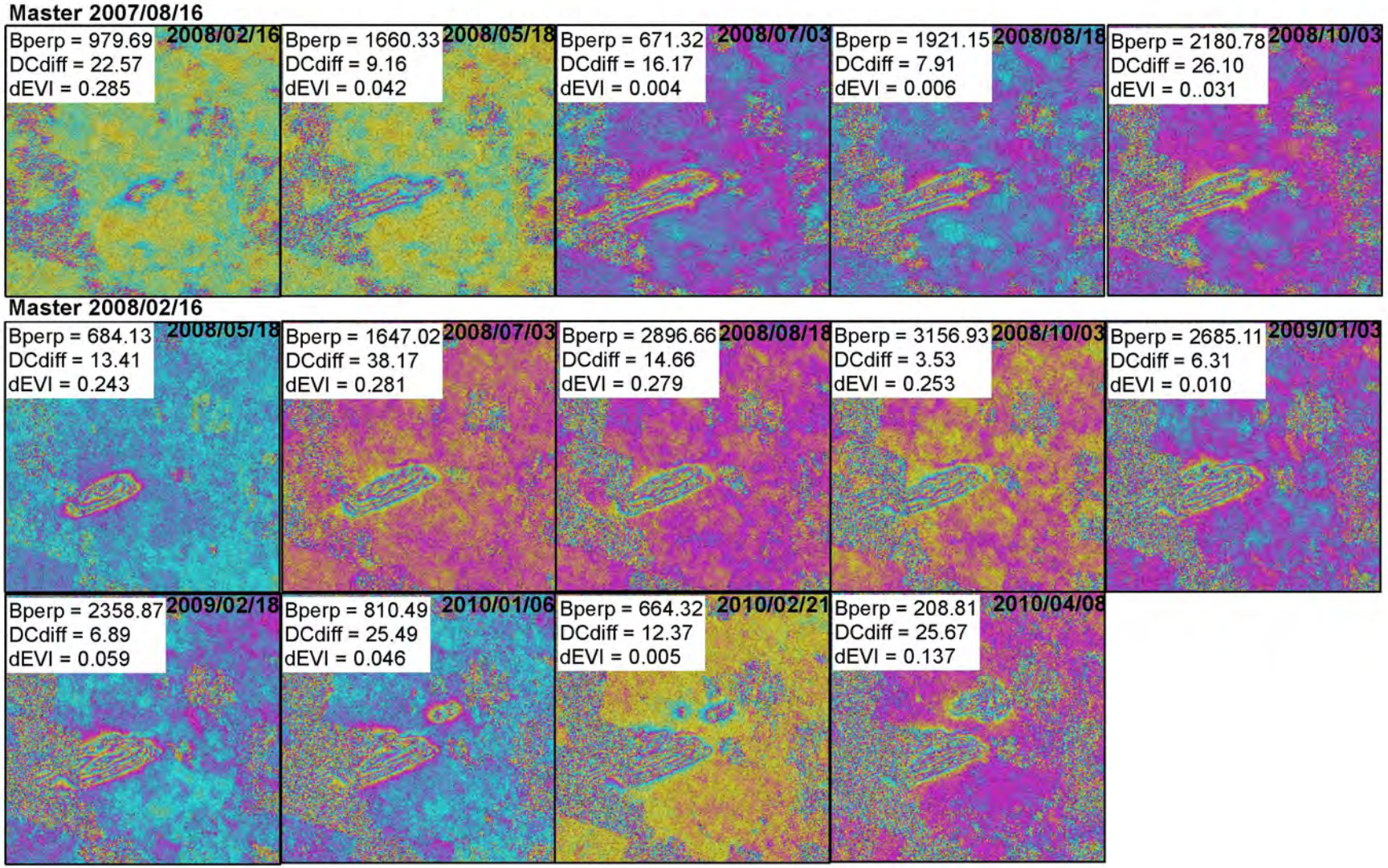
Master 2007/08/16
Bperp = 979.69
DCdiff = 22.57
dEVI = 0.285
2008/02/16
Bperp = 1660.33
DCdiff = 9.16
dEVI = 0.042
2008/05/18
Bperp = 671.32
DCdiff = 16.17
dEVI = 0.004
2008/07/03
Bperp = 1921.15
DCdiff = 7.91
dEVI = 0.006
2008/08/18
Bperp = 2180.78
DCdiff = 26.10
dEVI = 0..031
2008/10/03
Master 2008/02/16
Bperp = 684.13
DCdiff = 13.41
dEVI = 0.243
2008/05/18
Bperp = 1647.02
DCdiff = 38.17
dEVI = 0.281
2008/07/03
Bperp = 2896.66
DCdiff = 14.66
dEVI = 0.279
2008/08/18
Bperp = 3156.93
DCdiff = 3.53
dEVI = 0.253
2008/10/03
Bperp = 2685.11
DCdiff = 6.31
dEVI = 0.010
2009/01/03
Bperp = 2358.87
DCdiff = 6.89
dEVI = 0.059
2009/02/18
Bperp = 810.49
DCdiff = 25.49
dEVI = 0.046
2010/01/06
Bperp = 664.32
DCdiff = 12.37
dEVI = 0.005
2010/02/21
Bperp = 208.81
DCdiff = 25.67
dEVI = 0.137
2010/04/08

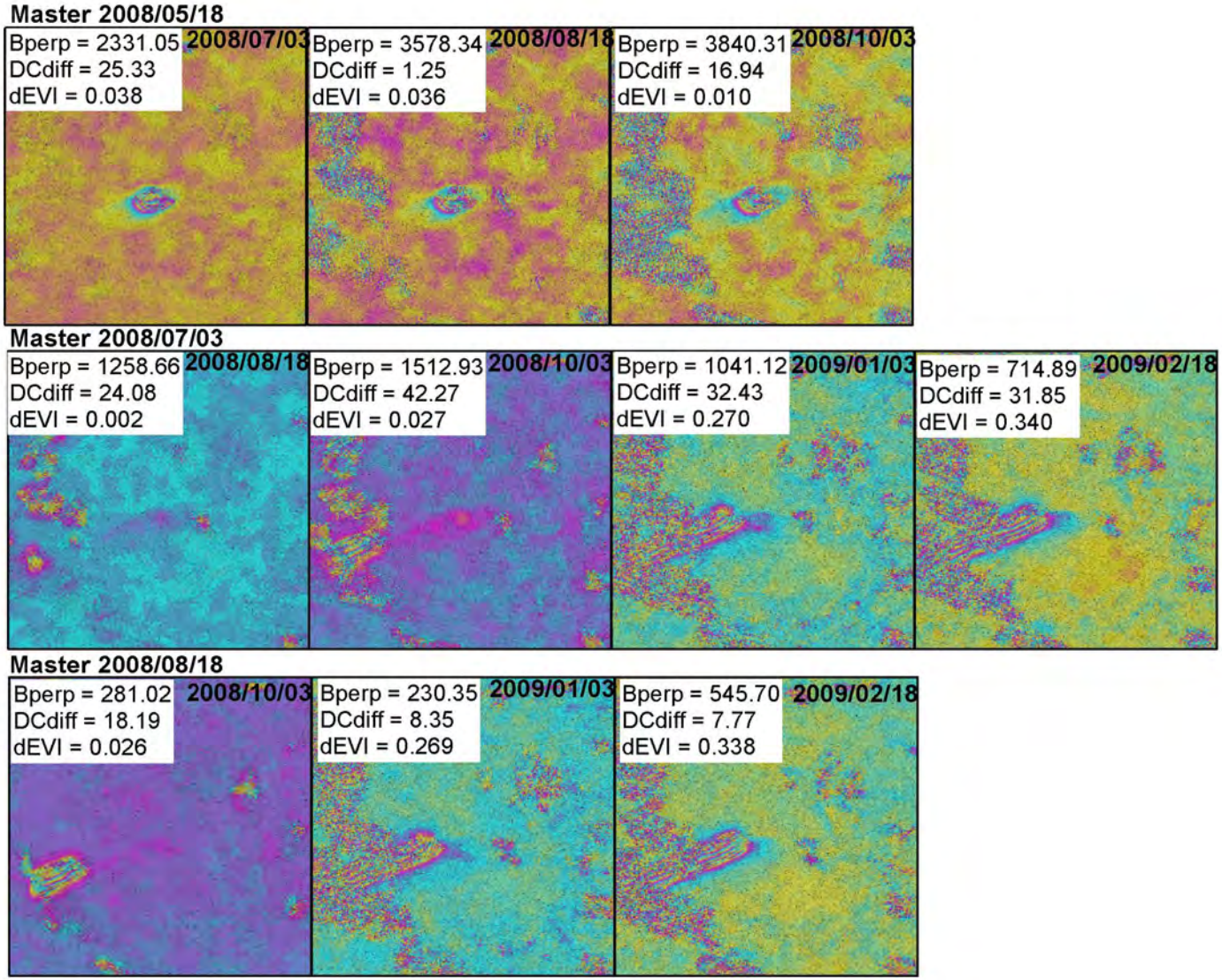
Master 2008/05/18
Bperp = 2331.05
DCdiff = 25.33
dEVI = 0.038
2008/07/03
Bperp = 3578.34
DCdiff = 1.25
dEVI = 0.036
2008/08/18
Bperp = 3840.31
DCdiff = 16.94
dEVI = 0.010
2008/10/03
Master 2008/07/03
Bperp = 1258.66
DCdiff = 24.08
dEVI = 0.002
2008/08/18
Bperp = 1512.93
DCdiff = 42.27
dEVI = 0.027
2008/10/03
Bperp = 1041.12
DCdiff = 32.43
dEVI = 0.270
2009/01/03
Bperp = 714.89
DCdiff = 31.85
dEVI = 0.340
2009/02/18
Master 2008/08/18
Bperp = 281.02
DCdiff = 18.19
dEVI = 0.026
2008/10/03
Bperp = 230.35
DCdiff = 8.35
dEVI = 0.269
2009/01/03
Bperp = 545.70
DCdiff = 7.77
dEVI = 0.338
2009/02/18

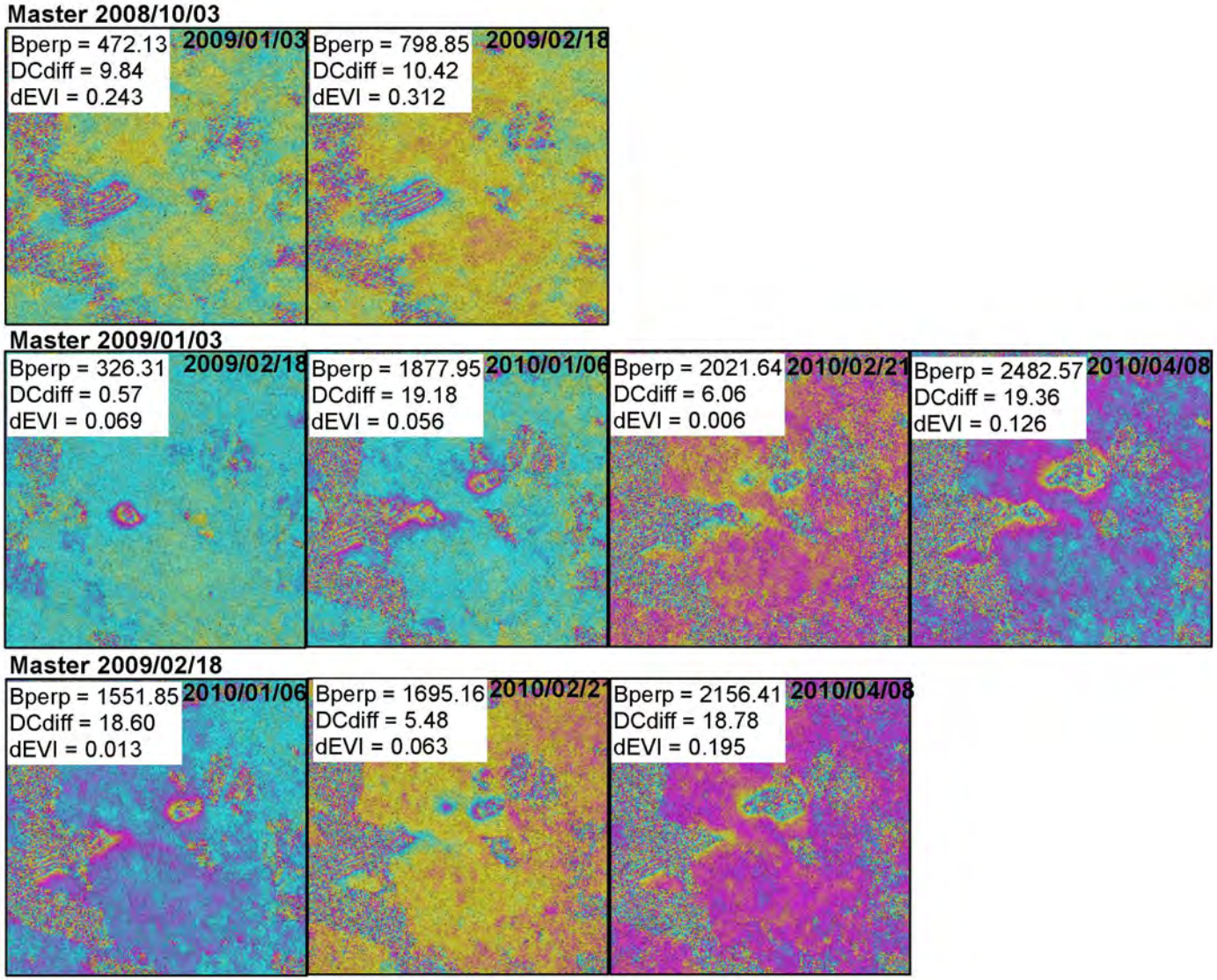
Master 2008/10/03
Bperp = 472.13
DCdiff = 9.84
dEVI = 0.243
2009/01/03
Bperp = 798.85
DCdiff = 10.42
dEVI = 0.312
2009/02/18
Master 2009/01/03
Bperp = 326.31
DCdiff = 0.57
dEVI = 0.069
2009/02/18
Bperp = 1877.95
DCdiff = 19.18
dEVI = 0.056
2010/01/06
Bperp = 2021.64
DCdiff = 6.06
dEVI = 0.006
2010/02/21
Bperp = 2482.57
DCdiff = 19.36
dEVI = 0.126
2010/04/08
Master 2009/02/18
Bperp = 1551.85
DCdiff = 18.60
dEVI = 0.013
2010/01/06
Bperp = 1695.16
DCdiff = 5.48
dEVI = 0.063
2010/02/21
Bperp = 2156.41
DCdiff = 18.78
dEVI = 0.195
2010/04/08

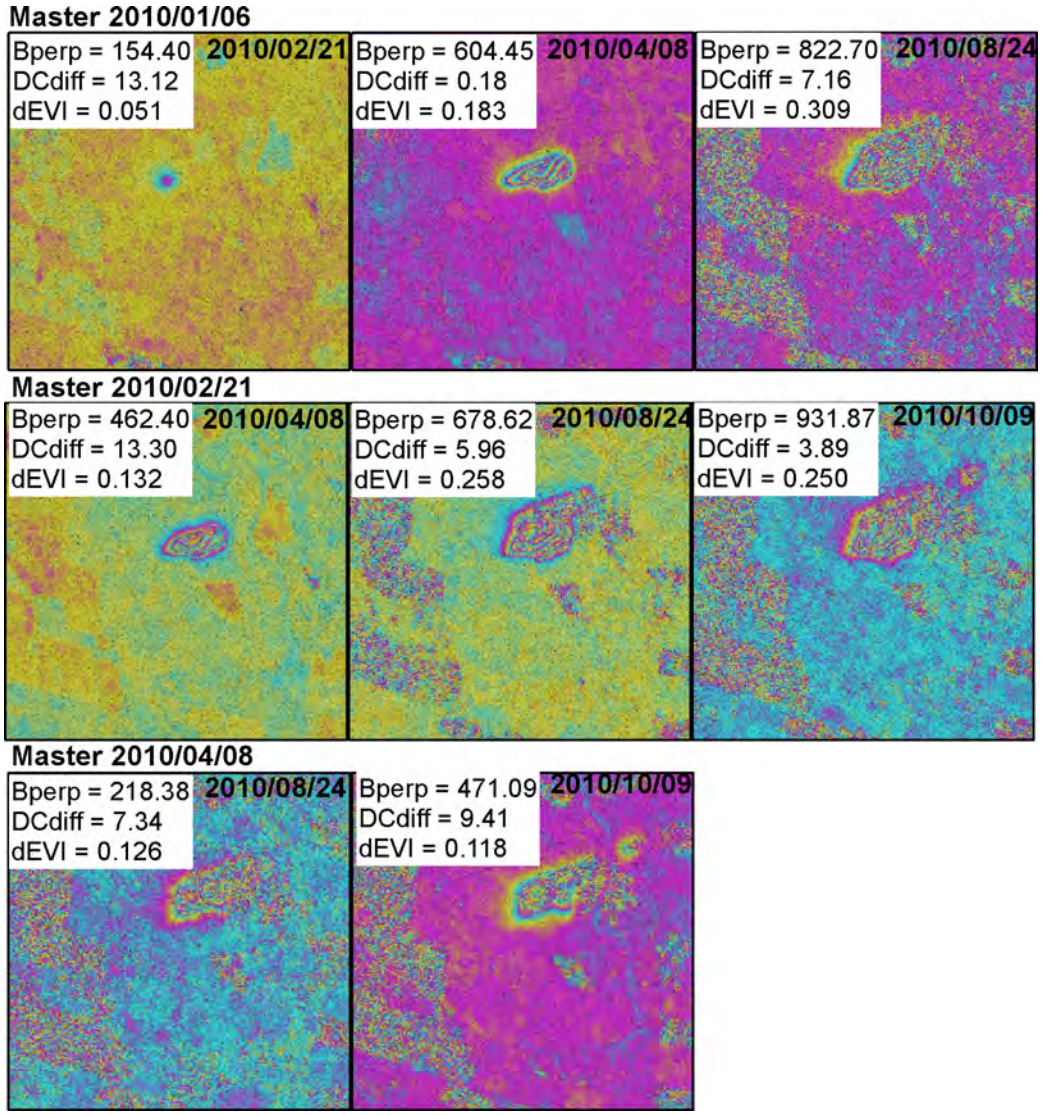

Figure 80: Series of differential interferograms from PALSAR data indicating the migration of subsidence basins over time.

It was observed that, even though longer wavelength PALSAR data was used, the centres of subsidence basins detected by PALSAR remained affected by noise similar to what was observed for the RADARSAT-2 differential interferograms although to a lesser extent. This implies that the deformation gradient limits was reached and affected the ability to extract deformation measurements. However, the extents of the subsidence basins could still be extracted from the interferograms. The accuracy of the mapping and monitoring of the extent of subsidence basins was confirmed by correlating the extent of longwall panels and their time-frame of operations with the extent of the subsidence basins detected through dInSAR techniques (Figure 81).

When the extents of the subsidence basins are correlated with the extent of the longwall panels and their time of operations, the effect of the pre-existing cavities are once again observed. The angles of draw calculations were performed and are presented in Table 18. In general, the angle of draw adjacent to un-minded areas was between 0.16 and 0.75 (average of 0.44) times smaller than the angle of draw adjacent to old workings. The effect of old workings adjacent to active panels on the lengthwise extent of the deformation basins is not as prominent as the observed effect on RADARSAT-2 measurements. However, this effect was observed for the subsidence basin that formed between 2009/01/03 and 2009/02/18 and to a lesser extent in the basin that formed between 2009/10/03 and 2009/01/03. The fact that the lengthwise extent over old workings was not detected using PALSAR data may suggest that the long wavelength data is less sensitive to small scale deformations compared to the shorter wavelength C-band data.

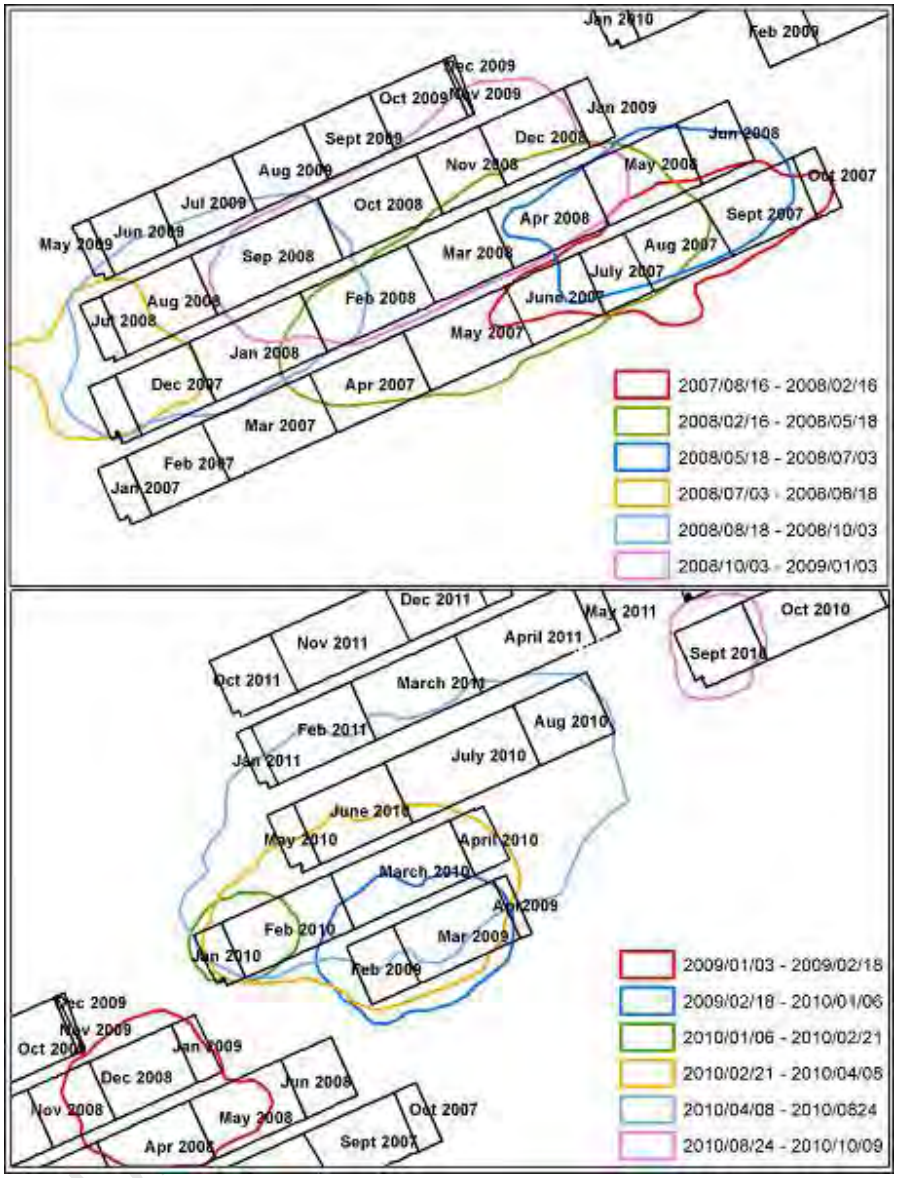

Figure 81: The extent of longwall panels and subsidence basins detected with PALSAR data. The dates of mining are also indicated.

Table 18: Angle of draw adjacent to both mined and un-mined areas calculated for subsidence basins detected using PALSAR data.

Dates	Distance adjacent to pre-existing cavities (m)	Distance adjacent to un-mined area (m)	Angle of draw adjacent to pre-existing cavities (degrees)	Angle of draw adjacent to un-mined area (degrees)
2008/02/16 - 2008/05/18	310.86	84.22	57.24	22.84
2008/05/18 - 2008/07/03	256.47	29.44	52.05	8.37
2008/07/03 - 2008/08/18	273.43	48.74	53.82	13.70
2008/08/18 - 2008/10/03	314.59	124.38	57.55	31.88
2008/10/03 - 2009/01/03	290.42	50.1	55.45	14.06
2009/01/03 - 2009/02/18	263.93	80.6	52.85	21.95
2010/02/21 - 2010/04/08	318.31	188.85	57.86	43.36
2010/04/08 - 2010/08/24	478.23	135.42	67.30	34.10
2007/08/16 - 2008/02/16	101.45	62.83	26.90	17.44

A time series of deformation maps was created for the PALSAR interferograms least affected by noise (Figure 82). The results show that between 16.1 cm and 49.1 cm (138 day temporal baseline) of subsidence was detected with the maximum deformation for 46-day temporal baseline of 37.2 cm. However, it should be noted that pixels with coherence values lower than 0.3 were masked out (white areas in deformation maps). Additionally, for several deformation measurements, the centres of the subsidence basins were dominated by noise once more implying that the 11 cm gradient limit may be exceeded and the actual amount of subsidence may be higher. Similar to C-band data, significant speckle noise remains present on the deformation maps suggesting that decorrelation effects remain dominant, even with the longer wavelength L-band data. However, it should be noted that the temporal baselines for the L-band data were significantly longer (up to 322 days) in contrast to the temporal baselines for RADARSAT-2 data (up to 96 days). Summation of the subsidence results provided the total amount of subsidence as measured with PALSAR data between 2007/08/16 and 2010/10/09. The results show that a total of 60 cm of subsidence was recorded which is in the 40 – 80 cm range reported by mining companies operating in the area (Section 1.5). However, since the centres of the subsidence

basins were in cases masked out due to the coherence threshold being exceeded, the total amount of subsidence may be higher than the recorded 60 cm.

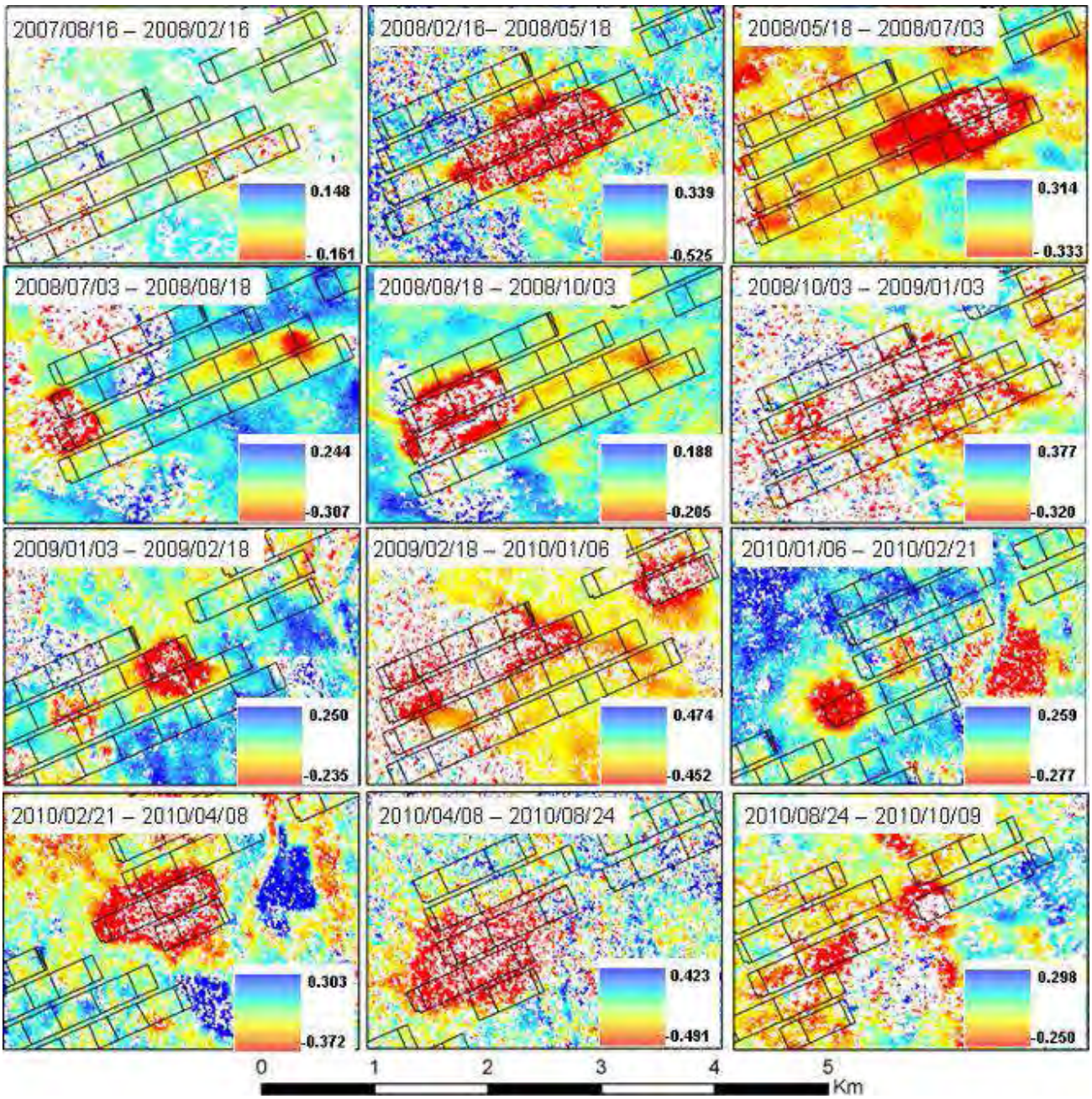

Figure 82: Time series of deformation maps created from PALSAR data depicting the evolution of surface subsidence over time. Deformation is measured in metre (m).

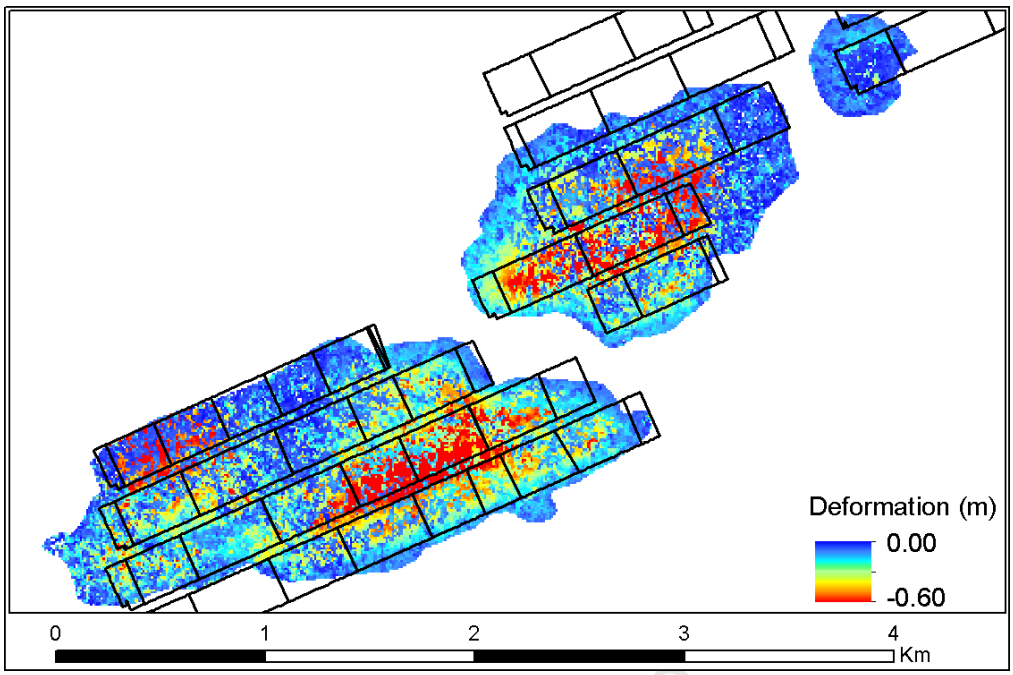

Figure 83: The total subsidence (m) as measured with PALSAR data.

The TerraSAR-X data available for the investigation did not cover the area of active longwall mining for which ground truth data was available. Consequently the effectiveness of the X-band data for the measuring and long-term monitoring of mining induced deformation could not be assessed. However, it is expected that the small deformation gradient limit of X-band data (~ 1.5 cm per 3 m pixel) and the fact that data was captured at 22-day temporal baselines at best, will imply the deformation gradient limit will be exceeded, prohibiting deformation measurement. Additionally, the high sensitivity of the X-band data to temporal decorrelation effects (Section 4.3.2) would make the use of X-band data unsuitable for deformation mapping in the area of interest.

6 DISCUSSION

The different sensitivities of different sources of data to the various sources of decorrelation can be used to investigate the optimal sensor configuration in terms of temporal baseline, land surface conditions and perpendicular baseline for the long term operational monitoring of deformation in the area of interest. Section 6.1 discusses the optimal image acquisition strategies for C-band, L-band and X-band sensors in isolation. Section 6.2 investigates the success and failures of the coherence optimisation approaches used in this investigation. Finally, the implications of these analyses on the

measurement of surface deformation and the implications for the long term monitoring of surface deformation using dInSAR techniques are discussed in Section 6.3.

6.1 COHERENCE LIMITATIONS AND CONTRIBUTING FACTORS

6.1.1 C-band

The results of the sensitivity analysis on RADARSAT-2 data (Figure 84) suggest that changes in Doppler Centroid difference will have the least significant impact on average scene coherence. However, considering the fact that the Doppler Centroid (DC) difference for the data analysed was low (< 4% of critical Doppler), the effect of DC difference may be underestimated. Similarly, the effect of perpendicular baseline (B_{perp}) on average scene coherence is lower than expected, though this may be due to generally low B_{perp} values reported for the available data. It is expected that if a higher frequency of datasets with high DC difference and B_{perp} values were available, the results would change significantly. This was confirmed by comparing the sensitivity of RADARSAT-2 and ERS-2 coherence to B_{perp}, DC difference and temporal baseline. The results (Figure 85) indicate that, with higher B_{perp} and DC Doppler values available, the C-band data appears to be the most sensitive to DC difference, followed by the sensitivity to B_{perp} and the lowest sensitivity to temporal baseline.

If only RADARSAT-2 data is considered, temporal decorrelation effects (temporal baseline and land surface evolution) were shown to have the most significant effect on average scene coherence (Figure 84). All polarisations exhibit the highest sensitivity to temporal decorrelation effects. HH and VV polarisations exhibited slightly higher sensitivities to temporal decorrelation suggesting that volume decorrelation effects affected HH and VV signals as well as the HV signal. The slightly higher sensitivity to temporal decorrelation effects for HH polarisation data may be due to the increased interaction with the surface for HH data compared to VV data suggesting that changes in surface roughness conditions due to tilling, planting and harvesting may be adding to the temporal decorrelation effects for HH polarisation data.

The VV polarisation data appears to be slightly more sensitive to baseline decorrelation effects than HH polarisation data (Figure 84). A change in incidence angle associated with the perpendicular baseline is expected to alter the travel distance through vegetation. Since VV polarisation is more likely

to interact with the vertical crops, changes in travel distance may induce incoherent changes in the signal due to changing interactions with vegetation. The incoherent changes due to interaction with vegetation will result in a decrease in coherence associated with the apparent change in baseline. The higher sensitivity of VV polarisation to the effects of land surface evolution may also be linked to the higher sensitivity of VV polarisation to surface roughness effects. As described in (Section 4.4.1), polarimetric analysis revealed that agricultural fields appear rough for the largest part of the year except for after 2011/05/02 up to 2011/09/23 were the fields appear to be smooth. VV polarisation data is more sensitive to changes in surface roughness than HH polarisation data (Section 2.3.2). Consequently, changes in roughness conditions induced by activities such as tilling, planting and harvesting would have a greater impact on VV polarisations compared to HH polarisations.

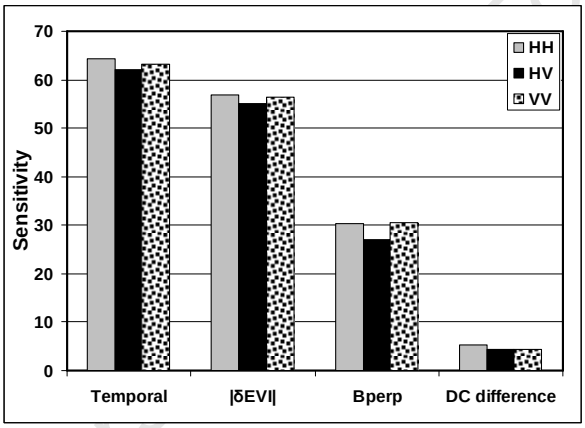

Figure 84: The average scene coherence's sensitivity to respective parameters for RADARSAT-2 data.

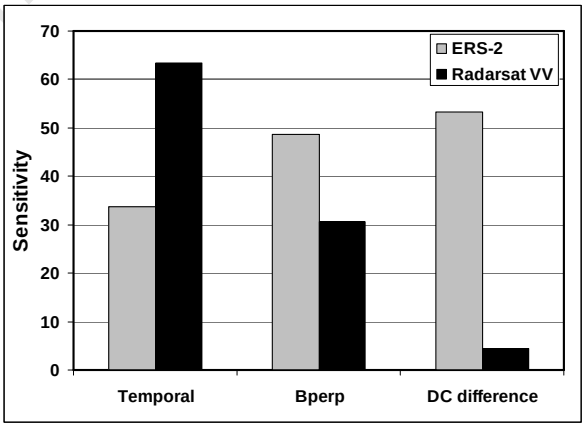

Figure 85: The sensitivity of ERS-2 and RADARSAT-2 coherence to temporal baseline, B_{perp} and DC difference.

Although the strong dependency of interferometric coherence on polarisation have been previously described (Cloude & Papathanassiou 1998), the results obtained in this investigation showed that the average scene coherence for HH and VV polarisation data at C-band varied only minimally. While HH polarisation is expected to be optimal for interferometric measurement in an area dominated by vertical crops, the choice of polarisation is not straightforward and depends on the season in which the scenes are captured.

The results of this investigation found that, while scene coherence for HH polarisation data was slightly higher for the majority of InSAR pairs, the use of VV polarisation would also be suitable in most cases. Specifically, it was observed that, for SAR scenes captured at the peak of the growing season and periods of high vegetation biomass, HH polarisation is preferred. On the other hand, if monitoring is to take place after harvesting during a period where the vegetation biomass is low, VV polarisation data is preferred. It should be noted however that the phase measurements in different polarisations provides information for different scattering mechanisms within a resolution cell and consequently, different phase centres for different polarisations, which will introduce a topographic phase change in differential interferograms (Navarro-Sanchez et al. 2010).

6.1.2 L-band

The results of the sensitivity analysis on L-band data (Figure 86) suggest that the long wavelength PALSAR data is most sensitive to temporal baseline decorrelation effects. This is followed by the sensitivity to perpendicular baseline. The average coherence for PALSAR data appears to be the least sensitive to Doppler Centroid differences and changes in land surface conditions. However, as mentioned in Section 4.2.1, the Doppler centroid differences for the interferometric scenes were very low and a higher sensitivity to Doppler centroid difference may be expected for large DC difference datasets. The low sensitivity to changes in land surface conditions for L-band data was also expected since the long wavelength radiation were expected to penetrate through vegetation, and consequently agricultural changes including crop growth and harvesting were not expected to affect average coherence significantly. Additionally, polarimetric analysis of the PALSAR data suggested that the agricultural fields appeared smooth at L-band irrespective of the time of year (Section 4.4.1).

Consequently, changes in roughness conditions such as tilling and harvesting did not affect interferometric coherence to a significant degree.

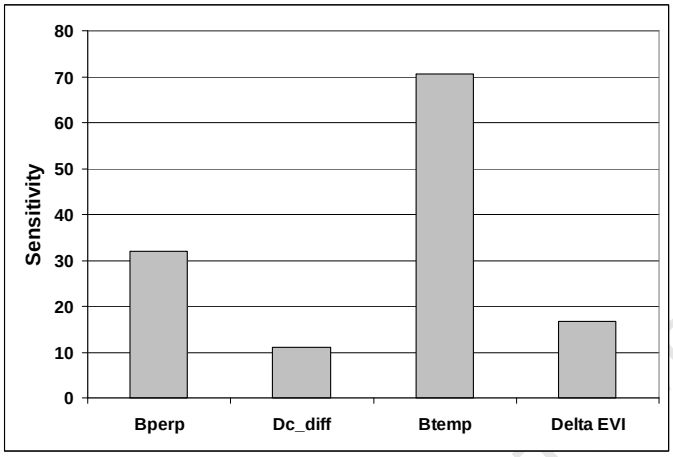

Figure 86: The sensitivity of PALSAR coherence to geometric and temporal decorrelation effects.

The relatively high sensitivity to perpendicular baseline was surprising since 78% of the interferometric pairs were captured with perpendicular baselines < 20 % of critical baseline and higher backscatter contributions from the surface minimises baseline decorrelation effects compared to backscatter from vegetation (Section 2.2). This was demonstrated by the observation that scenes captured at a time where vegetation densities were high (increase in volume scattering contributions) were more sensitive to baseline decorrelation effects than scenes captured where vegetation densities were low (Section 4.2.1). However, as mentioned in Section 2.2, the backscatter from smooth surfaces is more sensitive to changes in incidence angles. Consequently, baseline decorrelation effects are expected to be more prominent for the smooth surfaces at L-band compared to surfaces that appear rough at C-band. The results suggest that if more scenes with larger perpendicular baselines were available, the sensitivity of average scene coherence may increase even though surface scattering contributions dominate.

Although L-band data signals were expected to penetrate through vegetation thereby increasing surface interaction, volume scattering contribution remained present as was determined by baseline decorrelation effects and polarimetric analysis. Additionally, interferometric coherence for L-band data exhibited the highest sensitivities to temporal baseline decorrelation effects. Specifically, the density of vegetation at the time of master scene acquisition appeared to have a significant effect on average scene

coherence with master scenes captured at high vegetation densities exhibiting lower average scene coherence values than pairs with master scenes captured at low vegetation densities. The results suggest that, although surface scattering contributions are maximised, volume decorrelation due to the presence of vegetation is still affecting the longer wavelength signal in a significant way.

Determination of the optimal polarisation for L-band data was difficult since only three fully polarimetric scenes were available. The coherence from volume scattering contributions is independent of polarisation whilst coherence from surface scattering contributions is dependent on polarisation (Papathanassiou & Cloude 2001). Since L-band data provides an increased interaction with the surface which increases the dependence of average scene coherence on polarisation, the choice of polarisation will be important for long term operational monitoring. Although only three polarimetric datasets were available to investigate the optimal polarisation to use for long term monitoring, the results suggest that VV polarisation will provide higher interferometric coherence than HH polarisation (Section 4.2.3).

6.1.3 X-band

The results of the sensitivity analysis on TerraSAR-X data (Figure 87) revealed the greatest sensitivity to the evolution of the land surface (delta EVI) irrespective of image acquisition mode. This was followed by the sensitivity to temporal baseline, DC difference and perpendicular baseline. Since the short X-band signal is expected to interact primarily with vegetation, the sensitivity to temporal decorrelation effects (including evolution of the land surface and temporal baseline decorrelation) was expected.

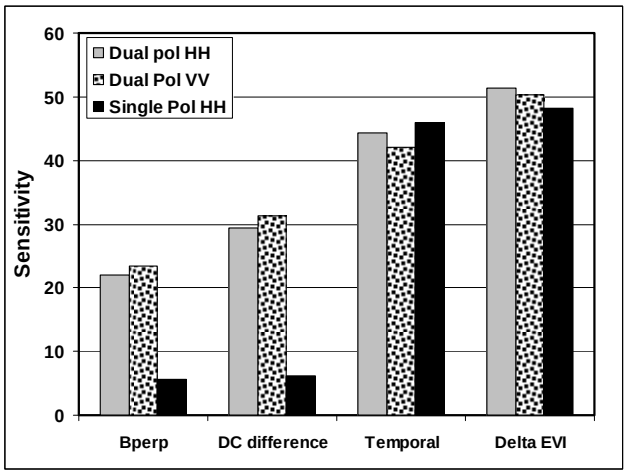

Figure 87: The sensitivity of TerraSAR-X datasets to temporal and baseline decorrelation effects.

Since volume scattering contributions are expected to dominate, the sensitivity to baseline decorrelation effects is expected to be higher. However, it was observed that perpendicular baselines of the TerraSAR-X scenes were between 0.081 and 5.125% of the critical baseline. Given the low perpendicular baselines for the interferometric pairs, the low sensitivity to baseline decorrelation effects could be expected. Additionally, the DC difference values for the interferometric pairs were between 0.063 and 2.820 % of the critical Doppler meaning that the low sensitivity to decorrelation as a result of Doppler centroid differences were also anticipated. The dominance of volume scattering contributions also implies that the average scene coherence is not affected by polarisation.

6.2 COHERENCE OPTIMIZATION ALGORITHMS – SUCCESS OR FAILURE

Polarimetric interferometry is recognised for its potential to significantly improve the quality of long temporal baseline interferometric pairs (Reigber et al. 2007). Phase noise introduced into interferograms causes pixels to undergo random phase changes which visually manifest as randomly coloured speckles in interferograms and, consequently, destroy the organised fringe pattern associated with interferograms (Massonnet & Feigl 1998). The coherence optimisation algorithms implemented in this investigation attempted to optimise the interferometric coherence by identifying the phase contribution from scattering mechanisms that lead to the highest possible coherence. Although the optimization of interferometric coherence was statistically achieved, the optimization did not translate to the differential interferometric phase (Section 4.4.2). More specifically, the random phase noise

effect remained present on the optimised coherence data as was evident by calculating the coefficient of variation of the coherence for traditional dInSAR and polInSAR results (Section 4.4.2).

The coefficient of variation (CV) for polInSAR results on C-band data was consistently higher than the CV for traditional single polarisation dInSAR results. This is indicative of a decrease in the spatial homogeneity of the phase noise contribution. The decrease in the spatial homogeneity of the phase noise was associated with an increase in the random speckle effect on the derived interferograms. The L-band data on the other hand demonstrated an increase in the spatial homogeneity of the coherence after optimisation algorithms were applied. The polarimetric analysis of the L-band data revealed that low entropy surface scattering mechanisms dominated irrespective of the time of year (Section 4.4.1). Consequently, the coherence optimisation algorithms were more likely to select the same scattering mechanism between neighbouring pixels which would lead to more homogeneous results. This suggests that longer wavelength data is, in theory, more successful in minimising phase noise through coherence optimisation techniques. However, although the number of fully polarimetric L-band interferometric pairs was insufficient to be conclusive, the results suggested that an increase in temporal baseline is also associated with a significant increase in the spatial heterogeneity of the phase noise contribution resulting in the destruction of the organised fringe pattern needed for successful interferometric measurement. This suggests that, polInSAR on PALSAR data could potentially be used to minimise the phase noise heterogeneity although only for shorter temporal baseline data.

A strong correlation between the polInSAR coherence values and coherence values obtained by traditional dInSAR was observed (Section 4.4.2). This implied that the parameters affecting the phase noise component of interferograms affected the dInSAR and polInSAR interferograms equally. Although the polInSAR coherence is slightly less correlated to $|\delta \mathrm{EVI}|$ than the dInSAR coherence, the correlation between the polInSAR coherence and temporal baseline is similar to the correlation between the dInSAR coherence and temporal baseline. It is therefore concluded that, although coherence can be statistically optimised using polInSAR techniques, the techniques are not successful in significantly decreasing the phase noise due to evolving land surfaces and volume decorrelation. This confirms that coherence optimisation partially reproduces phase noise effects evident in dInSAR interferograms.

An explanation for the failure of coherence optimisation techniques in minimising the phase noise component can be derived by considering the dominant scattering processes in the scene and how they change between master and slave image acquisitions. Although polarimetric analysis proved that the dominant scattering mechanism for the 2011/08/06 and 2011/08/30 scenes are low entropy surface scattering (Section 4.4.1), some volume scattering contributions and surface roughness propagation effects were also observed. Post-classification change detection algorithms on the H-A-alpha classification (Section 4.4.1), were used to highlight the dominant changes in scattering mechanisms between image acquisitions.

An example of the changes in scattering mechanism between master and slave image acquisition is presented in Figure 88 using a subset of the 2011/08/06 – 2011/08/30 interferometric pair as example. The results for this interferometric pair show that significant changes in the dominant scattering mechanism over time is experienced with Bragg surface scattering changing to surface roughness propagation effects being the most dominant change. Surface roughness propagation effects changing to volume scattering (vegetation) are also observed. The observed changes in scattering mechanism were spatially heterogeneous and, together with the volume scattering contributions, introduce random phase changes between the master and slave image acquisitions which cannot be removed by polInSAR techniques.

When the maximum coherence image (Figure 88) is considered, it is apparent that the subsiding area is associated with low interferometric coherence. The low coherence is due to the deformation between 2011/08/06 and 2011/08/30 exceeding the 2.8 cm per pixel gradient limit imposed by the RADARSAT-2 sensor. This implies that, even if the phase contribution from surface scattering mechanisms could be isolated to provide very high coherence interferograms, surface deformation exceeding the gradient limit would continue to cause incoherence and polInSAR is not capable of minimising the phase noise in these areas.

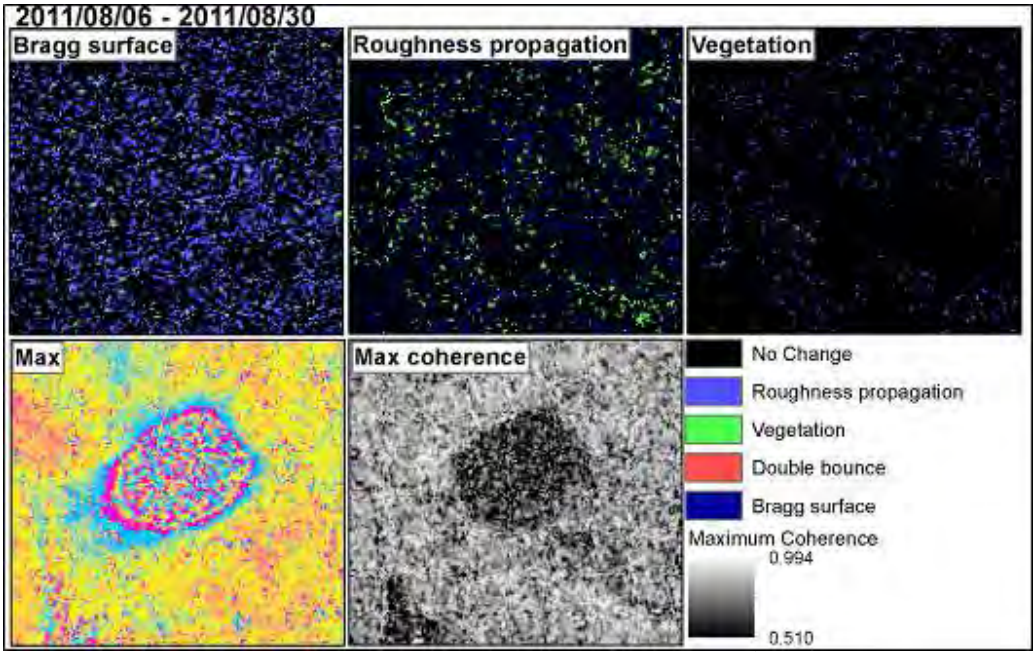

Figure 88: Scattering mechanism changes between 2011/08/06 and 2011/08/30. The top row labelling indicates the initial scattering state on 2011/08/06 as Bragg surface scattering, Roughness propagation effects and vegetation respectively. The colours indicate the scattering mechanism change reflected on 2011/08/30.

The longer wavelength PALSAR data is associated with a larger gradient limit of 11 cm per pixel. Additionally, the L-band data is associated with an enhanced ability to penetrate through vegetation and is predominantly associated with surface scattering contributions as demonstrated in Section 4.4.1. However, the post classification change detection on the classification based on scattering mechanism reveals that changes in scattering mechanisms between master and slave image acquisitions are still taking place. An example of this effect is presented in Figure 89 for a subset of the 2008/10/27 to 2009/04/29 scenes.

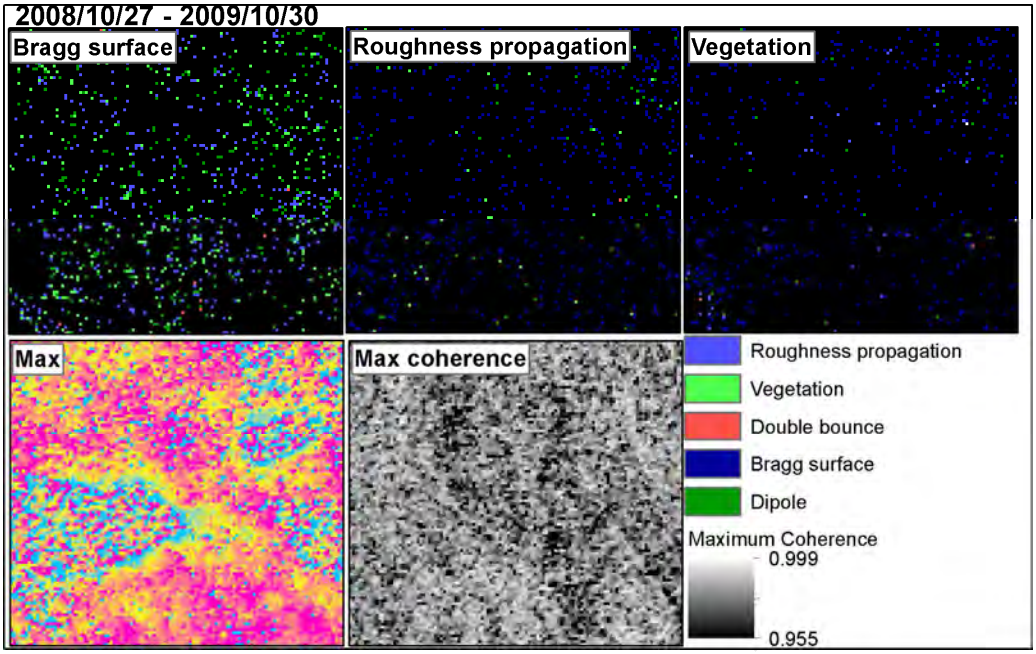

Figure 89: The change in scattering mechanism exhibited on PALSAR data between 2008/10/27 and 2009/10/30.

The scene coherence in this subset is very close to 1 suggesting that, in theory, the coherence optimisation approach was successful in isolating the surface scattering phase contribution. However, the random speckle introduced due to phase noise effects is still present in the differential interferograms. An area of low coherence associated with the subsiding area is not recognised in contrast to what was observed for the RADARSAT-2 data. This suggests that the deformation gradient limit is not reached and the phase noise is introduced from a different source. It is therefore concluded that the fairly heterogeneous nature of the changes in scattering mechanism as observed between image acquisitions introduces random phase changes which destroys the organised fringe pattern even though coherence values are very high.

This investigation demonstrated that the spatial heterogeneity of the scattering process and how it changes over time caused random phase changes associated with temporal baseline effects (including the noise where deformation exceeds the gradient limit) and the evolution of the land surface. These effects could not be removed from interferograms using the polInSAR approaches. The heterogeneity of the scattering processes implied that different phase centres were present in interferograms which introduced a spatially heterogeneous topographic phase contribution. Consequently, the polInSAR

techniques are considered to be unsuccessful in enhancing the ability to extract deformation measurements in the area of interest as hypothesized.

The selection of optimal scattering mechanisms that produces the highest possible coherence is, in this case, probably not the optimal approach since the different scattering mechanisms identified in a heterogeneous area would create a situation where different phase centres are present on a single interferogram for the different scattering mechanisms identified. The different scattering mechanisms and the different phase centres consequently introduce a spatially heterogeneous topographic phase contribution for a single interferometric pair. The ideal would be to select the most stable scattering mechanism which produces the highest possible coherence over time. However, the dynamic vegetated nature of the study area implies that the selection of the same scattering mechanism would not be appropriate.

6.3 THE IMPACT ON DEFORMATION MEASUREMENTS AND IMPLICATIONS FOR LONG-TERM OPERATIONAL MONITORING

The creation of differential interferograms and the measurement of surface deformation were possible despite temporal and geometric decorrelation effects limiting the number of scenes available for processing. These effects were aggravated by the presence of vegetation during the time of master image acquisition. Although the temporal and geometric decorrelation effects were present, the successful generation of differential interferograms enabled the measurement and monitoring of surface subsidence over time, as discussed in Section 5. Specifically, it was observed that the vegetative conditions at the time of image capture had a significant impact on the quality of derived interferograms.

For interferograms created for periods with lower vegetation biomass and less significant evolution of the surface, successful differential interferogram generation was possible even after 120 days with C-band data. However, for scenes captured during the peak of the growing season and prior to harvesting, 24-day temporal baseline or better is required for successful deformation monitoring. This implies that, if using C-band data, fewer scenes will be needed if monitoring is to take place after harvesting before

the peak of the growing season while more frequent image acquisitions will be needed during the peak of the growing season.

Although the L-band data revealed a very low sensitivity to the evolution of the land surface, the vegetative conditions at the time of image capture had a significant effect on the average scene coherence. However, despite the temporal decorrelation effects, successful differential interferogram generation was possible even for temporal baselines of 782 days with L-band data. Consequently, if the number of scenes needed to measure deformation in the Witbank Coalfields is to be kept to a minimum, L-band data will provide the ability to maximise the temporal baseline requirements, thereby minimising the number of scenes required for monitoring.

The limitation to the use of longer temporal baselines is the amount of deformation experienced in the area of active longwall mining. When interferograms were generated for the short temporal baseline pairs, it was observed that the deformation gradient limit was exceeded, most notably for C-band datasets, but also for L-band datasets to a limited extent. The decorrelation experienced in areas where the deformation gradient is exceeded implies that, irrespective of the characteristics of the surface, temporal baselines below 24-days would be needed to successfully determine the maximum amount of deformation if C-band data will be used. If L-band data are to be used, temporal baselines below the 46-day temporal baseline provided by PALSAR data will be needed if the maximum surface deformation needs to be quantified. Therefore, for accurate deformation measurements in the centre of deformation basins, shorter temporal baselines of longer wavelength data are required.

The longer wavelength data will provide an improved ability to measure deformation maxima although this would be at the expense of small scale deformation measurements at the edges of subsidence basins. This is because longer wavelength data is less sensitive to small scale surface deformations than the shorter wavelength datasets (Section 2.2). Consequently, it is possible that the very small scale surface deformation due the re-activation of subsidence over old workings could be missed if long wavelength data is used. If the quantification of the maximum amount of deformation is not important and only the extent of subsiding areas needs to be established, then longer temporal baseline datasets and shorter wavelength datasets would be suitable.

The characteristics of the surface at the wavelength and polarisation of the sensor also influence the sensitivity to geometric decorrelation effects. For C-band data, polarimetric analysis revealed that medium entropy surface scattering (surface roughness propagation effects) effects dominated over low entropy surface scattering mechanisms except for the period after 2011/05/02 up to 2011/09/23. This suggests that agricultural fields at C-band appear smooth during a window between 2011/05/02 and 2011/09/23 where baseline decorrelation effects will be maximised. This implies that C-band image acquisitions after harvesting but before tilling and planting activities would have to be captured at very short perpendicular baselines. However, for the majority of the vegetative cycle the fields at C-band appear rough which is associated with a decreased sensitivity to baseline decorrelation effects. However, it should be noted that VV polarisation data is more sensitive to changes in roughness conditions (Natural Resources Canada 2012) implying that HH polarisation data is recommended if C-band data is to be used. At L-band, the agricultural fields appear smooth irrespective of the time of year and consequently short perpendicular baselines scenes will be needed to minimise baseline decorrelation effects irrespective of the time of year or the polarisation used.

Interferometric coherence has been shown to be dependent on the polarisation of the signal depending on the characteristics of the surface at the wavelength of the sensor. Coherence of volume scattering contributions are known to be independent of polarisation whilst surface scattering contributions are highly dependent on polarisation (Papathanassiou & Cloude 2001). This was confirmed by the observation that X-band data exhibited a very low polarisation dependency (Section 4.3.3), compared to C-band data, where the average scene coherence was dependent on the input polarisation (Section 4.1.3). The polarisation dependency appeared to be even more dramatic for L-band data although too few fully polarimetric scenes were available to definitively prove this (Section 4.2.3).

The reason for the different sensitivities to polarisation is that, at X-band, the dominant scattering mechanism is volume scattering contributions due to the agricultural nature of the study area whilst at C-band, surface scattering mechanisms also contribute to the interferometric phase. For C-band data, the dominance of volume scattering mechanisms during the peak of the growing season and surface scattering mechanisms after the peak of the growing season (after 2011/04/08) (Section 4.4.1) also implies that the sensitivity to the polarisation of the signal will vary depending on the time of year. Where volume scattering effects dominate, the sensitivity to polarisation is expected to be lower than

periods where surface scattering dominate. Finally, at L-band, the dominant scattering contribution is expected to be from the surface which will provide the highest sensitivity to polarisation. Note that, in general, different polarimetric channels correspond to different phase centres in the pixel. Therefore, the use of different polarisations will lead to a topographic phase change that would contaminate the time series of interferograms. Therefore, the selection of polarisation, once made, should be adhered to in order to eliminate the possibility of introducing topographic phase variations when different polarisations are used.

The limitations induced by the effects of phase decorrelation due to geometric and temporal parameters imply that advanced dInSAR approaches may be more suitable for the long term monitoring of surface deformation. However, due to the agricultural nature of the study area, techniques which rely on the detection and processing of coherent targets over time could not be used. These techniques include the persistent scatterers and SBAS techniques. The coherence optimisation approach provided by polInSAR techniques allowing for the selection of multiple scattering mechanisms providing the highest possible coherence was tested for its availability to maximise interferometric coherence. For both C-band and L-band data, the polInSAR approach did result in an increase in interferometric coherence. However, the increase in coherence did not provide an enhanced ability to measure mining-induced subsidence compared to traditional dInSAR approaches as hypothesised. This was due to the selection of multiple optimised scattering mechanisms that incorporated topographic phase in an unpredictable way. Additionally, the decorrelation due to the gradient limit being exceeded for C-band data implies that, even if temporal decorrelation effects could be minimised by polInSAR techniques, the measurement of the maximum amount of deformation would not be possible.

7 CONCLUDING REMARKS AND RECOMMENDATION FOR FUTURE RESEARCH

Mining activities have the tendency to change the natural environment in several ways. Surface deformation due to underground mining is one area of concern since it poses risks not only to health and safety, but also to infrastructure and the environment. The monitoring of surface deformation has traditionally been achieved by means of ground-based approaches. However, these techniques provide only point-based measurements meaning that the full extent of deforming areas is frequently poorly

understood. Additionally, field-based measurements are usually made only on a reasonable assumption of potential deformation or once evidence of deformation has been detected by some other means, such as the observation of infrastructural damage or rainwater ponding on agricultural fields. The field-based approaches are also expensive in terms of man-power, especially if large areas need to be monitored on a regular basis.

To overcome the limitations associated with the field-based techniques, the use of differential radar interferometry techniques was considered in this investigation for its ability to reliably monitor large areas over time, remotely. Specifically, the investigation aimed to test the application of differential radar interferometry techniques for their ability to detect, measure and monitor mining-induced surface deformation in the Witbank Coalfields, South Africa. The dynamic agricultural nature of the area implied that known limitations due to phase decorrelation of SAR signals over time could be expected. For this reason, four sources of SAR data were used, which provides information captured at three different wavelengths namely X-Band (3.1 cm), C-band (5.6 cm), and L-band (23.6 cm). Different geometric and temporal properties at the time of image capture provided an opportunity to investigate the various signal decorrelation effects of data from standard SAR imaging platforms using a real-world deformation phenomenon as a test-case.

The results of the monitoring of surface deformation using the various sources of SAR data were presented together with an analysis of the parameters most detrimental to the successful long-term monitoring of surfaces deformation using these techniques. The results revealed that dInSAR techniques can be employed to detect measure and monitor surface subsidence associated with coal mining activities in the Witbank Coalfields. The results of the investigation further revealed that differential polarimetric interferometry did not provide an enhanced ability to measure mining-induced subsidence compared to traditional single polarisation interferometry approaches as hypothesised. Despite significant improvements in the actual coherence values, the spatial heterogeneity of the phase contributions could not be improved. More specifically, polInSAR techniques were not able to overcome coherence limitations associated with vegetation cover and the evolution of the land surface over time.

Although polarimetric data could not be used to enhance deformation measurements, the polarimetric analysis of quadrature polarisation data did provide an indication of the dominant scattering mechanisms over time and at different wavelengths. Together with the deformation measurements and analysis of the parameters associated with phase decorrelation, this information provided a significant amount of material that could be used to define the optimal sensor configuration and image acquisition strategy for the long-term monitoring of mining induced subsidence. Specifically, the results suggested that the deformation associated with long-wall mining frequently exceeded 2.8 cm per 10 metres over a 24-day period. Additionally, in extreme cases, deformation also exceeded 11.5 cm over 10 metres over a 46-day period. This implies that the longer wavelength datasets would be needed over shorter time intervals to measure the absolute amount of deformation taking place in the Witbank Coalfields.

If the determination of the absolute amount of deformation is not critical but rather the determination of the extent of the deforming areas, the shorter wavelength C-band data would be better suited since it is more sensitive to the smaller scale deformations. However, the sensitivity of the interferometric coherence to vegetation density is a major limitation. For short wavelength data, short temporal baseline datasets are needed during the peak of the growing season. However, longer temporal baseline datasets would be acceptable after the growing season and after harvesting.

The optimal polarisation for monitoring if only single polarisations datasets can be acquired was determined to be HH polarisation data if C-band data is to be used. Although more analysis of fully polarimetric data is needed to draw accurate conclusions, VV polarisation appears to be the optimal polarisation if L-band data is to be used. Furthermore, although the smallest possible perpendicular baseline and Doppler centroid difference image pairs are generally required, the C-band data captured for the largest portion of the year will be less sensitive to baseline decorrelation effects than L-band data. The results further revealed that, due to the vegetative conditions and the dynamic nature of the study area, X-band data is not suitable for the monitoring of surface subsidence in the area.

The sources of decorrelation in this investigation were assumed to be limited to temporal and geometric decorrelation. More specifically, atmospheric ambiguities and sources of atmospheric decorrelation were not considered for this study. Although advanced dInSAR techniques such as PS and SBAS techniques can be used to filter out the atmospheric effects, the current investigation assumed that these

approaches would fail due to a limited number of coherent targets over time. This is a reasonable assumption given the agricultural nature of the area. However, these techniques in combination with the small baseline and Doppler centroid difference datasets should be tested in future research. These techniques if used in combination with coherence optimisation techniques may overcome the limitations described in this investigation. Future research will also focus on determining the phase contribution introduced by the various decorrelation sources in an effort to determine the impact on deformation measurement.

Despite the challenges and limitations described above, the results presented in this investigation demonstrate that the traditional dInSAR approaches can still overcome many of the limitations associated with field-based approaches. Specifically, large areas can be monitored remotely and the areal extent of deforming basins can be assessed. Additionally, the revisit time of the sensors used ranged between 11 and 46 days meaning that routine measurements will be possible. Consequently, dInSAR measurements are highly complimentary to traditional monitoring approaches. The use of dInSAR techniques to monitor surface deformation will provide valuable information for land use planning and subsidence risk assessment. In conclusion, given the results of this investigation, it is recommended that dInSAR techniques are included as a part of a long-term strategy for the monitoring of deformation due to mining.

8 REFERENCES

Akoglu, A. M., Cakir, Z., Meghraoui, M., Belabbes, S., El Alami, S. O., Ergintav, S., & Akyüz, H. S. 2006. The 1994-2004 Al Hoceima (Morocco) earthquake sequence: Conjugate fault ruptures deduced from InSAR. *Earth and Planetary Science Letters*, 252 pp. 467-480.

Anderson, A. 2007. Land subsidence. *Renew Canada*, 33.

Bell, F. G., Bullock, S. E. T., Hälbich, T. F. J., & Lindsay, P. 2001. Environmental impacts associated with an abandoned mine in the Witbank Coalfield, South Africa. *International Journal of Coal Geology*, 45 pp. 195-216.

Berardino, P., Fornaro, G., Lanari, R., & Sansosti, E. 2002. A new algorithm for surface deformation monitoring based on small baseline differential SAR interferograms. *IEEE Transactions on Geoscience and Remote Sensing*, 40 (11) pp. 2375-2383.

Binghuang, Z. & Bing, C. 2007. An analysis of coherence optimisation methods in PolInSAR. *1st Asian and Pacific Conference on Synthetic Aperture Radar*, Huangshan, China.

Blaes, X. & Defourny, P. 2003. Retrieving crop parameters based on tandem ERS 1/2 interferometric coherence images. *Remote Sensing of Environment*, 88 pp. 374-385.

Boerner, W.-M. & Verdi, J. S. 1998. Advances in polarimetric SAR interferometry and its application to geo/eco-environmental stress change monitoring. *12th International Conference on Microwaves and Radar*, Krakow, Poland, pp. 277-303.

Cakir, Z., Akoglu, A. M., Belabbes, S., Ergintac, S., & Meghraoui, M. 2005. Creeping along the Ismetpasa section of the North Anatolian fault (Western Turkey): Rate and extent from InSAR. *Earth and Planetary Science Letters*, 238 pp. 225-234.

Canaslan, F. & Ustun, A. 2012. Impact of perpendicular and temporal baseline characteristics on InSAR coherence maps. *FIG Working Week 2012*, Rome, Italy.

Carnec, C. & Delacourt, C. 2000. Three years of mining subsidence monitored by SAR interferometry, near Gardanne, France. *Journal of Applied Geophysics*, 43 pp. 43-54.

Carnec, C. & Raucoules, D. 2000. Assessment of SAR interferometry within operational applications: mapping and modeling of peri-urban subsidence. *The ESA ERS-ENVISAT Symposium*, Gothenburg, Sweden.

Chang, H. C., Ge, L., & Rizos, C. 2004. Application of repeat-pass DInSAR and GIS for underground mine subsidence monitoring. www.gmat.unsw.edu.au/snap/publications/chang_etal2004d.pdf. 1-11-2007.

Cloude, S. R. & Pottier, E. 1997. An entropy based classification scheme for land applications of polarimetric SAR. *IEEE Transactions on Geoscience and Remote Sensing*, 35 pp. 68-78.

Cloude, S. R. 2010. *Polarisation applications in remote sensing.* Oxford University Press, New York.

Cloude, S. R. & Papathanassiou, K. 1998. Polarimetric SAR interferometry. *IEEE Transactions on Geoscience and Remote Sensing*, 36 (5) pp. 1551-1565.

Cloude, S. R. & Papathanassiou, K. P. 1997. Coherence optimisation in polarimetric SAR interferometry. *IEEE International Geoscience and Remote Sensing Symposium*, Singapore, pp. 1932-1934.

Cloude, S. R. & Pottier, E. 1996. A review of target decomposition theorems in radar polarimetry. *IEEE Transactions on Geoscience and Remote Sensing*, 34 (2) pp. 498-518.

Colin, E., Titin-Schnaider, C., & Tabbara, W. 2006. An interferometric coherence optimization method in radar polarimetry for high-resolution imagery. *IEEE Transactions on Geoscience and Remote Sensing*, 44 (1) pp. 167-175.

Doyle, G. S., Inggs, M. R., & Hartnady, C. J. H. 1997. The use of interferometric SAR in a study of reservoir induced crustal deformation. *Proceedings of the South African Symposium on Communication and Signal Processing*, Grahamstown, South Africa.

Doyle, G. S., Stow, R., & Inggs, M. R. 2011a. Satellite radar interferometry reveals mining induced seismic deformation in South Africa. *IEEE International Geoscience and Remote Sensing Symposium*, Sydney, Australia.

Doyle, G. S., Wilkinson, A. J., & Inggs, M. R. 1999. Contending with high relief and temporal decorrelation in an InSAR study of the effects of reservoir loading. *IEEE International Geoscience and Remote Sensing Symposium*, Hamburg, Germany.

Doyle, G. S., Wilkinson, A. J., & Inggs, M. R. 2001b. Major conclusions relating to the Katse dam differential InSAR study. *IEEE International Geoscience and Remote Sensing Symposium*, Sydney, Australia.

Engelbrecht, J., Inggs, M. R., & Makusha, G. 2011. Detection and monitoring of surface subsidence associated with mining activities in the Witbank Coalfields, South Africa, using differential radar interferometry. *South African Journal of Geology*, 114.1 pp. 77-94.

ESA (European Space Agency) 2005. *Spaceborne radar applications in Geology* TM-17.

Euillades, L. D., Euillades, P. A., Pepe, A., Blanco, M. H., & Barón, J. H. 2011. On the generation of late ERS deformation time series through small Doppler and baseline subsets differential SAR interferograms. *IEEE Geoscience and Remote Sensing Letters*, 8 (2) pp. 238-242.

European Space Agency. 2012. Polarimetry tutorial. http://envisat.esa.int/polsarpro/tutorial.html. 19-12-2012.

Farr, T. G. 1993. Radar interactions with geological surfaces. in *Guide to Magellan image interpretation.*, J. P. Ford et al., eds., National Aeronautics and Space Administration, Jet Propulsion Laboratory, Pasadena, California.

Ferretti, A., Monti-Guarnieri, A., Prati, C., Rocca, F., & Massonnet, D. 2007. *InSAR Principles: Guidelines for SAR interferometry processing and interpretation*, European Space Agency, TM-19.

Ferretti, A., Prati, C., & Rocca, F. 2001. Permanent scatterers in SAR interferometry. *IEEE Transactions on Geoscience and Remote Sensing*, 39 (1) pp. 8-20.

Galloway, D. L. & Hoffman, J. 2007. The application of satellite differential SAR interferometry-derived ground displacements in hydrogeology. *Hydrogeology Journal*, 15 pp. 133-154.

Grey, W. & Luckman, A. 2001. Deriving urban topography from multi-baseline SAR interferometric phase coherence images. http://earth.esa.int/pub/ESA_DOC//gothenburg/309grey.pdf 4-1-2012.

Guéguen, Y., Deffontaines, B., Fruneau, B., Al Heib, M., de Michele, M., Raucoules, D., Guise, Y., & Planchenault, J. 2009. Monitoring residual mining subsidence of Nord/Pas-de-Calais coal basin from differential and Persistent Scatterer Interferometry (Northern France). *Journal of Applied Geophysics*, 69 pp. 24-34.

Herrera, G., Tomás, R., Lopez-Sanchez, J. M., Delgado, J., Mallorqui, J. J., Duque, S., & Mulas, J. 2007. Advanced DInSAR analysis on mining areas: La Union case study (Murcia, SE Spain). *Engineering Geology*, 90 pp. 148-159.

Jiang, M., Ding, X. L., Li, Z. W., & Zhang, L. A functional model for predicting the detectable deformation gradient by D-INSAR. *Proceedings of the Fringe Workshop*, Frascati, Italy.

Kemp, J. N. 2010. *The application of multi-source remote sensing for sediment transport mapping in an intertropical context (La Réunion Island and South Africa).* PhD Thesis, University of La Réunion.

Kervyn, F., Ayub, S., Kajara, R., Kanza, E., & Temu, B. 2006. Evidence of recent faulting in the Rukwa rift (West Tanzania) based on radar interferometric DEMs. *Journal of African Earth Sciences*, 44 pp. 151-168.

Le Mouélic, S., Raucoules, D., Carnec, C., & King, C. 2005. A least squares adjustment of multi-temporal InSAR data: Application to the ground deformation of Paris. *Photogrammetric Engineering and Remote Sensing*, 71 (2) pp. 197-204.

Liu, G. X., Ding, X. L., Li, Z. L., Chen, Y. Q., & Yu, S. B. 2004. Pre- and co-seismic ground deformations of the 1999 Chi-Chi, Taiwan earthquake, measured with SAR interferometry. *Computers & Geosciences*, 30 pp. 333-343.

López-Martinez, C., Fàbregas, X., & Pipia, L. 2009. PolSAR and PolInSAR model based information estimation. *IEEE International Geoscience and Remote Sensing Symposium*, Cape Town, South Africa, p. III-959-III-962.

Manzo, M., Riccardi, G. P., Casu, F., Ventura, G., Zeni, G., Borgström, S., Bererdino, P., Del Gaudio, C., & Lanari, R. 2006. Surface deformation analysis in the Iscia Island (Italy) based on spaceborne radar interferometry. *Journal of Volcanology and Geothermal Research*, 151 pp. 399-416.

Massonnet, D. 1995. Application of remote sensing data in earthquake monitoring. *Advances in Space Research*, 15 pp. 1137-1144.

Massonnet, D., Briole, P., & Arnaud, A. 1995. Deflation of Mount Etna monitored by spaceborne radar interferometry. *Nature*, 375 (6532) pp. 567-570.

Massonnet, D. & Feigl, K. L. 1998. Radar interferometry and its application to changes in the Earth's surface. *Reviews of Geophysics*, 36 pp. 441-500.

Massonnet, D., Rossi, M., Carmona, C., Adranga, F., Peltzer, G., Feigl, K., & Rabaute, T. 1993. The displacement field of the Landers earthquake mapped by radar interferometry. *Nature*, 364 (6433) pp. 138-142.

McCarthy, T. S. & Pretorius, K. 2009. Coal mining on the highveld and its implications for future water quality in the Vaal River system. *The International Mine Water Conference*, Pretoria, South Africa, pp. 56-65.

Mora, O., Mallorqui, J. J., & Broquetas, A. 2003. Linear and nonlinear terrain deformation maps from a reduced set of interferometric SAR images. *IEEE Transactions on Geoscience and Remote Sensing*, 41 (10) pp. 2243-2253.

Natural Resources Canada. 2012. Radar Polarimetry. http://www.nrcan.gc.ca/earth-sciences/geography-boundary/remote-sensing/radar/1893. 1-8-2012.

Navarro-Sanchez, V. D., Lopez-Sanchez, J. M., & Vicente-Guijalba, F. 2010. A contribution of polarimetry to satellite differential SAR interferometry: increasing the number of pixel candidates. *IEEE Geoscience and Remote Sensing Letters*, 7 (2) pp. 276-280.

Neumann, M., Ferro-Famil, L., & Reigber, A. 2007. Multibaseline PolInSAR coherence modelling and optimization. *IEEE International Geoscience and Remote Sensing Symposium*, Barcelona, Spain.

Neumann, M., Ferro-Famil, L., & Reigner, A. 2008. Multibaseline polarimetric SAR interferometry coherence optimization. *IEEE Geoscience and Remote Sensing Letters*, 5 (1) pp. 93-97.

NSIDC. 2009. SAR Theory/Interpreting Images. http://nsidc.org/data/radarsat/pdfs/SARTheory.pdf. 8-5-2012.

Öttl, H., Moreira, A., & Süss, H. 2000. Some results of new microwave remote sensing experiments. *Acta Astronautica*, 47 pp. 355-363.

Papathanassiou, K. & Cloude, S. R. 2005. Single vs multi-polarization interferometry. http://envisat.esa.int/polsarpro/Manuals/2_Single_vs_Multi_Polarization_Interferometry.pdf.

Papathanassiou, K. P. & Cloude, S. R. 1997. Polarimetric effects in repeat-pass SAR interferometry. *IEEE International Geoscience and Remote Sensing Symposium*, Singapore, pp. 1926-1928.

Papathanassiou, K. P. & Cloude, S. R. 2001. Single-baseline polarimetric SAR interferometry. *IEEE Transactions on Geoscience and Remote Sensing*, 39 (11) pp. 2352-2363.

Papathanassiou, K. P., Cloude, S. R., Reigber, A., & Boerner, W. M. 2004a. Multi-baseline polarimetric SAR interferometry for vegetation parameters estimation. *IEEE International Geoscience and Remote Sensing Symposium*, Honolulu, Hawaii, pp. 2762-2764.

Papathanassiou, K. P., Reigber, A., & Cloude, S. R. 2000b. Vegetation and ground parameter estimation using polarimetric interferometry Part I: The role of polarization. *Proceedings of the CEOS SAR Workshop*, Toulouse, France.

Perski, Z. & Jura, D. 2003. Identification and measurement of mining subsidence with SAR interferometry: Potentials and limitations. *Proceedings of the 11th FIG Symposium on Deformation Measurements*, Santorini, Greece.

Pipia, L., Fabregas, X., Aguasca, A., Lopez-Martinez, C., & Mallorquí, J. J. 2009. Polarimetric coherence optimization for interferometric differential applications. *IEEE International Geoscience and Remote Sensing Symposium*, Cape Town, South Africa, p. V-146-V-149.

Prati, C., Ferretti, A., & Perissin, D. 2010. Recent advances on surface deformation measurement by means of repeated space-borne SAR observations. *Journal of Geodynamics*, 49 pp. 161-170.

Raucoules, D., Carnec, C., Cruchet, M., Delacourt, C., Feurer, D., & Le Mouélic, S. 2003a. Identification of landslides in La Reunion Island with JERS-1 and RADARSAT-1 radar interferometry. *Proceedings of the FRINGE Workshop*, Frascati, Italy.

Raucoules, D., Colesanti, C., & Carnec, C. 2007. Use of SAR interferometry for detecting and assessing ground subsidence. *C.R Geoscience*, 339 pp. 289-302.

Raucoules, D., Maisons, C., Carnec, C., Le Mouelic, S., King, C., & Hosford, S. 2003b. Monitoring of slow ground deformation by ERS radar interferometry on the Vauert salt mine (France) Comparison with ground-based measurement. *Remote Sensing of Environment*, 88 pp. 468-478.

Reigber, A., Neumann, M., Erten, E., Jäger, M., & Prats, P. 2007. Multi-baseline polarimetrically optimised phases and scattering mechanisms for InSAR applications. *IEEE International Geoscience and Remote Sensing Symposium*, Barcelona, Spain.

Rosen, P. A., Hensley, S., Joughin, I. R., Li, F. K., Madsen, S. N., Rodríguez, E., & Goldstein, R. M. Synthetic Aperture Radar Interferometry 3 edn, pp. 333-385.

Rosich, B., Esteban, D., Emiliani, G., Meadows, P., & Schättler, B. 2000. Assessment of the new ERS-2 mono-gyro piloting mode on the quality of ERS SAR data and ERS SAR applications performance. *ERS-Envisat Symposium*, Gothenburg, Sweden.

Sagués, L., Lopez-Sanches, J. M., Fortuny, J., Fabregas, X., & Broquetas, A. 2001. Polarimetric radar interferometry for improved mine detection and surface clutter rejection. *IEEE Transactions on Geoscience and Remote Sensing*, 39 pp. 1271-1278.

Samsonov, S. & d'Oreye, N. 2012. Multidimensional time-series analysis of ground deformation from multiple InSAR data sets applied to Virunga Volcanic Province. *Geophysical Journal International*, 191 pp. 1095-1108.

SARscape. 2009. SARscape v. 4.1 Help Files. March 2009 ed, Sarmap.

Silva, W. F., Rudorff, B. F. T., Formaggio, A. R., Paradella, W. R., & Mura, J. C. 2012. Simulated mutlipolarized MAPSAR images to distinguish agricultural crops. *Scientia Agricola*, 69 (3) pp. 201-209.

Simonetto, E., Raucoules, D., & Carnec, C. 2005. Interferometry of spatial radar images for post-mining surveillance: Experiment feedback. *Post-Mining 2005*, Nancy, France.

Smith, L. C. 2002. Emerging applications of interferometric synthetic aperture radar (InSAR) in geomorphology and hydrology. *Annals of the Association of American Geographers*, 92 pp. 385-398.

Stebler , O., Meier, E., & Nüesch, D. 2002. Multi-baseline polarimetric SAR interferometry- first experimental spaceborne and airborne results. *ISPRS Journal of Photogrammetry and Remote Sensing*, 56 pp. 149-166.

Stebler, O., Small, D., Divis, L., Schwerzmann, A., Lüthi, M., Meier, E., & Nüesch, D. 2005. Swiss Alpine Airborne SAR Experiment (SASARE): Multi-Baseline Polarimetric SAR Interferometry studies at L-band and P-band. *Proceedings of the 2nd International Workshop on Applications of SAR Polarimetry and Polarimetric Interferometry (POLinSAR)*, Frascati, Italy.

Tanase, M. A., Santoro, M., Wegmüller, U., de la Riva, J., & Pérez-Cabello, F. 2010. Properties of X-, C- and L-band repeat-pass interferometric SAR coherence in Mediterranean pine forests affected by fires. *Remote Sensing of Environment*, 114 pp. 2182-2194.

Tomás, R., Márquez, Y., Lopez-Sanches, J. M., Delgado, J., Blanco, P., Mallorquí, J. J., Martínez, M., Herrera, G., & Mulas, J. 2005. Mapping ground subsidence induced by aquifer overexploitation using advanced Differential SAR Interferometry: Vega Media of the Segura River (SE Spain) case study. *Remote Sensing of Environment*, 98 pp. 269-283.

Yen, J.-Y., Chen, K.-S., Chang, C.-P., & Boerner, W.-M. 2007. Evaluation of earthquake potential and surface deformation by differential interferometry. *Remote Sensing of Environment*, 112 (3) pp. 782-795.

Zebker, H. A. & Villasenor, J. 1992. Decorrelation in interferometric radar echoes. *IEEE Transactions on Geoscience and Remote Sensing*, 30 (5) pp. 950-959.

Zhou, X., Chang, N.-B., & Li, S. 2009. Applications of SAR interferometry in earth and environmental research. *Sensors*, 9 pp. 1876-1912.